Beta delayed particle emission

Probing the triple alpha continuum

Christian Aa. Diget

Experimental Nuclear Physics Group
Department of Physics and Astronomy
University of Aarhus, Denmark

Dissertation for the degree of Doctor of Philosophy

2nd Edition, September 2006

This dissertation has been submitted to the Faculty of Science at the University of Aarhus in Denmark, to fulfill the requirements for the PhD degree in Physics. The presented work has unless otherwise stated been performed by me under the supervision of Doctor Karsten Riisager and Doctor Hans O. U. Fynbo.
In the second edition, mainly typographical errors have been corrected. For further details see errata.

When I consider your heavens,
the work of your fingers,
the moon and the stars,
which you have set in place,
what is man that you are mindful of him,
the son of man that you care for him?
Psalms 8,3–4

Contents

List of Publications

Publications

H.H. Knudsen, H.O.U. Fynbo, M.J.G. Borge, R. Boutami, P. Dendooven, **C.Aa. Diget**, T. Eronen, S. Fox, L.M. Fraile, B. Fulton, J. Huikary, H.B. Jeppesen, A.S. Jokinen, B. Jonson, A. Kankainen, I. Moore, A. Nieminen, G. Nyman, H. Penttilä, K. Riisager, S. Rinta-Antila, O. Tengblad, Y. Wang, K. Wilhelmsen, and J. Äystö, *Beta-decay of 13O*, Physical Review C 72 (2005) 044312.

C.Aa. Diget, F.C. Barker, M.J.G. Borge, J. Cederkäll, V.N. Fedosseev, L.M. Fraile, B.R. Fulton, H.O.U. Fynbo, H.B. Jeppesen, B. Jonson, U. Köster, M. Meister, T. Nilsson, G. Nyman, Y. Prezado, K. Riisager, S. Rinta-Antila, O. Tengblad, M. Turrion, K. Wilhelmsen and J. Äystö, *Properties of the 12C 10 MeV state determined through beta-decay*, Nuclear Physics A 760 (2005) 3-18.

Y. Prezado, M.J.G. Borge, **C.Aa. Diget**, L.M. Fraile, B.R. Fulton, H.O.U. Fynbo, H.B. Jeppesen, B. Jonson, M. Meister, T. Nilsson, G. Nyman, K. Riisager, O. Tengblad and K. Wilhelmsen, *Low-lying resonance states in the 9Be continuum*, Physics Letters B 618 (2005) 43–50.

Hans O.U. Fynbo, **Christian Aa. Diget**, Uffe C. Bergmann, Maria J.G. Borge, Joakim Cederkäll, Peter Dendooven, Luis M. Fraile, Serge Franchoo, Valentin N. Fedosseev, Brian R. Fulton, Wenxue Huang, Jussi Huikari, Henrik B. Jeppesen, Ari S. Jokinen, Peter Jones, Björn Jonson, Ulli Köster, Karlheinz Langanke, Mikael Meister, Thomas Nilsson, Göran Nyman, Yolanda Prezado, Karsten Riisager, Sami Rinta-Antila, Olof Tengblad, Manuela Turrion, Youbao Wang, Leonid Weissman, Katarina Wilhelmsen, Juha Äystö and The ISOLDE Collaboration, *Revised rates for the stellar triple-alpha process from measurement of 12C nuclear resonances*, Nature 433 (2005) 136–139.

Y. Prezado, U.C. Bergmann, M.J.G. Borge, J. Cederkäll, **C.Aa. Diget**, L.M. Fraile, H.O.U. Fynbo, H. Jeppesen, B. Jonson, M. Meister, T. Nilsson, G. Nyman, K. Riisager, O. Tengblad, L. Weissmann, K. Wilhelmsen Rolander and the ISOLDE Collaboration, *Large asymmetry in the strongest beta-transition for A=9*, Physics Letters B 576 (2003) 55–61

U. C. Bergmann, **C.Aa. Diget**, K. Riisager, L. Weissman, G. Auböck, J. Cederkäll, L. M. Fraile, H.O.U. Fynbo, H. Gausemel, H. Jeppesen, U. Köster, K.-L. Kratz, P. Möller, T. Nilsson, B. Pfeiffer, H. Simon, K. Van de Vel, J. Äystö and the ISOLDE Collaboration, *Beta-decay properties of the neutron-rich 94–99Kr and 142–147Xe isotopes*, Nuclear Physics A 714 (2003) 21–43.

Proceedings

Christian Aa. Diget, Maria J.G. Borge, Rafik Boutami, Peter Dendooven, Tommi Eronen, Simon P. Fox, Brian R. Fulton, Hans O.U. Fynbo, Henrik B. Jeppesen, Ari Jokinen, Björn Jonson, Anu Kankainen, Iain Moore, Arto Nieminen, Solveig G. Pedersen, Heikki Penttilä, Victor F.E. Pucknell, Karsten Riisager, Sami Rinta-Antila, Olof Tengblad, Youbao Wang, Katarina Wilhelmsen and Juha Äystö, *Influences on the triple alpha process beyond the Hoyle state* Proceedings of the International Symposium on Nuclear Astrophysics—Nuclei in the Cosmos—IX, Proceedings of Science PoS(NIC-IX)25 (2006).

S.G. Pedersen, **C.Aa. Diget**, H.O.U. Fynbo, J. Bücherer, P. Van Duppen, M. Huyse, R. Raabe, S. Brandeburg, P. Dendooven, K. Jungmann, G. Onderwater, A. Rogachevskiy, M. Sohani, E. Traykov, H. Wilschut, M. Alcorta, M.J.G. Borge, M.M. Flores, O. Tengblad J. Äystö, A. Jokinen, K. Perajärvi, A. Saastamoinen, B. Jonson, G. Nyman, K. Riisager and B. Fulton, *β-decay studies of states in ^{12}C* Proceedings of the International Symposium on Nuclear Astrophysics—Nuclei in the Cosmos—IX, Proceedings of Science PoS(NIC-IX)244 (2006).

M.J.G. Borge, Y. Prezado, U.C. Bergmann, R. Boutami, J. Cederkäll, **C.Aa. Diget**, L.M. Fraile, H.O.U. Fynbo, Y. Jading, H. Jeppesen, B. Jonson, I. Martel, M. Meister, T. Nilsson, G. Nyman, K. Riisager, H. Simon, O. Tengblad, L. Weissman, F. Wenander and K. Wilhelmsen, *Asymmetry in the super-allowed beta-transitions of the A=9 isobars* Nuclear Physics A 738 (2004) 206–210.

H.O.U. Fynbo, **C.Aa. Diget**, Y. Prezado, J. Äystö, U.C. Bergmann, J. Cederkäll, P. Dendooven, L.M. Fraile, S. Franchoo, B.R. Fulton, W. Huang, J. Huikari, H. Jeppesen, A. Jokinen, B. Jonson, P. Jones, U. Köster, M. Meister, T. Nilsson, G. Nyman, M.J.G. Borge, K. Riisager, S. Rinta-Antila, I. Storgaard Vogelius, O. Tengblad, M. Turrion, Y. Wang, L. Weissman and

K. Wilhelmsen and the ISOLDE Collaboration, *News on 12C from beta-decay studies*, Proceedings of the 8^{th} International Conference on Clustering Aspects of Nuclear Structure and Dynamics, Nara, Japan, November 2003, Nuclear Physics A 738 (2004) 59–65.

H.O.U. Fynbo, U.C. Bergmann, M.J.G. Borge, P. Dendooven, **C.Aa. Diget**, W. Huang, J. Huikari, H. Jeppesen, B. Jonson, P. Jones, M. Meister, G. Nyman, Y. Prezado, K. Riisager, I. Storgaard Vogelius, O. Tengblad, Y. Wang, L. Weissman, K. Wilhelmsen Rolander and J. Äystö, *New information on 12C from the beta-decays of 12N and 12B*, Proceedings of the 7^{th} Nuclei in the Cosmos conference, Fujiyama, Japan, July 2002, Nuclear Physics A 718 (2003) 541–543.

U.C. Bergmann, G. Auböck, R. Catherall, J. Cederkäll, **C.Aa. Diget**, L. Fraile, S. Franchoo, H. Fynbo, H. Gausemel, U. Georg, T. Giles, H. Jeppesen, O.C. Jonsson, U. Köster, J. Lettry, T. Nilsson, K. Peräjärvi, H. Ravn, K. Riisager, L. Weissman, J. Äystö and The ISOLDE Collaboration, *Production yields of noble-gas isotopes from ISOLDE UCx/graphite targets*, The 14^{th} International Conference on Electromagnetic Isotope Separators and Techniques Related to their Applications, Victoria, BC, Canada, May 2002, Nuclear Instruments and Methods B 204 (2003) 220–224.

Public relations

Interviews in January 2005 in relation to *Revised rates for the stellar triple-alpha process from measurement of 12C nuclear resonances*, Nature 433 (2005) 136–139: National radio (DK-P3), local TV-channel (DK4), national newspaper (Jyllandsposten), local newspaper (Morsø Folkeblad).

Acknowledgments

This dissertation is based on the studies I have carried out during my PhD program at the Department of Physics and Astronomy, University of Aarhus, Denmark from August 2002 to July 2006. My studies have been financed partly by the Instrument Center for CERN Experiments (http://www.ice.nbi.dk/) and partly by the Faculty of Science, University of Aarhus. They have furthermore been supported by the European Union Fifth Framework Programme "Improving Human Potential, Access to Research Infrastructure".

The work presented here would not have been possible, had it not been for our collaboration with other groups. I would therefore like to thank firstly the collaboration from the ISOLDE experiment (Diget et al., 2005), that yielded the data on which I worked during the first years of my PhD program:

> M.J.G. Borge, J. Cederkäll, V.N. Fedosseev, L.M. Fraile, B.R. Fulton, H.O.U. Fynbo, H.B. Jeppesen, B. Jonson, U. Köster, M. Meister, T. Nilsson, G. Nyman, Y. Prezado, K. Riisager, S. Rinta-Antila, O. Tengblad, M. Turrion, K. Wilhelmsen and J. Äystö,

And secondly the collaboration from the IGISOL experiment on which the majority of the work presented in this dissertation builds:

> M.J.G. Borge, R. Boutami, P. Dendooven, T. Eronen, S.P. Fox, B.R. Fulton, H.O.U. Fynbo, H.B. Jeppesen, A. Jokinen, B. Jonson, A. Kankainen, I. Moore, A. Nieminen, S.G. Pedersen, H. Penttilä, V.F.E. Pucknell, K. Riisager, S. Rinta-Antila, O. Tengblad, Y. Wang, K. Wilhelmsen and J. Äystö

Among my collaborators I would like to give special thanks to Maria Borge, Olof Tengblad, Björn Jonson and Brian Fulton for your many encouragements and comments on my work. And to my fellow PhD students Henrik Jeppesen, Hans Henrik Knudsen, Solveig Pedersen, Hanna Franberg, Miguel Madurga and Martin Alcorta, thank you for always adding joy to our experiments, meetings and conferences. Even—and perhaps especially—to the night shifts. Regarding the actual work presented in this dissertation, I must thank Solveig, especially for your work on the branching ratios as presented in sections 8.3 and 8.4.

During my studies, I spent half a year in Leuven (Belgium). Many people deserve thanks for making this period a good time. Both in terms of my personal relationships as well as in my professional experiences. Most of all I must thank Mark Huyse, Piet Van Duppen and Riccardo Raabe. Mark for inviting me there and Piet and Riccardo for being there.

In my work I have had important feedback and input from a number of people. In particular from Fred C. Barker on the R-Matrix description in sections 3.3 and 3.4, and from Sam Austin, Karlheinz Langanke and Jørgen Christensen-Dalsgaard on applications of the stellar triple alpha reaction rate.

For the last five years I have had the privilege of being under the supervision of two of the best supervisors I could have wished for. Hans Fynbo was in 2001, as a fellow at CERN, an important mentor for me during my months as a summer student, and during all of my PhD he has in many aspects been supervising me. Not least during the last year. Your never ending encouragements and ideas have been an inspiration throughout my studies. But even more I thank you for the personal relationship, we have developed over the years, where nothing is too big or too deep to be discussed.

Karsten Riisager has been my supervisor during at least five years, starting from my Bachelor's project in 2001 continuing into my PhD program. Your wide knowledge and brilliant mind has challenged me constantly. Your ability to comprehend abundant as well as scarce amounts of data and always draw out the essence is more than anything what dragged me into your group. On the personal side, your open mind and inviting attitude is what made me sure that your group would give me four good and inspiring years as PhD student. In none of these matters have you let me down.

I have many thanks to give my entire family. For your patience, your interest and your encouragements. And to my father, special thanks for your proof reading, and especially for always passing on your passion for physics, no matter if the discussion is with a five year old on the rainbow or with a PhD student on his results in nuclear physics. To my wife, Anna, I cannot rightfully express my gratitude. I do not se how I could have done this without you by my side.

Errata

In the present edition, mainly typographical errors have been corrected, though as well some formulations have been clarified. Only the following corrections however impact the physics results presented in the thesis, and therefore deserves specific mention to those having read the first edition.

Table 6.3.3: The two columns to the right show results for E_3 and γ_3, not E_2 and γ_2.

Section 8.6: The absolute B_{GT} values for the decays of ^{12}N and ^{12}B respectively to the 12.7 MeV state are 0.456(57) and 0.63(13), not 1.17(14) and 1.61(33).

CHAPTER 1

Introduction

Selvfølgeligt er kun ét gode:
at fødes på en beboet klode.[1]

Piet Hein

1.1 Carbon primer

In all living organisms that we know of, including ourselves, molecules such as water, carbon dioxide, oxygen and various organic molecules—as for example fat, sugar and proteins—are essential building blocks and participants in the processes by which organisms breathe, move, grow etc. This is why the current search for life (or the traces of life) on Mars has such a strong focus on water and organic molecules. Though very different all these molecules have one thing in common: They all consist of hydrogen, carbon and oxygen and smaller amounts of other elements. This can for example be seen in figure 1.1.1 where a small fraction of our DNA is illustrated. Here it is evident, that carbon is one of the most important elements in us. It is fair to say that carbon is "the spine of our DNA". Apart from this, carbon is the element that hardens steel and the sole element in diamonds. The burning of carbon in the form of coal and oils is what made the wheels turn in the development of industrial societies. In all this, the carbon was originally created in massive stars extinguished billions of years ago. In the following chapters I will investigate the structure of the nucleus in

[1] Certain is only one good: To be born on an inhabited planet.

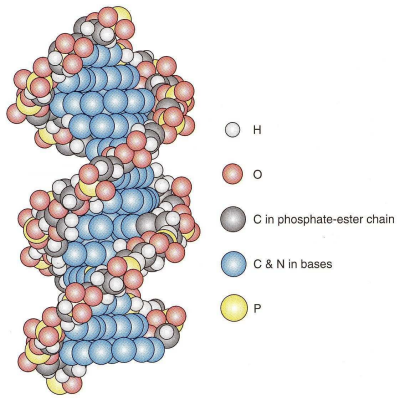

Figure 1.1.1: Atomic constituents of our DNA (Weaver, 2002, pg. 25).

the carbon atom, and describe the effects of this structure on the way carbon is created in stars.

In nature three different isotopes of carbon exist: Carbon 12, carbon 13 and carbon 14. The three behave in the same way chemically, but the nuclei are different, and the numbers denote the total number of nucleons (protons and neutrons) in the nucleus. Of these three isotopes carbon 14 (^{14}C) is probably the most well known. This stems from the fact that it is radioactive, that is, it decays. With a half life of 5730 years (Pfennig et al., 1998) it decays to nitrogen 14, which means if we imagine having for example a small piece of wood containing a certain amount of ^{14}C, after 5730 years half of this will have decayed. Because of this property one can determine the age of materials by determining the amount of ^{14}C still present in the material. This is the so-called carbon 14 dating. Most of the carbon present in nature however is of the other two kinds. They are both stable and of those two ^{12}C is by far the most abundant. This carbon isotope is what I will focus on in the following.

From the 12 nucleons (6 protons and 6 neutrons) the ^{12}C nucleus can be pieced together, like a puzzle. Here however, the puzzle is a bit complicated. Not only is it three dimensional, the individual nucleons move around inside the nucleus, and even overlap. Furthermore the nucleons can be assembled in more than one way as if the puzzle could be pieced together to form more than one picture. In the nucleus, these different "pictures" are called states and can have very different properties. One very important property of those states is their energy, and the state having the lowest energy of all is called the ground state. The ground state is the state present in nature, in other nuclei as well as in the case of ^{12}C. In this dissertation however I will focus on the properties of some of the excited states (states with higher energy than the ground state) in ^{12}C, the states that determine how ^{12}C is produced in massive stars.

1.2 Historical preamble

Before we turn to the hard-core physics, we will for a moment look back at two times when advances in physics important for this work have been made. Firstly the identification of a very important state in ^{12}C by Fred Hoyle and collaborators in the fifties, and secondly the discovery by Thomas Young that light can interfere.

The anthropic principle

In 1953 Fred Hoyle used observations of the cosmic abundances of the elements; helium, carbon and oxygen to argue that the most abundant carbon isotope ^{12}C should have a state at an energy of 7.68 MeV. The level was indeed found at that exact position (Dunbar et al., 1953) and it is now known to have an energy of 7.65 MeV and is denoted *the Hoyle state*. What can be concluded—taking the argument a bit further than Hoyle did—is that: Had there not been a state at this energy, the cosmic abundances of elements would have been much different, so different that life as we know it could probably not have existed. This is the essence of the anthropic principle, that our physical description of the universe and its constituents may not be in conflict with observations, including the observation that we exist. The physics behind Hoyles argument will be introduced in the following.

When elements are produced in stars the protons (p) combine to give helium, in particular ^{4}He. This can proceed via the PP-chains. The simplest example is the PP-I chain (Kippenhahn & Weigert, 1990):

$$\begin{aligned} p + p &\rightarrow {}^2\mathrm{D} + e^+ + \nu_e \\ {}^2\mathrm{D} + p &\rightarrow {}^3\mathrm{He} + \gamma \\ {}^3\mathrm{He} + {}^3\mathrm{He} &\rightarrow {}^4\mathrm{He} + 2p \end{aligned}$$

At this stage the shown sequential buildup of larger and larger nuclei runs into a problem, since neither of the nuclei ^{5}He, ^{5}Li and ^{8}Be are bound. This means that immediately after being formed from a ^{4}He nucleus and a n, p or ^{4}He respectively they break up again.

However, stellar environments do overcome this problem. Since ^{8}Be exists roughly $7 \cdot 10^{-17}$ s (0.00000000000000007 second) according to Audi et al. (2003), a ^{4}He nucleus (alpha particle) "just" has to combine with it within this period. The resulting process is called *the triple-alpha process*:

$$\begin{aligned} {}^4\mathrm{He} + {}^4\mathrm{He} &\rightarrow {}^8\mathrm{Be} \\ {}^8\mathrm{Be} + {}^4\mathrm{He} &\rightarrow {}^{12}\mathrm{C}(7.65\,\mathrm{MeV}) \\ {}^{12}\mathrm{C}(7.65\,\mathrm{MeV}) &\rightarrow {}^{12}\mathrm{C} + \gamma \end{aligned}$$

where the two first steps obtains a statistical equilibrium, as will be discussed thoroughly in chapter 9. After this step heavier elements such as oxygen can be produced.

What Fred Hoyle argued was the following (Hoyle et al., 1953):

> *It is assumed that oxygen and carbon are produced in stars, that have largely exhausted their central hydrogen, by the reactions* $2He^4 \rightarrow Be^8$*;* $Be^8 + He^4 \rightarrow C^{12}$*;* $C^{12} + He^4 \rightarrow O^{16}$*. The observed cosmic abundance ratio of He:C:O can be made to fit the yields calculated for these reactions if the reaction:* $Be^8(\alpha,\gamma)C^{12}$ *has a resonance near* 0.31 *MeV, corresponding to a level at* 7.68 *MeV in* C^{12}*.*

The state should therefore have an energy just above the energy required for a breakup into three ^{4}He nuclei, *the triple-alpha threshold*. Hoyle even argued that if the process is assumed to proceed without involving such a resonance, as was done earlier by Salpeter (1952) and Öpik (1951), the ratio could not be reproduced.[2] Since this state has an energy higher than the triple-alpha threshold, we say that it is situated in the triple-alpha continuum.

Interference of light

About two hundred years ago Thomas Young discovered that rays of light can interfere, they behave like waves, producing either constructive or destructive interference. For waves on a string this is seen as the nodes and anti-nodes respectively where the interference between the waves traveling back and forth in the string is destructive and constructive. In a lecture to the Royal Society of London (Young, 1804) he therefore states the following:

> *The proposition on which I mean to insist at present, is simply this, that fringes of colors are produced by the interference of two portions of light; and I think it will not be denied by the most prejudiced, that the assertion is proved by the experiments I am about to relate, which may be repeated with great ease, whenever the sun shines, and without any other apparatus than is at hand to every one.*

In Youngs experiment a beam of light was split in two by a card, after which it hit a wall behind the card. Now the two components of light hitting the wall does not just add up, but interfere just as was the case for the waves on the string. Here the interference was seen to be constructive or destructive depending on the position on the wall and the distance between the card and the wall. This caused the fringes seen by Young.

Interference however is an even more general property of physical processes, and many other processes show similar effects. These are the processes, where two different paths contribute significantly, and where it is impossible to distinguish between the two paths. An interesting example of this is an experiment very similar to that of Young, but with the difference that carbon is used instead

[2] The historical background behind the current understanding the nucleo-synthesis in stars is nicely described by William A. Fowler in his Nobel lecture of 1983, published in (Fowler, 1993).

of light (Arndt et al., 1999). And not just carbon but large molecules with 60 carbon atoms in each (the so-called C_{60} buckyballs). In this experiment as well the interference pattern is clearly seen.

In the experiment presented in the following chapters, the situation is much the same, though here the contributing paths are not physical positions in space but different ^{12}C states. These ^{12}C states mediate the process that we measure, and if the different "paths" cannot be distinguished physically, the interference arises. In contrast to the experiments of Young and of Arndt et al., the distributions are in this case not spatial distributions seen on a screen, but measured energy distributions in ^{12}C—the ^{12}C excitation energy distributions. The concept however remains the same: the two "paths" interfere either constructively or destructively, distorting the distributions that one would expect to see if no interference was present.

1.3 Excited states of ^{12}C

In the preceding, one excited state of the ^{12}C nucleus has already been presented, namely the Hoyle state. This however is not the only excited state in ^{12}C. As will be seen in the following chapter, at least 9 states in addition to the ground state have been confirmed experimentally within the first 15 MeV above the ground state. What we do as experimental nuclear physicists is to provide information on the individual state properties. This information will in turn allow a better theoretical understanding of the physical processes and interactions determining the state properties and the degrees of freedom that effectively exist in the system.

Different theoretical models are used to describe the properties of such states, models that have different strengths and weaknesses and thereby complement each other. One such model is *the shell model*. In this model the nucleons are described as trapped in a common potential, just like we are trapped by the gravitational potential of the earth. The individual nucleons in this potential can position themselves in different single particle states where the properties of the states differ. Furthermore, according to the *Pauli exclusion principle*[3], two protons (or two neutrons) cannot occupy the same single particle state, and we must therefore fill the states one by one with the available protons and neutrons. These states turn out to be grouped making a shell like structure where many states have similar energy and a gap in energy occur with no states before the next shell of states comes at higher energies. Because of that the model is denoted the shell model. With all nucleons thus placed in their respective single particle states, the global properties of the nucleus can be found by combining the single particle state properties. Another model, fundamentally different from the shell model is *the cluster model*. Here the nucleons are assumed to be grouped into clusters, and the nucleus is described in terms of these clusters, their interaction with each other and their positions relative to each other. This model of course only gives a good description of the nuclear states if they resemble such a cluster

[3]For which Wolfgang Pauli received the Nobel prize in 1945 (Pauli, 1964).

structure, which is *not* the case for all nuclear states. For ^{12}C however many states in the triple alpha continuum can be described in this manner. For the Hoyle state for example, the cluster state description dates back to 1956 at which time Morinaga for the first time described the Hoyle state as an elongated triple alpha cluster state. That is, three alpha particles (clusters of four nucleons) in a row. This idea has been elaborated on since then, and similar descriptions of other states have been attempted. Most of the states that will be examined in the following chapters are in fact best described in the cluster models.

With the shell model and the cluster model complementing each other very well, many nuclear states can be understood. There is however a third group of models worth mentioning. In a sense these are cluster models with an extreme amount of clusters, since they take the individual nucleons and describe their positions relative to each other and the interactions between them. These models are the *ab initio models* where the only input to the model are the interactions between the individual nucleons. One such model is the *quantum Monte-Carlo model* as used by e.g. Pieper (2002) to describe light nuclei. This model is valid more generally than the other two, and in principle covers both. It has however the disadvantage of introducing many additional degrees of freedom, of which many may be irrelevant for the understanding of the particular nuclear state one attempts to describe. Furthermore the extra degrees of freedom causes the amount of computing time to increase drastically with the number of nucleons, which is why the model is only feasible for the nuclei with few nucleons—the low mass nuclei. For these nuclei the model can be used as a test of other models to gain a further understanding of the models that can reach the nuclei with 12 or more nucleons.

CHAPTER 2

Probing the ^{12}C continuum

An experiment aimed at studying the triple alpha continuum states in ^{12}C must necessarily consist of two parts. Firstly a method for populating the states in question and secondly a setup measuring properties of the states in question by detection of particles emitted in the decay of the states. For both parts, different methods have been applied depending on which states and which properties of those states one wishes to describe. In the following we will look at two methods of production and furthermore focus on the detection of alpha particles from the breakup of the studied states.

2.1 Different probes

In recent years two studies of the triple alpha continuum has been performed using inelastic alpha scattering on the ^{12}C ground state $^{12}\mathrm{C}(\alpha,\alpha')^{12}\mathrm{C}^*$ as a probe of the excited states in ^{12}C (Bency John et al., 2003; Itoh et al., 2004). In these experiments the outgoing alpha particle (α') is detected and from the angular distribution of this as a function of energy the spin of the probed states are deduced. With knowledge of the spin, the parity of the state is known as well since only natural parity states are produced (both ^{12}C and ^{4}He are 0^+ nuclei).

As can be seen in figure 2.1.1, many states in ^{12}C are easily produced in this way, with a production method involving only a ^{4}He beam impinging on a thin ^{12}C target. This reaction can populate states in ^{12}C of natural parity, that is states for which the spin (j) and parity (π) satisfy $\pi = (-1)^j$. These and other states in ^{12}C are listed in figure 2.1.2. Furthermore if other reactions are used,

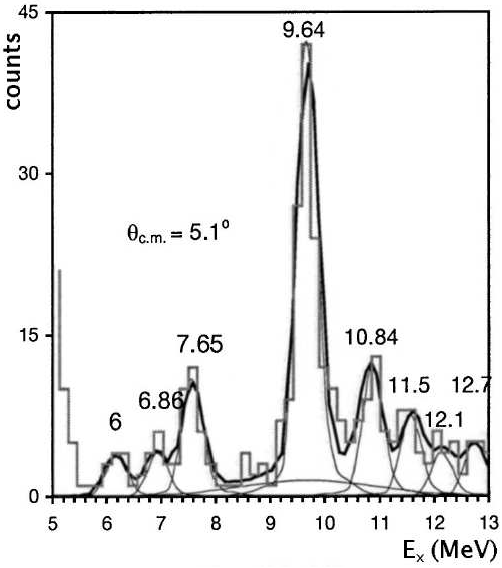

Figure 2.1.1: Inelastic scattering ^{12}C$(\alpha, \alpha')^{12}$C* at a center of mass angle of 5.1 °, measured by Bency John et al. (2003).

the remaining states can be populated. This gives a glimpse of the strength of using reaction studies in nuclear physics, since the reaction is not very selective in populating the states, and a few reactions can therefore probe all states in a single nucleus.

This very small selectivity however can as well be seen as a drawback in certain cases, namely those where we are interested in only a few of the produced states. In the study of Bency John et al. for example, the interest is not only in the rather well known 7.65 MeV 0^+ Hoyle state; the 9.64 MeV 3^- state; and the 10.84 MeV 1^- state that dominate the spectrum. The interest is as well in the broad 0^+ component (indicated as a wide state contributing in the 10 MeV region) and a 2^+ component they suggest around 11.5 MeV. With the very dominant states in the reaction, the results on the 0^+ and 2^+ components are less conclusive. We would therefore prefer a more selective probe of the states.

This is where beta decays prove valuable. For the purposes of the studies presented in the following chapters there are two types of beta decays: beta minus (β^-) and beta plus (β^+)[1]. In a β^- decay a neutron is converted to a

[1]The third possibility is the electron capture, and alternative to the β^+ decay. Here an electron is transformed to a neutrino instead of the usual double lepton emission. This decay mode however is only important when the Q value is very small which, as we will see in the following is not the case for the two beta decays to ^{12}C.

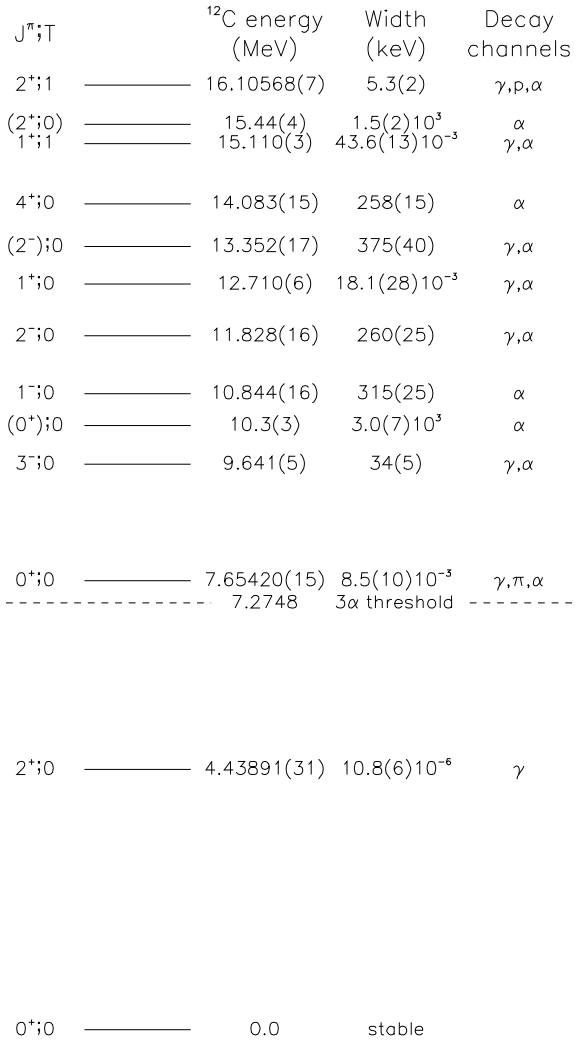

Figure 2.1.2: States in ^{12}C up to about 16 MeV according to the evaluation by Ajzenberg-Selove (1990). Apart from the typical decay channels of α and γ decays, emission of a e^+e^- pair (π) is observed for the 7.6542 MeV Hoyle state.

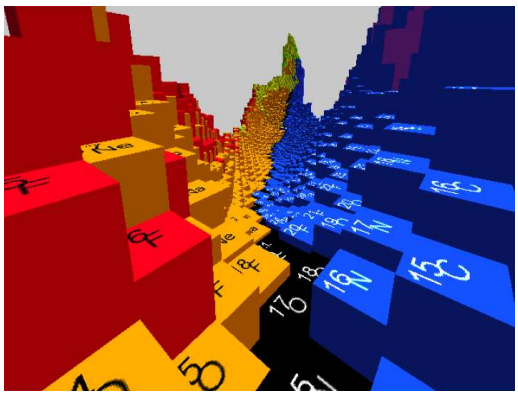

Figure 2.1.3: The valley of stability (figure from: Lunney, 2006). The isotopes in black are stable, whereas the remaining decay. Beta decay transform the nuclei on either side of the valley so they "fall" towards the floor of the valley.

proton under the emission of a pair of leptons:

$$ {}^{A}_{Z}\mathrm{X} \rightarrow {}^{A}_{Z+1}\mathrm{Y} + e^- + \bar{\nu}_e + Q_{\beta^-} \tag{2.1.1} $$

where A is the total number of nucleons in the mother nucleus X and Z is the number of protons. In a β^+ decay it is the opposite:

$$ {}^{A}_{Z}\mathrm{X} \rightarrow {}^{A}_{Z-1}\mathrm{Y} + e^+ + \nu_e + Q_{\beta^+} \tag{2.1.2} $$

To determine which of the two decays (if any) will take place we have to look at the energy—or mass, according to $E = mc^2$ (Einstein, 1905)—available in the decaying nucleus and the energy required by the daughter nucleus Y and the emitted leptons. The Q value for the decays is the difference between the two and must be positive for the decay to occur. The energy surplus in the decay (the Q value) is given as kinetic energy to the three particles created in the decay. The Q value for the two decays can be found from the atomic masses of the two nuclei:

$$ Q_{\beta^-} = M_{\mathrm{X}}c^2 - M_{\mathrm{Y}}c^2 \tag{2.1.3} $$

$$ Q_{\beta^+} = M_{\mathrm{X}}c^2 - M_{\mathrm{Y}}c^2 - 2m_e \tag{2.1.4} $$

where c is the speed of light and m_e is the mass of the electron. All beta decaying nuclei will therefore decay towards nuclei of lower mass. This results in the so-called valley of stability where the stable nuclei are those with the lowest mass for a given nucleon number A. This is illustrated in figure 2.1.3. The isotopes on the right decay through β^- decay whereas the isotopes on the left decay through β^+ decay until stability is reached. ^{12}C with 6 protons and neutrons (not in the picture) lies at the bottom of this valley with both neighboring nuclei ^{12}N and

^{12}B sufficiently high in energy (sufficiently heavy) to allow both beta decays to ^{12}C. The two beta decays furthermore have so high Q values that the decays can populate higher lying states in ^{12}C. For ^{12}N Q_{β^+} is thus 16.316 MeV whereas for the ^{12}B decay Q_{β^-} is 13.370 MeV.

In general beta decays can be classified as being either allowed ($l = 0$); forbidden ($l = 1$); doubly forbidden ($l = 2$); etc. depending on the angular momentum the two leptons carry away from the nucleus. The classification stems from the observation that forbidden decays are strongly suppressed with respect to the allowed decays, which means the allowed decay mode will dominate if it is possible. There exist two different types of allowed decays, the Fermi decay and the Gamow-Teller decay. The two decays differ in respect to the lepton spins. For Fermi decays the spins of the two leptons ($\vec{\frac{1}{2}} + \vec{\frac{1}{2}}$) couple to $\vec{0}$ whereas for the Gamow-Teller decay the two couple to $\vec{1}$. The selection rules for the two decays are therefore different.

The Fermi decay simply changes a neutron(proton) to a proton(neutron) leaving the latter in exactly the same single particle state as the original nucleon occupied. This means the spin, parity and isospin of the daughter nucleus are identical to those of the mother nucleus. The decay is restricted to the so-called isobaric analogue state in the daughter nucleus, the state that have exactly the same quantum mechanical wave function as the mother nucleus, in this case the ^{12}C 1^+ state at 15.11 MeV. For the Gamow-Teller decay on the other hand, the spin and isospin of the nucleus are not necessarily conserved, and the only selection rule in the spin of the nucleus is that: $|j_X - 1| \leq j_Y \leq |j_X + 1|$. The parity however is still conserved, as long as the decay is an allowed decay. Since the two nuclei ^{12}N and ^{12}B both have $j^\pi = 1^+$ this means the only states populated in the decays are 0^+, 1^+ and 2^+ states in ^{12}C. As illustrated in figure 2.1.4 this introduces a strong selection among the ^{12}C states.

2.2 Single particle detection

After the discovery of the Hoyle state, the low energy region of the triple-alpha continuum was investigated by Cook et al. (1957, 1958). He and his collaborators used the method of beta delayed particle emission to study the states in the triple alpha continuum, in particular the Hoyle state. The term *beta delayed particle emission* comes from the observation that beta decay is a weak process and is therefore in general very slow compared to other decay processes. When beta decay in this way populates continuum states, the particle emission (in this case triple alpha breakup) is delayed by the beta decay. In the case of decays to the Hoyle state, the beta decays have a typical time scale of some milliseconds (thousands of a second) whereas the typical life time of the Hoyle state itself is of the order of 10^{-16} s, hence the name *beta delayed triple alpha breakup*. With this method they used decay of ^{12}B to gain the strong selectivity and through this study found that the Hoyle state was a 0^+ state. In addition to that they saw an indication of a level at 10.1(2) MeV. This was confirmed by Schwalm & Povh

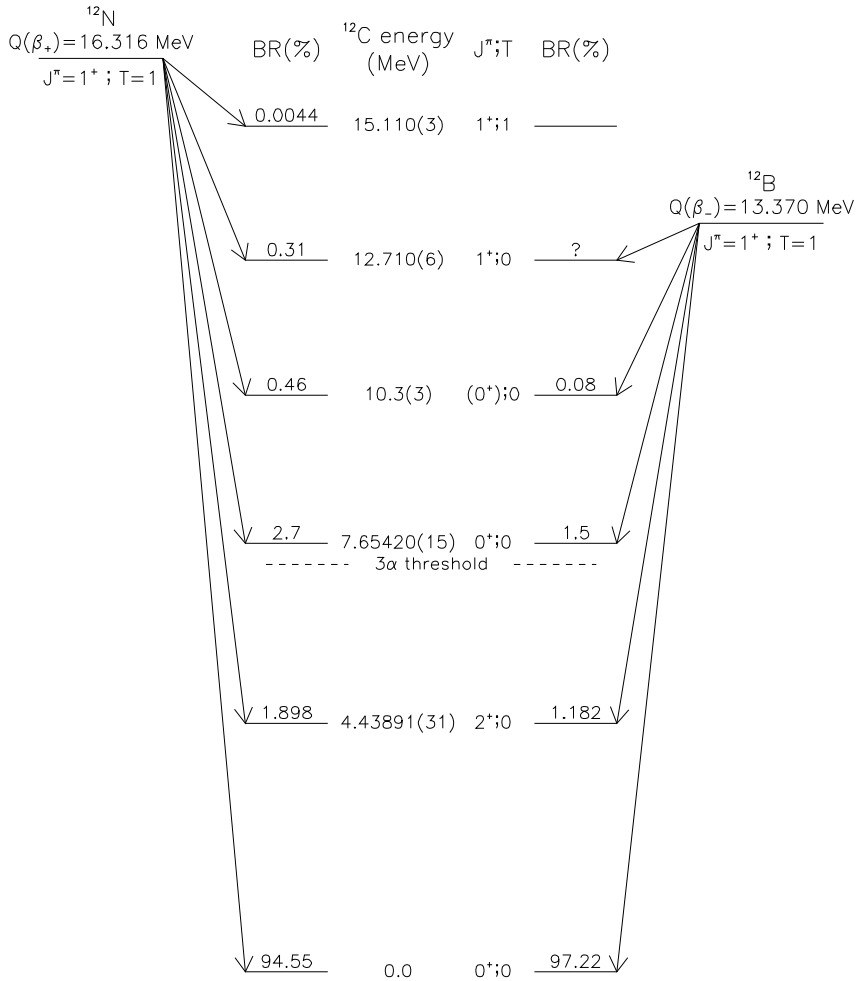

Figure 2.1.4: ^{12}C states populated in the beta decays of ^{12}N and ^{12}B. Branching ratios are stated according to Ajzenberg-Selove (1990).

(1966), who concluded that the state was either 0^+ or 2^+ and that the energy was 10.3(3) MeV.

In the studies of Cook et al. as well as in that of Schwalm & Povh, the states were detected through their breakup into three alpha particles. These alpha particles were detected and from this single alpha spectrum properties of the states was deduced. From these single particle spectra for example, Schwalm & Povh concluded that the 10.3 MeV state decayed by a sequential breakup, first into an alpha particle and the ^{8}Be ground state after which the ^{8}Be ground state would break up into two alpha particles. Of the three possibilities for j^π: 0^+, 1^+ and 2^+, only 0^+ and 2^+ is consistent with this breakup channel.

With the results of these two groups, Morinaga (1966) could describe the 10.3 MeV state in the same framework as his description of the Hoyle state (Morinaga, 1956). When understanding the Hoyle state as a prolate triple alpha cluster, one can imagine to make this state rotate around an axis through its center. The first such rotation would yield a spin of 2 of the resulting ^{12}C state and keep the positive parity. Such a 2^+ state is only the first of a number of rotational excitations of the Hoyle state, with the remaining coming in at higher and higher energies. We therefore describe it as the first member of *the rotational band* build on the Hoyle state.

For that reason, Morinaga assigned a spin-parity of 2^+ to the 10.3 MeV state. This interpretation has later on been quantified (Descouvemont & Baye, 1987), resulting in the prediction of a 2^+ state at 9 MeV in ^{12}C corresponding to 1.7 MeV above the triple alpha threshold. Following this prediction, the state has been included in a compilation of astrophysical nuclear reaction rates (Angulo et al., 1999), as will be discussed in detail in chapter 9. Because of this it is crucial, not only for the development of precise cluster calculations in the triple alpha continuum, but as well for the triple alpha reaction rate calculations, to obtain an experimental validation of the spin assignment of this particular state.

2.3 Multi particle detection

A very important goal for the studies presented in this dissertation is therefore to examine the so-called 10 MeV state and determine experimentally, which of the two possible assignments 0^+ and 2^+ is the correct one. These studies make use of a detection method where we—as in the previous experiments—detect the individual alpha particles from the breakup. Though in this way resembling the Schwalm & Povh (1966) experiment, an important development in detection methods (Bergmann et al., 2003b; Tengblad et al., 2004) makes it possible to detect all three alpha particles, their energies and directions, from the same ^{12}C breakup. Such experiments have been performed by our collaboration during the last five years at Igisol (Jyväskylä, Finland) and at Isolde (Cern, Switzerland). In all these experiments we have used segmented silicon detectors to detect the alpha particles. In the first two experiments (presented in: Fynbo et al., 2003, 2005) the setups consist of two detectors facing each other,

which allows us to detect all three alpha particles from the breakup if one of the three has sufficient energy to thrust the remaining two into the opposite detector when itself hitting one of the detectors. This gives a very high triple coincidence detection efficiency when the breakup proceeds through the ground state of ^{8}Be. Because the sum of the three energies is the energy in ^{12}C above the triple alpha threshold, this yields a direct measurement of the ^{12}C spectrum for breakup through the ^{8}Be ground state.

Though I analyzed the data from the ISOLDE experiment, this dissertation however will not include this analysis, since it is presented elsewhere (Diget, 2004; Diget et al., 2005). The focus will rather be on a new experiment where an improved setup is used. This setup consists of tree segmented silicon detectors, with which the detector setup covers a larger solid angle. This property of the improved setup is one of the main motivations for this new experiment, since it made possible the triple alpha coincidence detection of breakups through higher energies of the intermediate ^{8}Be nucleus. As will become evident in chapter 7, this will yield important information on this yet unseen breakup channel for the studied ^{12}C states.

2.4 Probing isospin (a)symmetry

Another key motivation for this experiment is to test the isospin symmetry (or asymmetry if present) between the two decaying nuclei ^{12}N and ^{12}B and their decay to the ^{12}C states. The two nuclei have opposite number of protons (Z) and neutrons (N) with $Z = 7$ and $N = 5$ for ^{12}N. In the shell model, mentioned in section 1.3, the single particle states for neutrons and protons are very similar. This means the two nuclei ^{12}N and ^{12}B look very similar on the quantum mechanical level, the two are isobaric analogue states. The effect of this is in turn, that the two beta decays are very similar. This symmetry is an example of the *isospin symmetry*, since the difference between the number of protons and neutrons sets the third component (T_3) of the isospin. As will be described in section 4.1 the aim of comparing these two decays was the prime motivation for using the IGISOL separator in Finland. The results of this comparison are presented in chapter 8.

2.5 Calorimetry

In the spring of this year, an alternative and completely different detection method has been applied (Pedersen et al., 2006) for such beta decay studies. In this experiment performed at KVI (University of Groningen, the Netherlands) a finely segmented detector was used as a calorimeter for the alpha particle energies.[2]

[2]Though our group is deeply involved in this experiment I did not participate in the actual data taking.

The beta decaying nuclei were implanted in the active part of the detector. When the nuclei decay, the beta delayed alpha particles deposit all of their energy in the detector, whereas the emitted beta particles escape the detector without depositing much energy, because the detector is thin and because of the segmentation. For a beta particle of for example 1 MeV, the average amount of energy deposited in the detector is thus only about 10 keV. This amount is found through a Geant4 simulation (Agostinelli et al., 2003). During my stay at Katholieke Universiteit Leuven (Belgium) in the spring of 2005, I made such simulations for the same detector which we used in other beta delayed particle emission experiments. In these we used the same method to study the beta decays of the two halo-nuclei ^{6}He (Crc, Louvain-la-Neuve, Belgium) and ^{11}Li (Triumf, Vancouver, Canada). Both decays have decay branches to continuum states that break up. With this method of detection, it is possible to measure the beta delayed triple alpha continuum spectrum all the way down to the Hoyle state. Though the data is very promising, however with the experiment being this recent, the analysis is still in its preliminary phase.

CHAPTER 3

R-Matrix theory

Ghosts, we tend to think, actually shouldn't be here but still once in a while they simply pop up somewhere. We often forget them but from time to time they get really nasty and interfere with us.

The challenge for theoretical nuclear physics is to understand and describe the structure of the excited ^{12}C states in terms of quantum mechanical wave functions. This structure however is *not* what we measure in an experiment. What we measure is a *quantum mechanical observable*, such as e.g. $E_{sum} = E_{\alpha_1} + E_{\alpha_2} + E_{\alpha_3}$. What is done in the following is to *interpret* the distribution of this observable in terms of states in ^{12}C, the decay of ^{12}N and ^{12}B to these states and the subsequent breakup of the states. To be more precise we use the R-Matrix theory to parameterize all processes that take place within a spherical reaction region with a radius of $a_c = r_0 \cdot (A_1^{1/3} + A_2^{1/3})$ where A_1 and A_2 are the number of nucleons in the two participating nuclei (in this case ^{4}He and ^{8}Be) as illustrated in figure 3.0.1. Here r_0 must be chosen so large that anything else but Coulomb interactions can be neglected outside the sphere. There is no universal size for the channel radius a_c, and it may thus differ for different breakup channels. One natural choice however for r_0 is the pion Compton wavelength, since the pion is the primary mediator of the nucleon-nucleon force (Feshbach & Kerman, 1967). For the charged pions this yields $\hbar/m_\pi c = 1.41\,\text{fm}$ (Eidelman et al., 2004). With

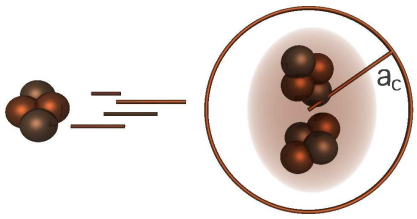

Figure 3.0.1: Reaction region for ^{12}C breakup to a ^{8}Be nucleus and an α particle. Channel radius a_c illustrated.

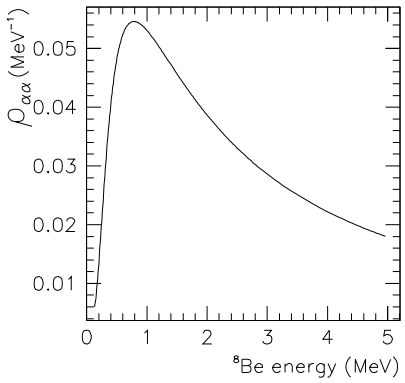

Figure 3.1.1: High energy tail of penetrability corrected Breit-Wigner distribution for the ^{8}Be(g.s.). Total distribution is normalized to 1.

this confinement of the reaction region the evolution of the wave function in the outer region can be described analytically using the Coulomb wave functions, while on the other hand some very complicated processes take place in the inner region with unknown wave functions and reaction mechanisms. For that reason the processes in this region cannot be described in the same exact manner, as is the case for the outer region, but must be parameterized in some way. The point of the R-Matrix theory is that it provides such a parameterization that is both successful in reproducing spectra for the observables and has parameters that can be interpreted physically in terms of state energies and transition matrix elements.

The success of quantum mechanics is to a large extent based on its precise predictions of such states and transition probabilities. These predictions are determined unambiguously, at least in principle. However because of the complexity of the quantum mechanical many body system approximations must be made and thus different competing theoretical descriptions may be available as is the case for the excited states of ^{12}C. Thus the goal for the experimental study is to provide restrictions on the states and involved transitions that may rule out some theories and favor others. When the states in question are well separated in energy, providing such information may be straight forward. When the states on the other hand are broad and overlapping or close to a threshold, the interpretation of experimental data can be more complex, and a model, such

as the R-Matrix theory, is needed.[1]

3.1 Interference and ghosts

As described in the introduction (section 1.2) interference is important if a process has two or more paths to proceed through and there is no way of gaining information on which of the paths were actually used. That is, if no (quantum mechanical) observable contains such information. This is exactly what happens if two states with no distinguishing quantum numbers in an intermediate nucleus overlap in energy and thereby both contribute significantly to the total reaction amplitude at a given energy. If this is the case, the two must be added coherently resulting in constructive or destructive interference depending on their relative phase in the complex plane.

Another issue regards the threshold effects appearing when a decaying state is very close to a threshold. The most striking threshold effect is the appearance of ghosts, where the shape of the state as seen in for instance a resonant scattering experiment is no longer the simple Breit-Wigner form:

$$\sigma(E) \propto \frac{\Gamma^2}{\left(E_\lambda - E\right)^2 + \left(\Gamma/2\right)^2}. \tag{3.1.1}$$

The ghost arises when the width (Γ) of the state is heavily energy dependent. In the high energy tail of the ^{8}Be ground state Breit-Wigner distribution (around 1 MeV), the width will for example increase drastically, since the Coulomb barrier can no longer confine the state so easily and the decay probability—i.e. the width—increases. As is seen from figure 3.1.1, this means the state at these energies behaves as a broad state, blowing up the tail of the distribution at the high energies where the width overcomes the decrease from the $\left(E_\lambda - E\right)^2$ denominator. Note that the exact position of this ghost depends on the energy dependence of the involved Coulomb barrier penetrabilities, and thereby depends on the probing reaction. It is therefore not surprising that Barker et al. (1967) and Becchetti et al. (1981) with their ^{9}Be$(p,d)^8$Be reaction experiments and Szczurek et al. (1991) using a ^{9}Be$(d,t)^8$Be experiment find a slightly different position of the ghost.

This effect is a general threshold effect and therefore applies to the ^{12}C Hoyle state as well. This will become evident in the following section, where it is seen that the Hoyle state besides dominating the low energy region has an important ghost. The Hoyle state ghost has previously been discussed by Wilkinson et al. (1963), and a general description of these threshold effects is given by Barker & Treacy (1962), a formalism that was as well applied in the analysis of the mentioned reaction experiments.

The effect of the strong energy dependence of the width is actually the same as that seen for the alpha decay in general, where the lifetime $\tau = \hbar/\Gamma$ is the

[1] Parts of the R-Matrix introduction given in this chapter can as well be found elsewhere (Diget, 2004).

most convenient observable. The alpha decay lifetime (τ) can be very long when the decay has a very low Q value, since the lifetime is determined primarily by the probability of penetrating the Coulomb barrier. This penetration depends strongly on energy, yielding a very wide span of the lifetimes ranging from micro seconds up to billions of years as is for instance seen in the thorium isotopes (Pfennig et al., 1998). The difference is that in the case of the Hoyle state and the ^{8}Be ground state the difference in lifetime is seen within a single state depending on at which energy the state is populated.

3.2 Beta delayed particle emission

The description of R-Matrix theory given in this section will follow the notation and description by Buchmann et al. (2001) and deals with beta decay to broad states and their subsequent breakup through a narrow exit channel, in this case the 91.8 keV (Tilley et al., 2004) ground state of ^{8}Be. A very detailed description of R-Matrix theory has been written by Lane & Thomas (1958). The theory will be described in the most general case and the connection between the general description and the well known Breit-Wigner shape of a state will be indicated.

The most general case is the case where ^{12}B and ^{12}N decay to several interfering levels in ^{12}C (denoted by Greek letters) the decay being either Fermi or Gamow-Teller decay ($x = F, GT$). These levels may then decay through several narrow channels (c). For this case the transition probability distribution for the channel c is given by:

$$w_c(E) = C^2 f_\beta \mathcal{P}_c \sum_{x=F,GT} \left| \sum_{\lambda\mu} g_{\lambda x} \gamma_{\mu c} A_{\lambda\mu} \right|^2 . \tag{3.2.1}$$

Here C is just a normalization constant that we have no need to worry about at the moment, $\mathcal{P}_c$ is the penetration factor for the decay through the channel c at the energy E, $g_{\lambda x}$ is the quantum mechanical matrix element for the x transition from ^{12}B to the state λ and $\gamma_{\lambda c}$ is the reduced partial width of the state λ to the channel c. Just as is the case for $g_{\lambda x}$, $\gamma_{\lambda c}$ is basically the matrix element between the state λ and the final state $^8\mathrm{Be} + \alpha$. $A_{\lambda\mu}$ is the (λ, μ) entry in *the level matrix* A, which is defined at each energy E by its inverse as:

$$\left(A^{-1}\right)_{\lambda\mu} = (E_\lambda - E)\delta_{\lambda\mu} - \sum_c \gamma_{\lambda c}\gamma_{\mu c}(\mathcal{S}_c - \mathcal{B}_c + i\mathcal{P}_c), \tag{3.2.2}$$

where E_λ is the R-Matrix energy parameter[2] of the level λ, $\mathcal{S}_c$ is the shift function at the energy E and $\mathcal{B}_c$ is the boundary condition parameter, a constant typically chosen such that $\mathcal{S}_c - \mathcal{B}_c = 0$ at one of the level energies E_λ. Both $\mathcal{P}_c(E)$, $\mathcal{S}_c(E)$ and $\mathcal{B}_c$ are real numbers and depend on the choice of r_0. They are found from the regular and irregular Coulomb wave functions and their derivatives. It

[2] E_λ is *not necessarily* the observed level energy, as will be discussed in section 3.2.1.

should not be surprising that the Coulomb wave functions are used since the basic assumption in the theory is that the only long range interaction is the Coulomb interaction.

A simple case is the case where the decaying nucleus being either ^{12}N or ^{12}B decays to only one level λ in ^{12}C with only one transition type (here Gamow-Teller). For this decay type the level matrix has only one entry, and the partial transition probability distribution is given by:

$$\begin{aligned} w_c(E) &= C^2 f_\beta g^2_{\lambda,GT} \frac{\mathcal{P}_c \gamma^2_{\lambda c}}{\left|(E_\lambda - E) - \sum_c \gamma^2_{\lambda c}(\mathcal{S}_c - \mathcal{B}_c + i\mathcal{P}_c)\right|^2} \\ &= \frac{1}{2} C^2 f_\beta g^2_{\lambda,GT} \frac{\Gamma_c}{\left(E_\lambda - E + \Delta\right)^2 + \left(\sum_c \Gamma_c/2\right)^2}, \end{aligned} \tag{3.2.3}$$

with the definitions (Lane & Thomas, 1958): $\Gamma_c(E) = 2\mathcal{P}_c\gamma^2_{\lambda c}$ and $\Delta(E) = -\sum_c \gamma^2_{\lambda c}(\mathcal{S}_c - \mathcal{B}_c)$. This reduces to the well known Breit-Wigner distribution with the corrections from Δ and the energy dependence of Γ_c. These corrections are small when the state is narrow.

Equation 3.2.3 may be used for two non-interfering states by simply adding the contributions from the different levels incoherently. This is the case if we assume only one state besides the 0^+ Hoyle state to contribute to the decay spectrum, and furthermore assign spin and parity 2^+ to that state, since such two states cannot interfere. On the other hand if the second state is a 0^+ state or if at least three 0^+ and 2^+ states in total contribute, two or more states will have the same spin an can thus interfere with each other. In which case the general formalism (equation 3.2.1) must be used to find the contribution from each individual spin component after which they are added incoherently.

3.2.1 Observed parameters

When the formalism presented in equation 3.2.1 has been used to identify the states fed in the decay and the properties of those states, we are in a position to extract the physical energies and widths of the states from their corresponding R-Matrix level parameters.

The first step in doing so is to be able to transform the R-Matrix parameters between different choices of the boundary condition parameter $\mathcal{B}_c$. That is we wish to transform the parameters E_λ, $\gamma_{\lambda c}$, and $g_{\lambda x}$ corresponding to $\mathcal{B}_c$ into the parameters E'_λ, $\gamma'_{\lambda c}$, and $g'_{\lambda x}$ corresponding to $\mathcal{B}'_c$. The reason why this is necessary can be seen in equation 3.2.3, where it is seen that peak of the state λ is positioned at the energy where $E_\lambda - E + \Delta(E) = 0$. What is done in the following transformation is to find $\mathcal{B}_c$ such that $\Delta(E) = 0$ at the transformed peak energy E'_λ, and for this boundary condition parameter find the new set of R-Matrix parameters. The transformation is deduced and described in detail by Barker (1972) and the results are given by Buchmann et al. (2001) as well. The transformation is given here for the most general case, that is many level, many channel.

To perform the transformation we let C be the matrix with the following entries:

$$C_{\lambda\mu} = E_\lambda \delta_{\lambda\mu} - \sum_c \gamma_{\lambda c}\gamma_{\mu c}\left(\mathcal{B}'_c - \mathcal{B}_c\right). \tag{3.2.4}$$

Since the matrix is a real symmetric matrix we may find a real orthogonal matrix K that diagonalizes C, that is: $K\,C\,\widetilde{K} = D$ where D is diagonal. The rows of K are the normalized eigenvectors of C and the diagonal elements of D the corresponding eigenvalues.[3] From this the new parameter values may be found using:

$$E'_\lambda = D_{\lambda\lambda}\,, \qquad \gamma'_c = K\gamma_c\,, \qquad g'_x = Kg_x, \tag{3.2.5}$$

where γ_c and g_x are the column vectors with entries $\gamma_{\lambda c}$ and $g_{\lambda x}$ respectively. What we need is to find the parameters corresponding to the boundary condition parameter that fulfills: $\mathcal{S}_c(E'_\lambda) - \mathcal{B}'_c = 0$. By construction the fitted parameters fulfill this requirement for the energy of the first state ($\lambda = 1$), and what we should find is the corresponding parameter set for $\mathcal{B}'_c = \mathcal{S}_c(E'_\mu)$ for $\mu \neq \lambda$. But since we do not know a priori what this new level energy is, we must find it iteratively. The first choice for $\mathcal{B}'_c$ is: $\mathcal{B}'_c = \mathcal{S}_c(E_\mu)$ resulting in a new value E'_μ. After this we choose: $\mathcal{B}''_c = \mathcal{S}_c(E'_\mu)$ and find the value E''_μ etc. This turns out to converge rapidly towards the energy that fulfills the requirement. The limit of this iteration is therefore the observed level energy E^o_μ.

To find the observed width we make use of the description of Barker & Treacy (1962) where the basic assumption is that the shift function $\mathcal{S}_c$ is linear around the observed resonance energy. From this one may find the observed partial width:

$$\Gamma^o_{\lambda c} = 2\mathcal{P}_c(E^o_\lambda)\gamma^2_{\lambda c}\left(1 + \gamma^2_{\lambda c}\frac{\mathrm{d}}{\mathrm{d}E}\mathcal{S}_c(E)\right)^{-1}_{E=E^o_\lambda}, \tag{3.2.6}$$

where $\Gamma_{\lambda c} = 2\mathcal{P}_c(E^o_\lambda)\gamma^2_{\lambda c}$ is the "true width" of the state. This method is used in the following to find the values and uncertainties of the observed quantities E^o_μ and $\Gamma^o_{\lambda c}$.

It should be noted that this relation between R-Matrix level parameters and the observed parameters for the states opens up for an alternative to fitting the level parameters. Namely to have the observed parameters as fitting parameters and making the reverse translation from observed parameters to level parameters before calculating the theoretical spectrum. This method yields the same results, but can be more convenient for estimating errors on observed parameters and applying restrictions on the individual parameters. The application of such a parameterization of the R-Matrix theory has been described by Brune (2002). In the analysis presented in the following chapters however the standard parameterization will be used.

[3] No requirements are needed on the sign of the eigenvectors in K. This is because changing the sign of e.g. eigenvector λ would only change the sign of $\gamma'_{\lambda c}$ and $g'_{\lambda x}$ as seen from equation 3.2.5 and because only the sign of $\gamma'_{\lambda c}{\cdot}g'_{\lambda x}$ is of physical importance.

3.2.2 Branching ratios and B_{GT} values

There exist two fundamentally different ways of describing the way a beta decay populates individual states in the daughter nucleus, namely branching ratios to different energy regions and B_{GT} values to different states. The direct counting of measured intensity in different energy regions of the spectrum is completely model independent but it cannot necessarily be compared directly to theoretical models. The division of strength into different spin components and the individual contributing states on the other hand is much more interesting as seen from a theoretical point of view. The extraction of this information from the experimental spectrum however can be model dependent, as is seen in the following where two broad interfering states both give important contributions. When the involved states in the daughter nucleus are narrow, the two methods however are directly related namely through the ft value.

The partial half life $t_{1/2;\lambda}$ for a beta decay to a state λ is directly related to the beta decay phase space f_β and the transition matrix elements M_F and M_{GT} for Fermi and Gamow-Teller decay respectively by:

$$f_\beta t_{1/2;\lambda} = \frac{B}{|M_F|^2 + \frac{g_A^2}{g_V^2}|M_{GT}|^2} = \frac{B}{B_F + \frac{g_A^2}{g_V^2}B_{GT}}, \tag{3.2.7}$$

where the constants $B = 6145(4)\,\mathrm{s}$ and $|g_A/g_V| = 1.266(4)$ have been determined for example by Towner et al. (1995) and Schreckenbach et al. (1995). Furthermore since the investigated ^{12}C states are isospin 0 states and the decaying nuclei have isospin 1, the Fermi transition does not couple the states to any of the two mother-nuclei.[4] Because of this, B_F in equation 3.2.7 is 0 and the relation simplifies to

$$B_{GT} = \frac{g_V^2}{g_A^2}\frac{B}{f_\beta t_{1/2;\lambda}} \tag{3.2.8}$$

allowing us to easily calculate the B_{GT} value for these decays.

The phase space factor f_β is very energy dependent ($f_\beta \propto Q^5$ for $Q \gg m_\beta c^2$) but can be calculated to an accuracy of one per mill by using the parameterizations given by Wilkinson & Macefield (1974). This relates to the branching ratios through

$$f_\beta t_{1/2;\lambda} = f_\beta \frac{t_{1/2}}{\mathrm{BR}_\lambda} \tag{3.2.9}$$

when the branching ratios to the individual levels BR_λ are well defined experimentally, that is when the contributing states are narrow. This is for instance the case for the 12.7 MeV state.

With this in hand, we can proceed to the case where the states are broad and possibly even interfering and therefore cannot be easily separated. The first

[4] The lowest lying $T = 1$ state is at 15.11 MeV, and is not detected here. The branching ratio to this state in the ^{12}N decay is $4.4 \cdot 10^{-3}$% and it primarily decays through gamma decay.

possibility of dividing the spectrum into individual energy regions is done by simply integrating the total decay probability defined as:

$$w(E) = \sum_{j_a} w^{j_a}(E) = \sum_{j_a,c} w_c^{j_a}(E) \tag{3.2.10}$$

where j_a is the ^{12}C spin, and $w_c^{j_a}(E)$ is defined for each spin as in equation 3.2.1. For convenience when calculating B_{GT} values in the following, we choose the global normalization constant C such that:

$$\frac{\ln 2}{t_{1/2}} = \int_0^\infty w(E)dE, \tag{3.2.11}$$

as done by Barker (1969). With this we get the branching ratios by integrating over the region of interest (ΔE) as:

$$\mathrm{BR}_{\Delta E} = \int_{\Delta E} w(E)dE \Big/ \int_0^\infty w(E)dE = \frac{t_{1/2}}{\ln 2} \int_{\Delta E} w(E)dE \tag{3.2.12}$$

Or for a single spin component j_a:

$$\mathrm{BR}^{j_a} = \frac{t_{1/2}}{\ln 2} \int w^{j_a}(E)dE \tag{3.2.13}$$

For branching ratios relative to a known state we scale with the partial half life to that state instead of the total half life.

For contributions from individual states we will follow Barker & Warburton (1988) in defining the decay probability to a state λ as:

$$w_\lambda^{j_a}(E) = C^2 f_\beta \sum_c \mathcal{P}_c \left| \sum_\mu g_{\lambda,GT}^{j_a} \gamma_{\mu c}^{j_a} A_{\lambda\mu}^{j_a} \right|^2 \tag{3.2.14}$$

where the summation over $x = F, GT$ (equation 3.2.1) has been omitted for simplicity, since the decays here are purely Gamow-Teller decays. As noted by Barker & Warburton $g_{\lambda,GT}$, $\gamma_{\mu c}$ and $A_{\lambda\mu}$ as used here must be calculated for the set of R-Matrix parameters corresponding to $\mathcal{B}_c = \mathcal{S}_c(E_\lambda)$. How to get these values was described in section 3.2.1. The branching ratio to the state λ is then calculated by integration of equation 3.2.14:

$$\mathrm{BR}_\lambda^{j_a} = \frac{t_{1/2}}{\ln 2} \int w_\lambda^{j_a}(E)dE \tag{3.2.15}$$

This corresponds to the integral of the two dashed lines ($\lambda = 1$) and ($\lambda = 2$) in figure 3.2.1. Note however that this is *not* an exact division of the total strength, as can be seen in the figure, where the sum of the two is not an exact reproduction of the total strength function. In this case however the correspondence is very good. Though not fully, equation 3.2.15 does take interference into account

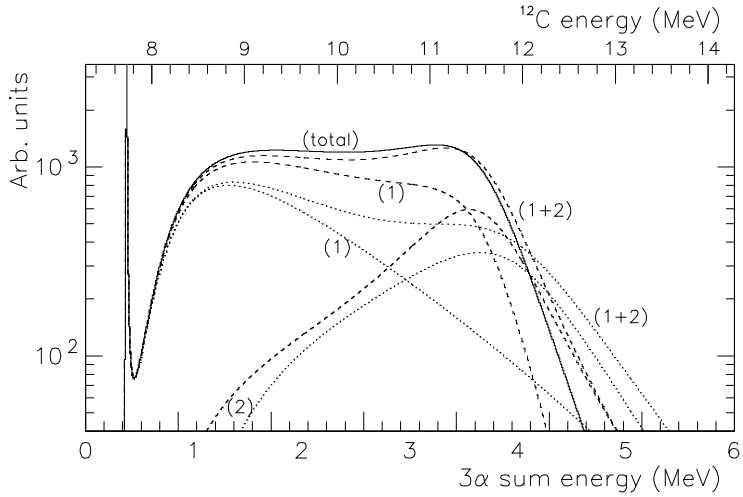

Figure 3.2.1: An example of two interfering states. The Hoyle state with its ghost (1) and state at higher energy (2), both with $J^\pi = 0^+$. Dotted lines are the two states in the single level approximation and an incoherent addition of the two; the dashed lines are the individual state contributions as described in equation 3.2.15 and the sum of the two; whereas the solid line is the total intensity including the full interference (equation 3.2.1). Note that this is not the best fit description of the experimental spectrum, but should merely illustrate the properties of the interference.

to some degree. This can be seen if we from the parameters corresponding to level λ find its contribution to the total strength using the single level approximation (equation 3.2.3). This is shown in figure 3.2.1 where for example the Hoyle state ghost (dotted line 1) is very pronounced. This has previously been used to describe the individual level branching ratios (Barker, 1969), but as has more recently been noted this is not a good approximation (Barker & Warburton, 1988), which can as well be seen from the figure where it is evident that the two dotted lines do not at all sum up to the total spectrum.

To the extent that $\sum_\lambda \mathrm{BR}_\lambda^{j_a} \approx \mathrm{BR}^{j_a}$ as described in equation 3.2.15 is a good approximation, we can use this to calculate approximate values for the Gamow-Teller matrix elements for the two beta decays to the individual levels. This is also described by Barker & Warburton (1988). Following their argument[5] we can

[5]Slightly modified to explicitly state the parameters we will need in the following analysis.

see that the branching ratio (equation 3.2.15) can be rewritten to:

$$\begin{aligned} \mathrm{BR}_\lambda^{j_a} &= \frac{t_{1/2}}{\ln 2} C^2 \left(g_{\lambda,GT}^{j_a}\right)^2 \int f_\beta \sum_c \mathcal{P}_c \left| \sum_\mu \gamma_{\mu c}^{j_a} A_{\lambda\mu}^{j_a} \right|^2 dE \\ &= \frac{t_{1/2}}{\ln 2} C^2 \left(g_{\lambda,GT}^{j_a}\right)^2 f_\lambda^{j_a} J_\lambda^{j_a} \end{aligned} \tag{3.2.16}$$

with

$$J_\lambda^{j_a} = \int \mathcal{P}_c^{j_a} \left| \sum_\mu \gamma_{\mu c}^{j_a} A_{\lambda\mu}^{j_a} \right|^2 dE. \tag{3.2.17}$$

if we define the average phase space factor $f_\lambda^{j_a}$ for the state as:

$$f_\lambda^{j_a} = \int f_\beta \sum_c \mathcal{P}_c \left| \sum_\mu \gamma_{\mu c}^{j_a} A_{\lambda\mu}^{j_a} \right|^2 dE \Big/ J_\lambda^{j_a} = I_\lambda^{j_a} \Big/ J_\lambda^{j_a}. \tag{3.2.18}$$

$I_\lambda^{j_a}$ will turn out to be convenient in section 8.6. When rearranging equation (3.2.16) this yields the following relation for the "ft" value:

$$\frac{1}{f_\lambda^{j_a} t_{1/2;\lambda}} = \frac{\mathrm{BR}_\lambda^{j_a}}{f_\lambda^{j_a} t_{1/2}} = \frac{C^2}{\ln 2} \left(g_{\lambda,GT}^{j_a}\right)^2 J_\lambda^{j_a}. \tag{3.2.19}$$

When interpreting this "ft" value as an inverse of the B_{GT} value according to equation 3.2.8 we get the following B_{GT} values:

$$B_{GT;\lambda}^{j_a} = \frac{g_V^2}{g_A^2} C^2 \frac{B J_\lambda^{j_a}}{\ln 2} \left(g_{\lambda,GT}^{j_a}\right)^2 \tag{3.2.20}$$

Each of these is again calculated for each level using the R-Matrix parameters corresponding to $\mathcal{B}_c = \mathcal{S}_c(E_\lambda)$ for that particular level. This means the B_{GT} value for a state μ relative to that of a state λ is found as:

$$\frac{B_{GT;\mu}}{B_{GT;\lambda}} = \frac{|M_{GT;\mu}|^2}{|M_{GT;\lambda}|^2} = \frac{J_\mu^{j_a}}{J_\lambda^{j_a}} \frac{{g_{\mu,GT}}^2}{{g_{\lambda,GT}}^2}. \tag{3.2.21}$$

In the preceding the B_{GT} were found by assigning an average f value for the level λ and using this to calculate an "ft" value for the decay to that particular level. We should however be aware that since the f-factor of the beta decay to this state varies a lot over the energy range of the state, the ft value is not really the beta phase space factor times the partial half life of the decaying nucleus to that particular state as in the traditional understanding of the ft value. So the ft value should rather be seen as just the inverse of the B_{GT} to the state apart from the scaling factor, and the most appropriate parameter to discuss for these broad states is thus the B_{GT} value. The final results presented in chapter 8 however will be presented as absolute values of log ft, to allow a direct comparison with previous measurements.

3.2.3 Parameter restrictions

The B_{GT} values denotes the strength of the coupling between two states by the Gamow-Teller operator. The total Gamow-Teller strength from a nucleus is denoted:

$$S(GT,\beta^+) = \sum_\lambda B_{GT;\lambda}(\beta^+) \text{ and } S(GT,\beta^-) = \sum_\lambda B_{GT;\lambda}(\beta^-), \tag{3.2.22}$$

for beta plus and minus respectively summed over all final states λ. Note here, that it is the *total* strength, not only the strength within the available energy window for beta decays, so for example strength for neutrino induced reactions with negative Q value should be taken into account as well. The total strength will always comply with the Gamow-Teller sum rule:

$$S^-_{GT} - S^+_{GT} = 3(N-Z) \tag{3.2.23}$$

where N is the number of neutrons in the initial nucleus in the decay (or reaction) and Z is the number of protons. This relation is exact as described for example by Gaarde et al. (1980) and Goodman (1990) as long as all final states are included.

If we are to use this to place restrictions on one of the transitions, we must know something about the other transition. This is the case for example for very neutron rich nuclei, where there are no available single particle states for the β^+ transition. Because of this, the β^+ strength is very close to zero and the total β^- strength can be found from the Gamow-Teller sum rule.

In the decay of ^{12}N, the situation is just the opposite though not as extreme. This nucleus has $N = 5$ and $Z = 7$, and has therefore $3(N-Z) = -6$. The nucleus has in its ground state a filled $1s$ shell for both protons and neutrons and furthermore 3 neutrons and 5 protons in the $1p$ shell, where 6 single particle states are available for each of the two kinds of nucleons $(4\times 1p_{3/2}, 2\times 1p_{1/2})$. This means that three states are available in the $1p$ shell for the β^+ transition whereas only one is available for the β^- transition. This makes it reasonably safe to assume that the β^+ strength is significantly larger than the β^- strength. To be conservative, we will assume it to be a factor of two: $S^-_{GT} \leq \frac{1}{2}S^+_{GT}$, in which case we get the following inequality for the β^+ strength:

$$S^+_{GT} = 2(S^+_{GT} - S^-_{GT} + S^-_{GT} - \frac{1}{2}S^+_{GT}) = 2(6 + S^-_{GT} - \frac{1}{2}S^+_{GT}) \leq 12. \tag{3.2.24}$$

This will prove useful in section 6.3.5.

The Gamow-Teller sum rule described above regards the beta decay into ^{12}C states. For the decay of these states on the other hand, we can similarly place restrictions on the decay matrix elements, the reduced widths: $\gamma'_{\lambda\alpha}$. The reduced width of a state can be converted to the dimensionless reduced width (Lane & Thomas, 1958, pg. 324):

$$(\theta'_{\lambda\alpha})^2 = \left(\frac{\hbar^2}{\mu_c a_c^2}\right)^{-1} (\gamma'_{\lambda\alpha})^2. \tag{3.2.25}$$

Here μ_c is the reduced mass of the two particle system in the outgoing channel (in this case the $^8\mathrm{Be} + \alpha$ system) and a_c is the channel radius. This dimensionless reduced width ($\theta'_{\lambda\alpha}$) cannot exceed 1 (the Wigner limit), since it may be understood as the probability for decaying into this final state channel, when all effects of phase space factors are removed. This restriction will as well be helpful in section 6.3.5.

3.3 Broad exit channel

Having dealt with the case of a narrow outgoing breakup channel, we will proceed to the case where the breakup of a narrow state proceeds through a broad intermediate state. This is for instance the case for the beta decay to the ^{12}C 1^+ state at 12.7 MeV. This state cannot breakup through the 0^+ ground state of ^{8}Be, since such a breakup would imply an $L = 1$ angular momentum for the $^8\mathrm{Be}+\alpha$ pair yielding a change of parity in contradiction with all involved parities being positive. The description here will largely follow that of Balamuth et al. (1974) and Fynbo et al. (2003), though the notation has been adjusted to ease the generalization to the description of a broad state in ^{12}C decaying into a triple alpha final state through broad intermediate levels of ^{8}Be.

For a three body breakup it is convenient besides the laboratory system $\vec{r}_1, \vec{r}_2, \vec{r}_3$ to define a coordinate system $\vec{R}, \vec{s}_{1-23}, \vec{s}_{2-3}$ as done by Ohlsen (1965). Here the three vectors respectively are the center of mass of the three particles; the position of the first emitted alpha[6] with respect to the remaining two; and the position of the second alpha relative to the third. With these definitions, the energy corresponding to the latter two coordinates are E_{1-23} and E_{2-3}, yielding $E_{1-23} = E_\lambda - E_{2-3}$ with E_λ as the total energy of the three alpha particles, that is the energy of the decaying ^{12}C state. Ohlsen also describes how the pure three particle phase space determined entirely by the statistical energy distributions is proportional to $\sqrt{E_{2-3}E_{1-23}}$, if we assume that no physical interaction or intermediate two particle states play a role.

With this we are ready to proceed to the interaction altering the three particle phase space distribution. This can be described as a weight associated with any point in phase space. This weight factor is found as

$$W(E_{2-3}, \Omega_1, \Omega_{1-23}) \propto \sum_{m_a} |f_{j_a m_a, \lambda}(E_{2-3}, \Omega_1, \Omega_{1-23})|^2$$

where the point in three particle phase space is defined by the energy in the secondary breakup, the direction of the first emitted alpha particle Ω_1 and the direction of the second breakup with respect to the first emitted alpha particle

[6] We will soon deal with the problem of defining which of the three was emitted first.

Ω_{1-23}. In this the amplitude f consists of an angular part and an energy part:

$$\begin{aligned} f_{j_a m_a,\lambda} &= \sum_{m_b} \phi\left(\Omega_1, \Omega_{1-23}\right) \xi\left(E_{2-3}\right) \\ \phi\left(\Omega_1, \Omega_{1-23}\right) &= \left(l m j_b m_b | j_a m_a\right) Y_l^m\left(\Theta_1, \Phi_1\right) Y_{l'}^{m_b}\left(\Theta_{1-23}, \Phi_{1-23}\right) \\ \xi\left(E_{2-3}\right) &= \left(E_{1-23} E_{2-3}\right)^{-1/4} \; e^{i(\omega_l - \phi_l)} \; \sqrt{2\mathcal{P}_l\left(E_{1-23}\right)} \gamma_{\lambda\alpha}^{j_a} \\ &\quad \cdot \; e^{i(\omega_{l'} - \phi_{l'})} \; \rho_{j_b}^{1/2}\left(E_{2-3}\right), \end{aligned} \tag{3.3.1}$$

where ρ should be interpreted as

$$\rho_{j_b}^{1/2}\left(E_{2-3}\right) = \frac{\sqrt{2\mathcal{P}_{l'}\left(E_{2-3}\right)} \gamma_{\kappa\alpha}^{j_b} A_{\kappa\kappa}^{j_b}\left(E_{2-3}\right)}{\left[\int_0^\infty 2\mathcal{P}_{l'}\left(E'_{2-3}\right) \left(\gamma_{\kappa\alpha}^{j_b}\right)^2 \left|A_{\kappa\kappa}^{j_b}\left(E'_{2-3}\right)\right|^2 dE'_{2-3}\right]^{1/2}}, \tag{3.3.2}$$

Here j_a, m_a and $\gamma_{\lambda c}^{j_b}$ refers to the spin and reduced width of the ^{12}C state in play, whereas j_b, m_b and $\gamma_{\kappa c}^{j_b}$ refers to the properties of the intermediate state in ^{8}Be through which the breakup proceeds. In both cases we assume for the time being that only one state contributes in each case. For convenience these are denoted λ and κ for ^{12}C and ^{8}Be respectively. The angular momenta l and l' are those of the first and second breakup respectively. l' is of course just the spin j_b of the intermediate state. For both angular momenta $\omega_l - \phi_l$ is the Coulomb minus hard sphere phase shift corresponding to the two particle scattering. The Clebsch-Gordan coefficients $(l m j_b m_b | j_a m_a)$ and the spherical harmonics $Y_l^m(\Theta, \Phi)$ as a function of the polar (Θ) and azimuthal (Φ) angles are both calculated using the Cernlib program package (Shiers, 1996). With the above definition of $\rho_{j_b}^{1/2}$ and because we assume only one contributing state with spin j_b, $\rho_{j_b} = \left|\rho_{j_b}^{1/2}\right|^2$ is simply the Breit-Wigner distribution of the ^{8}Be state (equation 3.1.1) normalized and taking into account the corrections from Δ and the energy dependence of the width as seen in equation 3.2.3. The energy at which the penetrability should be evaluated is still the available energy of the first breakup, but since this now depends on the energy available in the secondary breakup it depends on which pair is assigned to be the ^{8}Be alphas, and it must therefore be included in the amplitude before taking the norm squared to get the weight.

3.3.1 Symmetrization and simulation

Usually the angular part and the energy part uncouple, and we are left with an energy distribution and an angular distribution in the final weight. This is the case in the decay through the ^{8}Be ground state and was the reason why there was no reason to worry about the angular distributions, since they uncoupled from the energy distribution and furthermore they were isotropic since the intermediate ^{8}Be state was a spin 0 state.

In the present case however the two distributions couple. This is because there is one element missing so far in the description of the weight. This has to

do with the question: Which of the three alphas are the first emitted alpha. The answer to this is: There is no way of telling. This means that for a given triple of alpha energies E_1, E_2, E_3, any pair among the three can be identified as the ^{8}Be pair, so for any observed event we have three possible paths contributing to the overall amplitude, and since they must be added coherently, the contributions from the three paths interfere. For this reason the weight is actually given by:

$$W(E^i_{2-3}, \Omega^i_1, \Omega^i_{1-23}) \propto \sum_{m_a} \left| \sum_{i=1}^{3} f_{j_a m_a, \lambda}(E; E^i_{2-3}, \Omega^i_1, \Omega^i_{1-23}) \right|^2 , \tag{3.3.3}$$

where i denotes the choice of the first emitted alpha, and all energies and angles are defined according to that choice. The positive signs in this sum stems from the fact that the alpha particles are bosons. Because of this the amplitude (under the norm squared) must be symmetric under interchange of any pair of the alphas.

Because of this entanglement between the angular and energy distribution, we cannot describe the weight as a simple product of one dimensional distributions, but must treat the entire three particle phase space at once. The total weight distribution is here the product of W and the pure three particle phase space, and is scaled to have a maximum of 1. This weight is best investigated using a Monte-Carlo simulation where the three particle phase space is sampled with the Von Neumann sampling method (Eidelman et al., 2004). Three particle breakups are therefore generated using the CERNLIB routine GENBOD. To each generated breakup GENBOD assigns the corresponding pure three particle phase space weight allowing a calculation of the total weight at that point of phase space. With this in hand we are ready to use the Von Neumann sampling method where a random number x is generated from a uniform $[0, 1]$ distribution. If the weight exceeds x the breakup is accepted as a physical breakup event. Though not very efficient for distributions where sharp peaks come into play, the Von-Neumann sampling is the best choice here, since the distributions are generally broad. Furthermore the distributions depend on the assumptions made on the involved spin and angular momenta (j_a, j_b and l), so a sampling optimized for one specific distribution is not applicable.

3.4 Phase space integrated spectrum

With the phase space distributions in hand, we are ready to proceed towards an understanding of the spectrum in ^{12}C for such a broad breakup channel. That is, the spectrum for broad interfering states in ^{12}C.[7] As in the preceding section, we will need the weight at any point of phase space but now for any sum energy E of the three alpha particles. Once again we have $f_{j_a m_a}$ as:

$$f_{j_a m_a} = \sum_{j_b l m_b} \phi\left(\Omega_1, \Omega_{1-23}\right) \xi\left(E, E_{2-3}\right) \tag{3.4.1}$$

[7] In the development of this application of R-Matrix theory, I owe special thanks to Fred Barker for his important help and feed back in the description as well as in notation.

except we must now as well sum over all possible spins (j_b) in the intermediate nucleus ^{8}Be and different values of l in the case that more than one angular momentum of the first breakup can contribute. From this we can again derive the weight now as a function of the sum energy E as well, as long as we remember the distortion from the beta decay phase space (f_β) and the possibility of more than one contributing spin of ^{12}C:

$$W(E, E_{2-3}, \Omega_1, \Omega_{1-23}) \propto f_\beta\left(Q - E\right) \sum_{j_a m_a} \left| f_{j_a m_a, \lambda}(E_{2-3}, \Omega_1, \Omega_{1-23}) \right|^2, \quad (3.4.2)$$

where the different spins of ^{12}C are again summed incoherently. With this we can calculate the ^{12}C spectrum as a function of E by integrating over all the other parameters.

In equation 3.4.1 the angular part (ϕ) is exactly as in the preceding section whereas the energy dependent part (ξ) must now as well take into account the energy distribution in ^{12}C with contributions from different interfering states:

$$\begin{aligned} \xi\left(E, E_{2-3}\right) &= e^{i(\omega_l - \phi_l)} \sum_{\mu\lambda} g^{j_a}_{\lambda, GT} \gamma^{j_a}_{\mu j_b l} A^{j_a}_{\lambda\mu}\left(E\right) \sqrt{2\mathcal{P}_l\left(E_{1-23}\right)} \\ &\quad \cdot\ e^{i(\omega_{l'} - \phi_{l'})}\ \rho^{1/2}_{j_b}\left(E_{2-3}\right). \end{aligned} \quad (3.4.3)$$

Here the dependence on E is through the penetrability $\mathcal{P}_l$ and the level matrix $A_{\lambda\mu}$ as was the case in the decay through the narrow ^{8}Be ground state (equation 3.2.1). The level matrix however is not quite the same as before (equation 3.2.2). It still has the same structure, but the channels c that we sum over are more complicated. For the level matrix we will therefore use:

$$\begin{aligned} &\left(A^{j_a}(E)^{-1}\right)_{\lambda\mu} = (E_\lambda - E)\delta_{\lambda\mu} \quad (3.4.4) \\ &- \textstyle\sum_{j_b l} \int_0^\infty \gamma^{j_a}_{\lambda j_b l} \gamma^{j_a}_{\mu j_b l} \left(\mathcal{S}_l(E_{1-23}) - \mathcal{B}_{j_b l} + i\mathcal{P}_l(E_{1-23})\right) \rho_{j_b}(E_{2-3}) dE_{2-3}, \end{aligned}$$

where once again the boundary condition parameter is chosen such that $\Delta_{j_b l}$ is zero at an energy $E = E_\lambda$ for one of the ^{12}C levels λ. In this case $-\Delta_{j_b l}$ is the real part of the integral.

3.4.1 Integration and symmetrization

We are now ready for the integration over the five coordinates, one energy and four angles: E_{2-3}, Θ_1, Φ_1, Θ_{1-23} and Φ_{1-23}. This could be a terrible integral to evaluate, since it is five dimensional and the integrated function is itself heavy to calculate. There are however ways to make it at least somewhat simpler. Firstly, we should note that since the ^{12}C nucleus is not populated in a polarized superposition of m_a values, the first alpha is emitted isotropically, when averaging over m_a. This makes the integral over Θ_1 and Φ_1 contribute by just a factor of 4π. Similarly the second breakup is uniform over the azimuthal angle Φ_{1-23}, contributing with just a factor of 2π. To ease the calculation further, tables are

made of the real and imaginary parts of the integral in equation 3.4.4 for all possible combinations of j_a, j_b and l, excluding the constants $\gamma^{j_a}_{\lambda j_b l}\gamma^{j_a}_{\mu j_b l}$, that may differ from one level to the other. During the integration, the values are found from interpolating in these tables, using a linear interpolation for the shift function (Δ) and logarithmic interpolation for the penetrability ($\mathcal{P}$). Similarly the penetrability $\mathcal{P}_l(E_{1-23})$; the penetrability and shift function hidden in $\rho_{j_b}(E_{2-3})$; and the phase shifts ω_l, ϕ_l are calculated using interpolation in tables created before the integration is initiated. The remaining two-dimensional integration is performed using DCUHRE, an adaptive multidimensional integration routine by Berntsen et al. (1991a,b).

As noted in the preceding, this integration is performed without symmetrization of the amplitude. What should actually be done is to symmetrize the amplitude and only then do the integration. The reason why this is not done is that the integration is most conveniently formulated as an integration over E_{2-3}, Θ_1, Φ_1, Θ_{1-23} and Φ_{1-23}, which assumes a specific alpha particle as the first emitted, precluding the symmetrization. Though this has not yet been done, it could prove possible to change the integration parameters by substitution, and thereby integrate over the parameters $x = \sqrt{3}\left(E_1 - E_2\right)/E$ and $y = \left(2E_2 - E_1 - E_3\right)/E$ these two parameters describe uniquely the three particle breakup, apart from three angles describing the orientation in space which as above can be integrated out by hand. The two parameters x and y will be discussed further in section 4.2.2 and chapter 7, since they are essential in the definition of the so-called Dalitz plot.

CHAPTER 4

Experimental setup

4.1 Production of radioactive isotopes

To use beta decay as a probe of the triple alpha continuum, we must be able to produce the beta decaying isotopes and be ready to detect the breakup when the nuclei decay. This is not straight forward since the half lives are just 11 ms and 20 ms for ^{12}N and ^{12}B respectively (Ajzenberg-Selove, 1990). To handle such short lived nuclei we use a technique developed during the last half of the 20$^{\text{th}}$ century, the ISOL method an acronym for *Isotope Separation On-Line*. The first development of this method took place in Copenhagen at the Niels Bohr Institute 55 years ago (Kofoed-Hansen & Nielsen, 1951) where neutron rich Kr isotopes were produced in fission, separated and the half lives of the isotopes and their daughters measured. This was done for half lives down to 10 s and activity was seen even for isotopes with a faster decay.

This method was in sharp contrast to the so-called SRAFAP technique[1] where the isotopes were handled by hand from production through separation to the detection of their decay. Just two years earlier (Koch et al., 1949) the same group was therefore limited to studying isotopes with half lives of the order of half an hour, since this was the shortest time in which such a separation could be made.

[1] Students Running As Fast As Possible (Herrmann, 1988; Kronenberg, 2001).

Reaction	Target	Beam	Ions	Time	Yield
$^{12}C(p,n)^{12}N$	1400 µg/cm^2;^{12}C	28 MeV;25 µA;p	0.11G	103h	300/s
$^{11}B(d,p)^{12}B$	500 µg/cm^2;^{11}B	10 MeV;10 µA;d	0.85G	58h	4000/s

Table 4.1.1: Production reactions for ^{12}N and ^{12}B. Produced number of ions, effective beam time and estimated yield is given for the part of the data presented in the following chapters.

4.1.1 The Ion Guide technique

The IGISOL separator at JYFL in Jyväskylä (Äystö, 2001) is optimal for an experimental probing of the ^{12}C continuum with beta decays of ^{12}N and ^{12}B. The reason for this is that IGISOL is the only ISOL facility (figure 4.1.1) where beams of both isotopes have yet been produced. IGISOL is an abbreviation for *Ion Guide Isotope Separator On-Line* and builds on an ion guide, where the isotopes are produced as ions and guided directly to the experimental setup, avoiding the typical ion source design where boron and nitrogen are easily trapped. IGISOL was therefore the first ISOL facility to produce a ^{12}N beam, and for ^{12}B it is at other ISOL facilities (see e.g.: Diget et al., 2005) necessary to produce ^{12}B via the beta decay of ^{12}Be.

The isotopes of interest are produced in a thin foil upon which a beam of a light stable nucleus impinges. The production can therefore be very selective, when target, beam and beam energy is chosen properly. The used reactions[2] are listed in table 4.1.1.

The primary beam is therefore accelerated in the k130 cyclotron at JYFL to the appropriate energy and shot on the thin target, as shown in figure 4.1.2. With the thin target, the reaction recoil is enough to make the produced nuclei leave the target as ions after which they are stopped in a helium buffer gas. When stopped they are guided to the acceleration chamber by subsequent acceleration voltages, where the beam is accelerated to a total of 25 keV. After this the accelerated beam is led through a mass separator to the experimental setup as shown in figure 4.1.1.

4.2 Detection: Coincidence measurements

The primary detector system (Äystö et al., 2002) consists of three detectors surrounding a ^{12}C foil of thickness 33 µg/cm^2 and a diameter of 2 cm (figure 4.2.1) in which the beam is stopped. When the stopped nucleus decays it will break up into three α particles, if the ^{12}C nucleus is populated above the threshold. In

[2]Besides the two isotopes decaying to ^{12}C, ^{20}Na nuclei were produced using the $^{24}Mg(p,\alpha n)^{20}Na$, with a 40 MeV proton beam. Since beta decay of ^{20}Na in some cases result in beta delayed alpha particles, this decay is used for testing calibration and geometry of the setup as described in section 5.1.1.

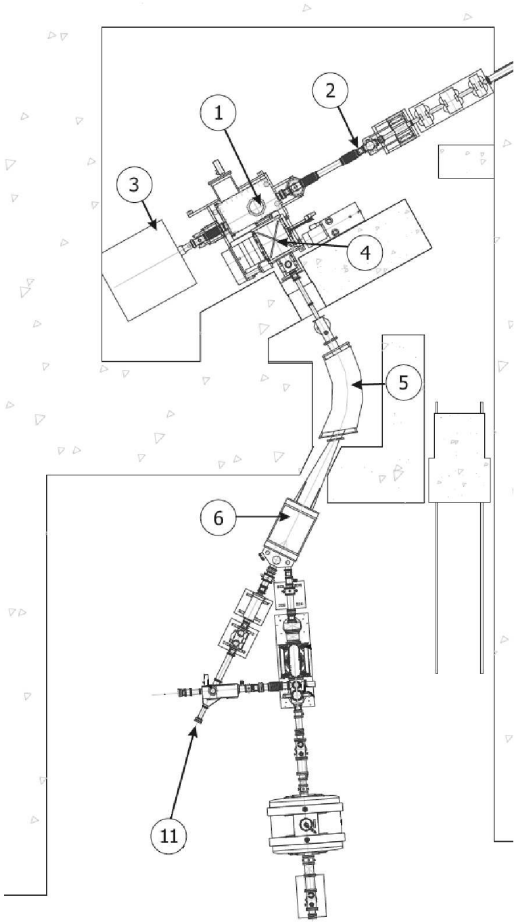

Figure 4.1.1: The Igisol separator (figure adapted from: Penttilä, 1998). Of importance in this context is: 1) Ion guide; 2) Cyclotron beam line; 3) Beam dump; 4) Acceleration chamber; 5) Dipole magnet; 6) Switch yard; and 11) Experimental setup.

this case we make use of the fact that the three detectors are segmented and as well have a good energy resolution. This allows us to detect more than one alpha particle from a single breakup. The three detectors are furthermore placed close enough to the foil to allow detection of all three alpha particles from the beta delayed triple alpha breakups as indicated in figure 4.2.2. The efficiency of the triple coincidence detection is around 2% as described in the following chapters.

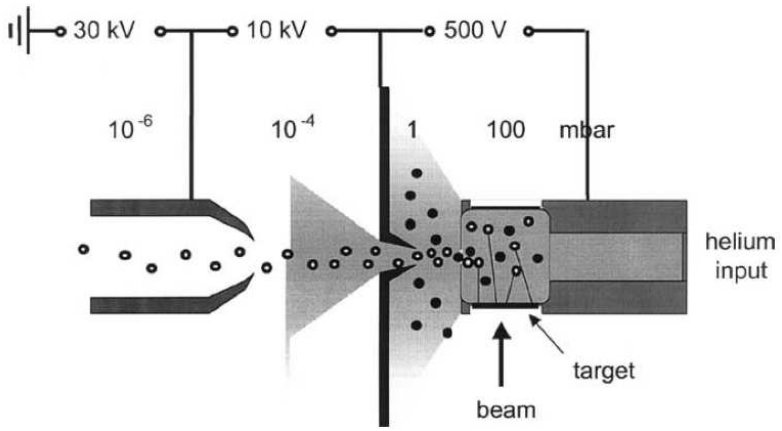

Figure 4.1.2: IGISOL ion guide layout (figure from: Äystö, 2001). Note that in our experiment the total acceleration energy was only 25 keV.

4.2.1 Detectors

The three detectors positioned roughly 3 cm from the decay point are all *double sided silicon strip detectors* (DSSSDs) constructed of a 50 mm×50 mm silicon wafer of a thickness around 60 µm. All three have a thin implantation layer on each side, doped to make front and back p-type and n-type respectively. Here "front" refers to the side of the detector facing the foil. The implants are separated in 16 strips on both sides of width 3.0 mm, where the front strips are vertical and the back strips are horizontal. When a charged particle hits the detector electron-hole pairs are created and the holes are attracted to the front side by a negative voltage giving rise to a signal in the front strip that was hit, likewise for the back strips in which the electrons give a signal. A thin contact grid of aluminum has been deposited on each strip, and the amplitudes of the resulting signals are transformed to energy signals and stored along with parameters identifying in which strip the hit occurred. Typically several strips are hit by different particles and the information describing those hits are stored as a single event in the data structure. We can afterwards in the offline analysis identify the position and energy of the measured alpha particles in the event as described in chapter 5. For the two detectors facing each other, the contact grid covers only 2% of the detector, making the detector dead layer dominated by the doped inactive region of the silicon wafer. This yields an effective dead layer equivalent to 100 nm of silicon. A detailed test of these DSSSDs have been carried out recently by Tengblad et al. (2004) and is published along with a description of the DSSSDs. The third detector is somewhat older and of a different design where the contact grid covers the active regions completely yielding a total dead layer of 630 nm. The response of this detector has been analyzed in detail by

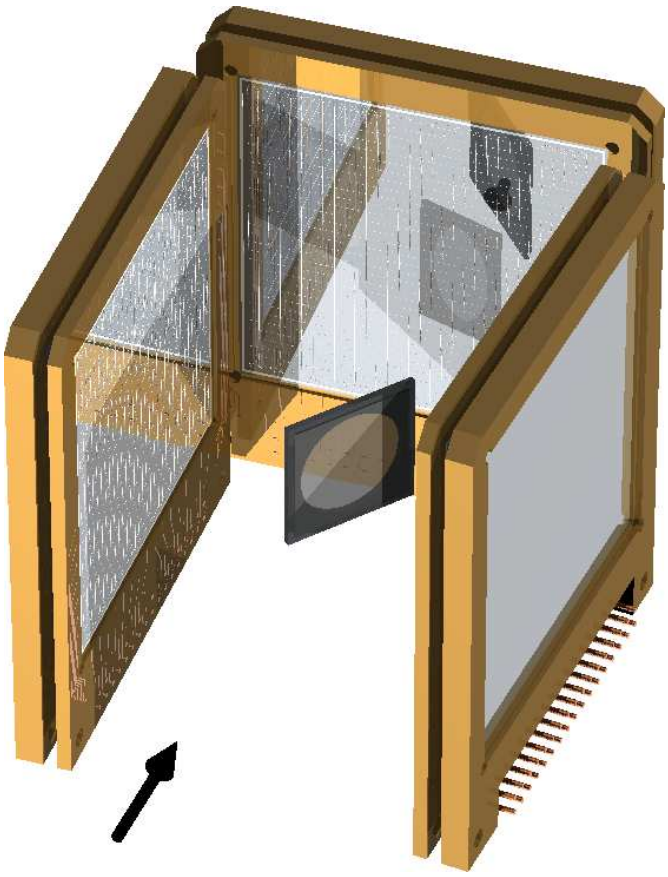

Figure 4.2.1: Detector setup, three thin DSSSDs backed by thicker beta detectors surrounding a thin carbon foil. The arrow illustrates the incoming beam.

Thaysen (1999).

4.2.2 Three particle phase space coverage

As shown in figure 4.2.2 there are basically two ways of making a setup of three such detectors. One where the three detectors are positioned like three sides of a horseshoe and one where the two are positioned opposite to the third as indicated in the figure. Before deciding which of the two setups to use it is good to get an idea about the advantages and drawbacks of the two.

Such a comparison can be made using a Monte-Carlo simulation (Eidelman et al., 2004), where three particle phase space is sampled allowing us to test the probability of detecting all three alpha particles with the two setups. The result of

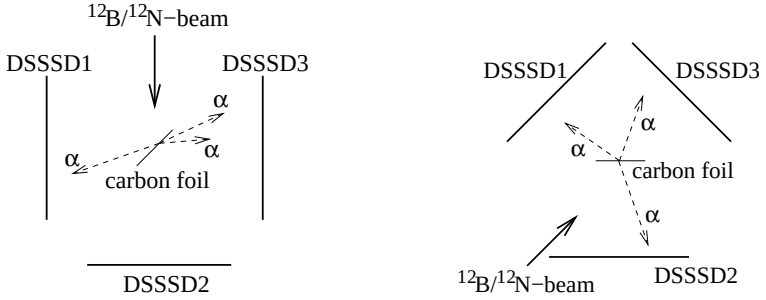

Figure 4.2.2: Two possible setups for three DSSSDs. Left: "horseshoe" setup, right: "house" setup (top view).

this sampling is a scatter plot over three particle phase space for the phase space distributed events as well as for the triple coincidence detections corresponding to the two setups. For simplicity the detectors are assumed to have a 100% efficiency and are placed 3.2 cm from the foil for the lower of the three (figure 4.2.2) and at a distance of 2.8 cm for the two remaining, making the solid angle coverage identical for the two compared setups. No effects of low energy cutoffs and identification of the alpha particle positions in the detectors are included. Only the effect of the detector geometry.

To describe this detection efficiency over the entire three particle phase space we need a convenient set of coordinates to plot. For this Dalitz (1953) has used a plot of the two coordinates[3]: $x = \sqrt{3}\,(E_1 - E_3)\,/E$ and $y = (2E_2 - E_1 - E_3)\,/E$ which has very nice properties, especially for three particle decays where the three particles have the same mass. The breakup studied by Dalitz bears strong similarities with the breakup presented here since what he studied was the decay of a K meson into three pions whereas in this case we have an excited ^{12}C state decaying into a three alpha final state. In both cases a three particle breakup and in both cases the three particles have identical mass. Though his description is as well useful in other three particle breakups, this is why it is of particular value in this case.

The so-called Dalitz plot seen in figure 4.2.3 have three very useful properties. Firstly when y versus x is plotted, all possible three particle breakups will fall in the equilateral triangle drawn on the central Dalitz plot. This property is determined by energy conservation alone, because with his definition of x and y, the distances to the three sides are exactly the three individual energies scaled by the total energy as indicated. This allows us to directly identify how the energy is shared between the three particles from just looking at the point in the Dalitz plot corresponding to a given breakup the center will therefore correspond to an equal

[3]Note that Dalitz uses the convention $E_1 > E_3 > E_2$ in his plotting. For convenience $E_1 > E_2 > E_3$ has been used here, resulting in an interchange of E_2 and E_3 compared to the definitions of Dalitz.

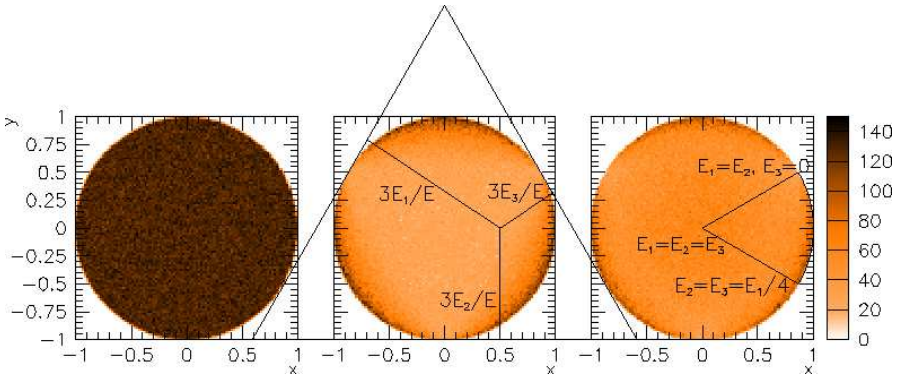

Figure 4.2.3: Dalitz plot for pure three particle phase space and triple coincidences detected by the horseshoe and house setup respectively. The intensity scale on the left plot is arbitrary, whereas for the two remaining it follows the indicated scale.

sharing of the energy whereas the outer regions correspond to one or two of the particles taking the most of the energy as illustrated in the plot to the right. Note that this is a general characteristic of the Dalitz plot and thus applies to all three particle decays no matter how the masses of the three particles are relative to each other. The second property derives from momentum conservation which requires for a breakup to three identical mass particles that all breakups must fall within the circle which is clearly visible in the plots. Furthermore with this symmetry, it is clear that the six slices of which one is shown in the rightmost Dalitz plot are actually identical and correspond to just a different numbering of the three particles. The third property is as well valid for three identical masses, and is equally important. As Dalitz states, the distribution of the decays over the circle is uniform if it is determined by a pure three particle phase space distribution. This can as well be seen in the left plot where this phase space distribution is plotted. This means that any deviation from a uniform distribution in the two plots to the right are because of differences in detection efficiency.

As seen in the two efficiency plots, the overall triple coincidence detection efficiency of the two setups are quite similar. There are however differences in the efficiency when comparing individual regions of phase space. For the region with equal sharing of the energy the house setup is the best whereas for an uneven sharing the horseshoe is preferable. This in itself does not give any preference to any of the two, but since the house setup has a more uniform efficiency over three particle phase space the simulated efficiencies can be said to favor the house setup. This is because one of the channels that we want to investigate is the breakup through higher energies of ^{8}Be and since we cannot a priori say how such breakup events are distributed over phase space, we need a significant efficiency at all possible energy sharings. In favor of the horseshoe setup is the

fact that it is more efficient in the region of phase space where one alpha takes as much of the energy as allowed by momentum conservation (the ^{8}Be ground state channel). This channel will be important to determine the degree of isospin symmetry between the decays of ^{12}B and ^{12}N. Another more practical concern is that it is easier to mount the horseshoe setup along with the other detectors to be mounted (see the following).

The conclusion is that the reduction in detection efficiency in the central region of the Dalitz plot of about a factor of two for the horseshoe setup is acceptable compared to the other advantages of the setup, and the horseshoe setup is therefore chosen as shown in figure 4.2.1.

4.2.3 Additionals

Backing the DSSSDs as indicated in figure 4.2.1, three silicon detectors are placed. These have no segmentation and are of a sufficient thickness to allow detection of the beta particles that go straight through the DSSSDs. Furthermore a germanium gamma detector is placed outside the vacuum chamber as close to the decay point as possible. The combination of these two makes it possible to not only study the beta delayed alpha emission, but as well detect the beta delayed gammas from the beta decays to the bound 4.44 MeV 2^{+} state in ^{12}C (see figures 2.1.2 and 2.1.4). In section 8.4 this will be used to identify the absolute branching ratios from the known branching ratios to the 4.44 MeV state.

In addition to these detectors, a segmented silicon hemisphere is included in the setup (Bergmann et al., 2003a).[4] The hemisphere has a radius of about 20 cm, and segments of 2 cm×2 cm and a thickness of 1 mm. With the distances between decay point and detectors applied in this experiment, the hemisphere has an angular resolution similar to that of the DSSSD pixels. During the data analysis however it was concluded that the hemisphere has too significant beta response to allow for a sufficient discrimination between alpha and beta particles. Though it could be done, it was judged that the gained statistics was insufficient to justify the systematic uncertainties introduced by the ambiguity in particle identification.

To determine which data events to store on disk, different trigger settings are applied during the experiment. In the greater part of the beam time the front strip signals are triggering the data acquisition system, whereas from a small part of the experiment, the backing beta detectors are as well used. The former is the data described in the following chapter and analyzed in chapters 6 to 8 while the latter is only used for the beta-gamma coincidence detection yielding the absolute normalization of branching ratios as will be mentioned in section 8.4. For all events, the energy signals are stored as well as are the timing signals from the DSSSD front strips.

[4] Used as well in an experiment at IGISOL immediately after our data taking (Kankainen et al., 2006).

CHAPTER 5

Data analysis

The data analysis contains two conceptionally different parts. Firstly the handling of the raw data set in which important physical distributions are extracted (this chapter), and secondly the interpretation of these distributions in terms of states in ^{12}C and their breakup to the triple alpha continuum (chapter 6–8).

The first part given in the following is rather technical and includes calibration of the detectors, single particle identification, triple coincidence detection and a thorough analysis of the applied cutoffs.

5.1 Calibration

The response of each of the individual 3x2x16 strips in the setup must be calibrated, taking into account the dead layer of the detector. The calibration and test of the calibration will be described in the following.

5.1.1 Online and offline sources

Three different alpha sources are used in the calibration, to ensure that all systematics are under control. A ^{148}Gd source and a ^{241}Am source are used for the actual calibration, while a ^{20}Na source is used for testing the calibration as well as the setup geometry and the dead layer corrections derived from this geometry.

These three sources cover the range of alpha energies from about 2 MeV to 5.5 MeV. The decay of ^{148}Gd yields a single alpha, whereas alphas with many different energies are emitted in the ^{241}Am decays (Firestone & Shirley, 1996).

Decaying nucleus	^{148}Gd	^{241}Am	^{241}Am
α-energy (MeV)	3.182787(24)	5.44290(13)	5.48560(12)
Absolute branching	100%	12.8(2)%	84.2(8)%

Table 5.1.1: Calibration α energies: ^{148}Gd and ^{241}Am.

α-energy (MeV)	2.1504(19)	2.4796(21)	3.799(3)	4.4322(29)
Relative branching	100%	3.65(43)%	1.510(27)%	17.31(9)%
α-energy (MeV)	4.673(3)	4.885(3)	5.249(4)	5.698(6)
Relative branching	0.553(15)%	1.09(3)%	0.165(11)%	0.010(2)%

Table 5.1.2: Calibration test α energies: ^{20}Na.

Of these only the dominating one is used in the calibration. However when determining the energy channel corresponding to the dominant peak, knowledge of the lower peak is included. In the ^{148}Gd data as well as in the ^{241}Am data, the central energy channel of the peak is identified in a Gaussian fit to the individual strip spectra. For the ^{20}Na calibration test on the other hand eight different alpha groups are used (Clifford et al., 1989). The ^{148}Gd and ^{241}Am sources are standard offline sources placed in the chamber in front of the three detectors one by one, while ^{20}Na with a half life of 446 ms must be produced online as described in section 4.1.1. When produced the ^{20}Na beam is implanted in the same foil as the one afterwards used for stopping the ^{12}B and ^{12}N beams. In this way we can test that we understand the energy loss in foil and detector dead layers, not only for the sodium decay data but for the boron and nitrogen data as well. This emphasizes the strength of using an online calibration source, possibly in addition to offline sources. Offline calibration was done at the beginning and end of the experiment, while the online calibration was done between the boron and nitrogen runs and repeated after the nitrogen run.

5.1.2 Source positions

Since the calibrations of all strips are very similar, the detector pixel being hit by the alpha particle can easily be identified. At least for the calibration data, where the typical event has one alpha hitting the detector in question besides low energy noise in some of the strips not being hit by the alpha particle. This can be seen in figure 5.1.1, where back strip energy channel is plotted against front strip energy channel for the DSSSD3 ^{241}Am calibration data. To exclude low energy noise a cut is placed around the diagonal, accepting only front-back pairs that differ by less than 500 channels and have both front and back energy channels above 700. For these identified hits, the pixel distribution is shown in figure 5.1.2. This distribution can be described by assuming a isotropic emittance from a point source somewhere in front of the detector taking into account the

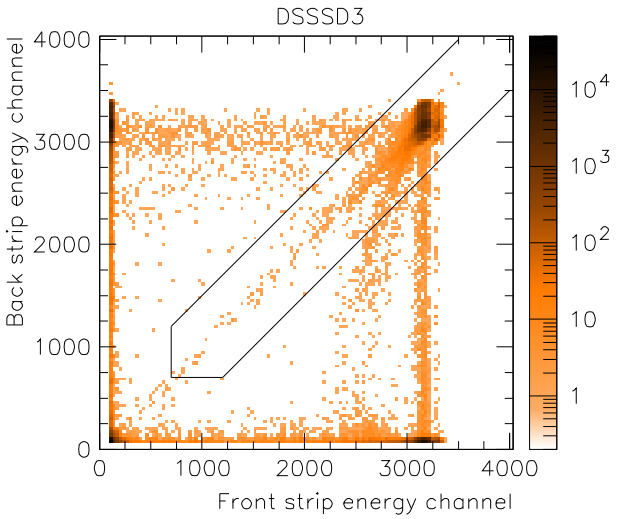

Figure 5.1.1: DSSSD3 ^{241}Am data, back strip energy channel vs. front strip energy channel. Cutoff for front-back identification is shown.

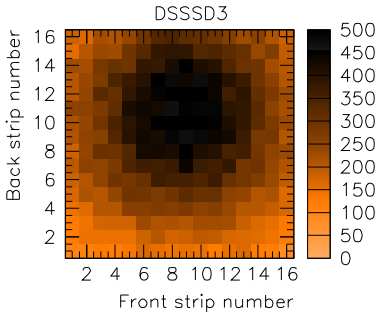

Figure 5.1.2: DSSSD3 ^{241}Am data grid: Number of events per pixel.

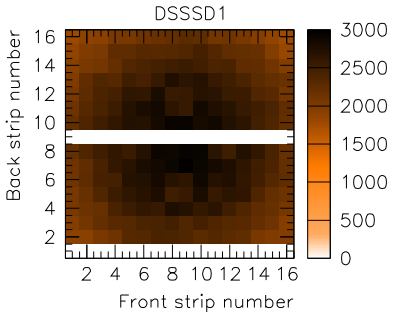

Figure 5.1.3: DSSSD1 ^{148}Gd data grid: Number of events per pixel.

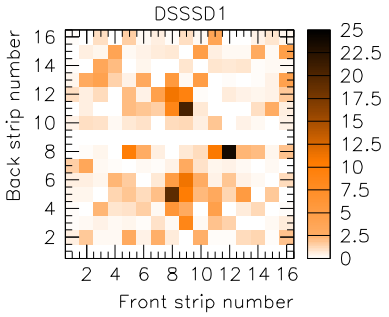

Figure 5.1.4: DSSSD1 ^{148}Gd fit to data grid: individual pixel contribution to χ^2_λ.

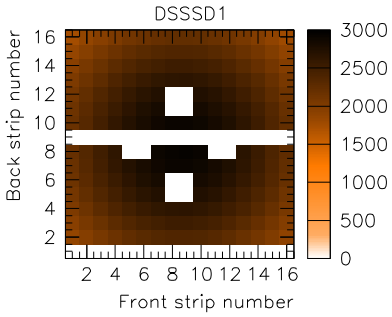

Figure 5.1.5: DSSSD1 ^{148}Gd fit to data grid: fit excluding 4x4 pixels.

solid angle the individual pixel covers as seen from the point source. This solid angle is proportional to z/r^3 where z is the distance from the detector plane to the source and r is the distance from the pixel to the point source under the approximation that pixel dimensions are small compared to z. By fitting such a distribution to the measured distribution, the position of the point source is identified.

For DSSSD1 and DSSSD2 a few dead strips have been excluded from the analysis. Apart from this, the analysis of the source position is analogous to that of the DSSSD3 data. However one additional complication arises for DSSSD1. As can be seen from figure 5.1.3, there are four 2x2 squares where the detected intensity seems to be lower than what would be expected from a smooth distribution. (Note that only 12 of the 16 pixels are actually seen, since the last 4 pixels lie in a malfunctioning strip.) And indeed if we fit the solid angle distribution to this data set and investigate the contributions to the log-likelihood χ^2 (χ^2_λ), we see that these four regions have a significant contribution to the total χ^2_λ (figure 5.1.4). This effect has been studied by Thaysen (1999) and is caused by the design of this particular DSSSD for which the inter strip separation is larger in these four regions, resulting in these 16 pixels being slightly smaller. This effect has been avoided in the design of the two new DSSSDs. Because of this reduction the 12 pixels are excluded in the source coordinate fits as can be seen in the fitted distribution shown in figure 5.1.5. With this fit in hand we can estimate the reduction in active detector area for these pixels compared to the remaining pixels. For the ^{241}Am data the total number of counts for the 12 pixels is 6021, whereas the number of counts expected from the fitted distribution is 6519, corresponding to an active area of only 92.4(17)% of the standard pixel size. (The noted uncertainty neglects any uncertainties in the fitted distribution,

Detector	x_i (mm)	y_i (mm)	z_i (mm)
DSSSD1	1.38(15)	7.72(20)	34.84(37)
DSSSD2	-3.09(10)	7.38(11)	28.79(19)
DSSSD3	2.46(7)	8.06(8)	25.28(13)

Table 5.1.3: Foil position relative to detector plane centers.

which is reasonable since the majority of the data lie within the fitted 212 pixels.) The ^{148}Gd data has better statistics and is consistent with the ^{241}Am data. By combining the two the best estimate of the active area is determined to be 92.6(7)% of the standard pixel size.

In exactly the same way the source position in the three detector coordinate systems can be found for the ^{20}Na data, to illustrate the detector positions relative to the foil the coordinates are given in table 5.1.3. Here the x_i and y_i coordinates are within the plane of the respective detector both relative to the center of detector i, x_i being the horizontal coordinate and y_i the vertical. The z_i coordinate is perpendicular to the detector plane and is thus the distance from the beam spot to the detector. The average precision of these is about 0.15 mm, significantly better than what could be achieved when measuring by hand.

5.1.3 Energy loss and dead layers

The energy deposited in the dead layer is about 25 keV for the new detectors (DSSSD2 & DSSSD3) and 200 keV for the old detector (DSSSD1). This however depends on energy as well as the impact angle of the alpha on the detector. In addition to this, a similar energy loss is experienced when the decaying isotope is implanted in the foil, yielding a foil energy loss of about 25 keV, with similar variations as those of the dead layer corrections. To take these variations properly into account, two different strategies are applied, one for the offline sources and one for the online source.

To calibrate using the ^{148}Gd and ^{241}Am sources, we start by identifying an effective position of the two peaks for each strip. Since we can assume that no energy is lost in the sources, the first step in doing this is to calculate the dead layer correction for each of the 16 pixels in the strip in question. From the source position derived in the preceding, the impact angle of the alpha particle on the detector is found, yielding the effective dead layer of the pixel as seen from the source. From a Srim2003 (Ziegler et al., 2003) calculation, the stopping of the alpha particle in the dead layer is found, yielding an effective peak position for this pixel. By averaging over all 16 pixels, weighted by their solid angle coverage as seen from the source, the effective peak position for the strip is found. Since we now know the typical energy deposited in the active region of the strip, the strip can be calibrated.

This calibration, is now used in the analysis of the ^{20}Na data, to transform the raw energy channel spectrum to a spectrum of the energy deposited in the

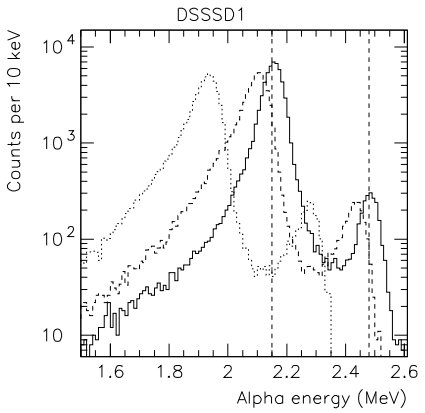

Figure 5.1.6: ^{20}Na alpha energy for DSSSD1 and energy before foil energy loss correction and dead layer correction. Tabulated energies shown as vertical lines.

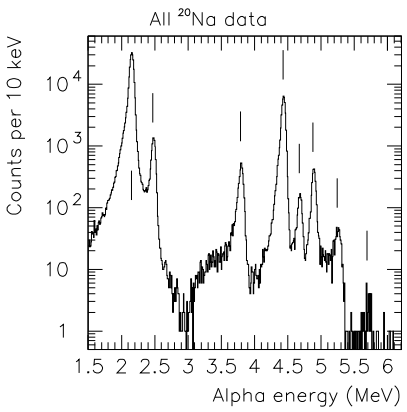

Figure 5.1.7: Total ^{20}Na foil and dead layer energy loss corrected spectrum. Peaks used in the calibration test are marked.

active region of the strip. By identifying which pixel was hit in the individual event, the effective dead layer is known allowing dead layer correction on an event-by-event basis. Similarly, from the impact point of the individual alpha particle on the detector the angle of the emitted alpha with respect to the foil can be deduced. From this and the energy of the alpha particle, the foil energy loss can be deduced. It is important to consider the energy dependence of the energy loss, so the alpha energy (E_α) after passing through a length x of material is:

$$E_\alpha(x) = E_\alpha(0) - \int_0^x \left|\frac{\Delta E}{\Delta x}\right|_{E_\alpha(x')} dx'$$

where $\frac{\Delta E}{\Delta x}$ is the energy loss per unit length for the material in question. Getting this right is crucial for low energy particles especially, since the energy loss can be a significant part of the total energy. This strategy is therefore applied to the triple alpha breakup data discussed in the following chapters.

This correction is illustrated in figure 5.1.6, where the measured 2 MeV ^{20}Na alpha energy peak is compared to the energy loss corrected energies and the tabulated energy. Since the effective thickness of both foil and dead layer is different for the individual pixels in one strip, the correction for this on an event-by-event basis, not only removes the energy loss bias in the raw data, but increases the resolution as well, as can be seen by comparing the widths of the individual peaks in the figure.

5.1.4 Results

The total energy loss corrected data set for ^{20}Na is shown in figure 5.1.7. All energies are extracted from front strip energies and agree with the measurements of Clifford et al. (1989) within 10–20 keV. The peaks have been fitted to Gaussian distributions yielding a root mean square (RMS) width σ of 30 keV corresponding to a single alpha full width at half maximum (FWHM) resolution of 70 keV. No significant energy dependence in the resolution is seen.

In addition to the precision and resolution, directly used in the following data analysis, a few important aspects of the ^{20}Na data should be noted. Firstly, the measured relative branching ratios of the eight alpha groups are consistent with those listed in section 5.1.1, but since we have less statistics this data set gives no significant improvement of the relative branchings. One thing however can be concluded: As expected our single alpha energy detection efficiency is independent of energy in the measured 2–6 MeV energy range. With regards to the individual alpha groups, special attention should be drawn to the 2.5 MeV group, since it was measured by Clifford et al., but for some reason was not included in the eighth edition of the Table of Isotopes (Firestone & Shirley, 1996). With this confirmation it is unavoidable in future nuclear tables. A third characteristic of the spectrum is the broad structure just above 3 MeV. This alpha group has a very sharp low energy cutoff for a state as broad as the one giving rise to this alpha group. As will be shown in the coming chapters such an abrupt cutoff often indicates interference between two broad neighboring states of identical spin and parity. Thus for a proper description of the details of the ^{20}Na spectrum, inclusion of interference effects will most likely be needed.

5.2 Cutoffs and single particle identification

In this experiment we measure triple alpha coincidences in a 96 channel setup only covering 4π solid angle partly. This makes detection efficiencies a bit difficult to handle, and special care should be taken, since it will depend on the relative directions of the three alpha particles. To describe these dependencies properly, Monte-Carlo simulations will be made in chapter 6. For such a simulation to be correct however, it is necessary to have all single particle detection cutoffs and cutoffs introduced in the data analysis under control. In the following, the different cutoffs will be determined or defined.

5.2.1 Geometric detector coverage

With the setup described in section 4.2 and the detector-foil distances in table 5.1.3 the three detectors each cover roughly 10% of 4π. From this 9 of the 96 strips have been excluded, either because they were dead (section 5.1.2), because they were partly shaded by the foil holder (figure 4.2.1) or because of bad resolution or calibration, such as the strips identified in section 5.2.4 below.

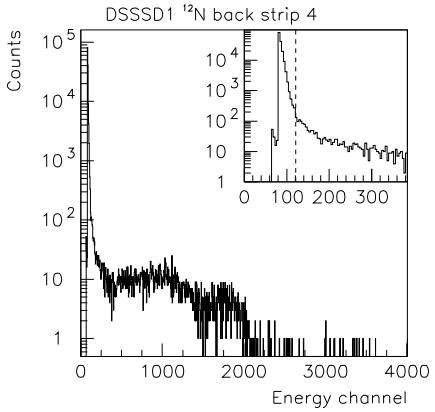

Figure 5.2.1: ^{12}N data, uncalibrated energy channel for a single strip. Inset shows zoom at low energy and the applied low energy cutoff for this particular strip.

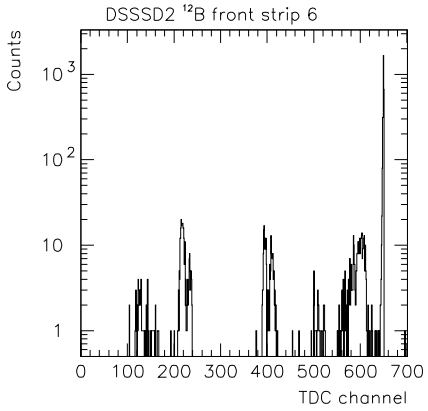

Figure 5.2.2: Time relative to trigger for one strip. The events around channel 650 are the events triggered by this strip.

In addition to this, the reduction of the active detector region (section 5.1.2) for the 16 pixels in DSSSD1 must be taken into account in the coming simulations.

5.2.2 Single strip low-energy cutoff

A low energy background is unavoidable, it arises from a combination of beta response and electronic noise in the setup. For this analysis there is no need to distinguish between the two, and it will be referred to simply as the low energy noise. For each strip a proper cutoff is chosen to cut away the majority of the noise. Such a cutoff is shown in figure 5.2.1 for a single strip. Choosing a reasonable cutoff value is always a question of weighing the complications arising from letting noise signals into the analysis against the drawback of cutting away real data. As will be seen in the following, other methods can be used here to distinguish between noise signals and physical data, so the implications from noise can be dealt with, and the cutoff is chosen to accept some noise. As seen in the figure, a typical cutoff is the channel with about ten times the number of counts around channel 250.

5.2.3 Trigger levels from TDC gated events

Where the low energy cutoff defined above sets the lowest possible energy for a detected particle, the trigger level basically sets the lowest possible energy for

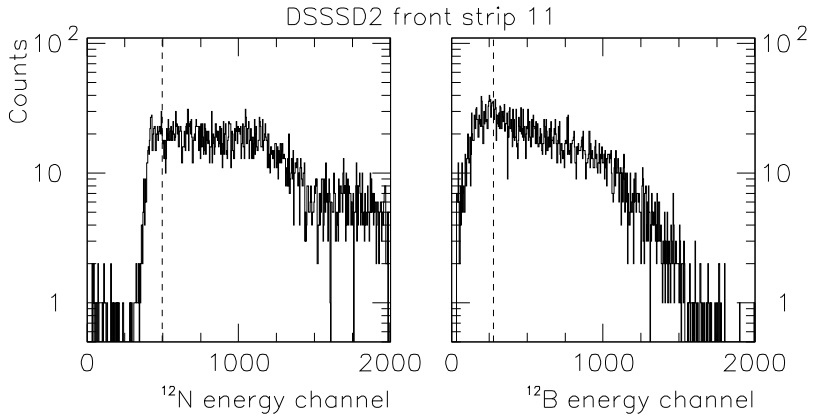

Figure 5.2.3: Energy in a single strip from events triggered by the strip. ^{12}N and ^{12}B data are compared for this strip.

the highest energy particle in the event. That is: both will influence the low energy cutoff for the triple events, making it essential to have a well defined and identical trigger level for data analysis and simulation.

To make sure the trigger thresholds are under control, the TDC time spectrum is plotted. This spectrum shows the time of a given strip signal relative to the trigger time of the event in question. For all events where the strip we are investigating is the one triggering the event, the TDC signal will end up in a very narrow peak. This is seen in figure 5.2.2, where the trigger peak is easily recognized close to channel 650.

When it is known, that a given strip was the one triggering the event, the energy of that strip is interesting from a triggering point of view, since that energy must be above the trigger threshold. Such a single strip trigger energy spectrum is shown in figure 5.2.3, for a strip in both ^{12}N and ^{12}B data. As illustrated, a rather conservative value for the trigger threshold is applied.

TDC signals and triggers are included in the data acquisition for front strips only, and not all front strips have as clean TDC spectra as the one showed in the figure. The trigger peak however can be recognized for all the front strips included in the analysis, and an upper limit for the trigger threshold is found for all strips. Though not all strips exhibit as pronounced a difference when comparing boron and nitrogen as the strip shown here, the effect is general and comes from the fact that electronic noise was stronger during the days of nitrogen data taking compared to the boron data taking. This noise difference results in a lower triple alpha energy cutoff for the boron data as will be seen in the following.

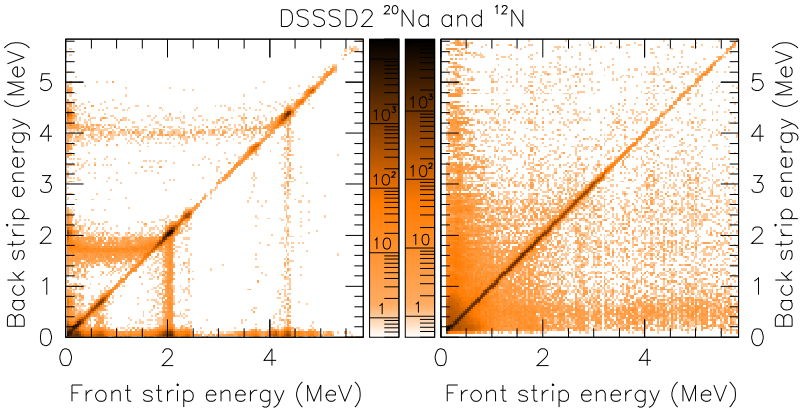

Figure 5.2.4: DSSSD2 calibrated front-back identification plot. ^{20}Na data to the left, ^{12}N data to the right.

5.2.4 Front-back identification of alpha particles

With the calibration in place, the front-back identification of the activated pixel can be performed with a stronger requirement on the difference between front and back energy. Such an identification plot is shown in figure 5.2.4. The final identification cut applied accepted only front-back pairs with an energy difference less than 80 keV. As before, such an identified pair corresponds to a particle depositing its energy in a single pixel. In the following this will be denoted a *hit*.

As noted in section 5.1.4 the single alpha energies are taken from the front strip energies. Thus to test the back strip energies, we compare front-back energies on a strip by strip basis. Such a comparison is shown in figure 5.2.5 for a single back strip. This ^{20}Na plot includes only the dominating 2.15 MeV peak and is produced with a slightly larger acceptance in front-back energy difference. The plot clearly shows a roughly 30 keV offset in the back strip in DSSSD1. When investigating the corresponding plots for all DSSSD1 back strips for different parts of data set, it is seen that the effect is present for all strips and for all parts of the data. Consequently the DSSSD1 back strip data is shifted up by 30 keV.

No overall offset is seen for the back strip in DSSSD2 and DSSSD3, but for two of the front strips the front and back energies do not coincide. This is as well seen when investigating the other back strips, and since the effect turns out to be less pronounced for the 4 MeV peak it indicates a nonlinear energy response for the two front strips, consequently the two strips are discarded.

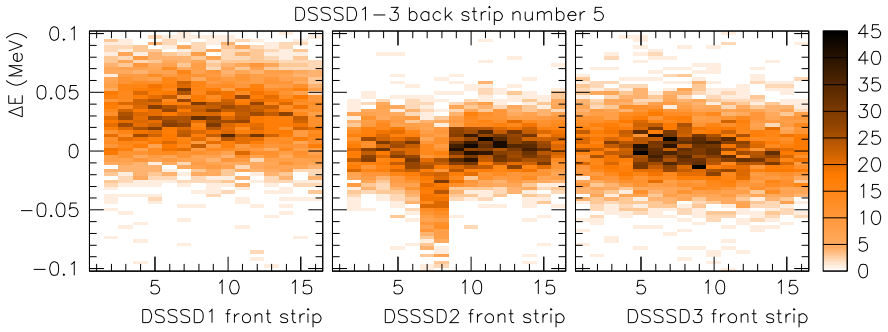

Figure 5.2.5: ^{20}Na data, 2.15 MeV peak. For a single back strip in the three detectors, the energy difference ($\Delta E = E_{front} - E_{back}$) between measured front and back energies is plotted for individual front strips.

5.3 Triple alpha detection

With single alpha detection under control, the next stop in the analysis process is identifying triple coincidences. If a given event has less than three hits, it is of course irrelevant with regards to triple coincidences, but if it has three or more hits, several different combinations may form possible triples. The following deals with this ambiguity, using the sum momentum for the three alpha particles. This sum should be zero for real triple alpha events when recoil from the beta decay is neglected. As will be shown in the following (section 5.3.2) this recoil is indeed small.

5.3.1 Momentum and beam spot positions

However before doing this, we will take a brief look at the three projections of the sum momentum p_x, p_y and p_z. In section 5.1.2 we identified the beam spot position relative to the detectors from the ^{20}Na data. With this position relative to the pixels hit by the individual alpha particles and knowledge of the amount of energy deposited in the pixel we can calculate the momentum of the individual particles. Given these three momenta we can calculate p_x, p_y and p_z for their sum momentum, with x and y being horizontal and vertical in the foil plane and z being perpendicular to the foil plane. The setup illustration in figure 4.2.1 gives an overview of how this foil plane is positioned relative to the three detectors. The momentum projections with these assumptions are shown in the upper frames of figure 5.3.1

The beam spot position discussed in section 5.1.2 however was for the ^{20}Na data and there is no reason to assume that the position should be exactly the

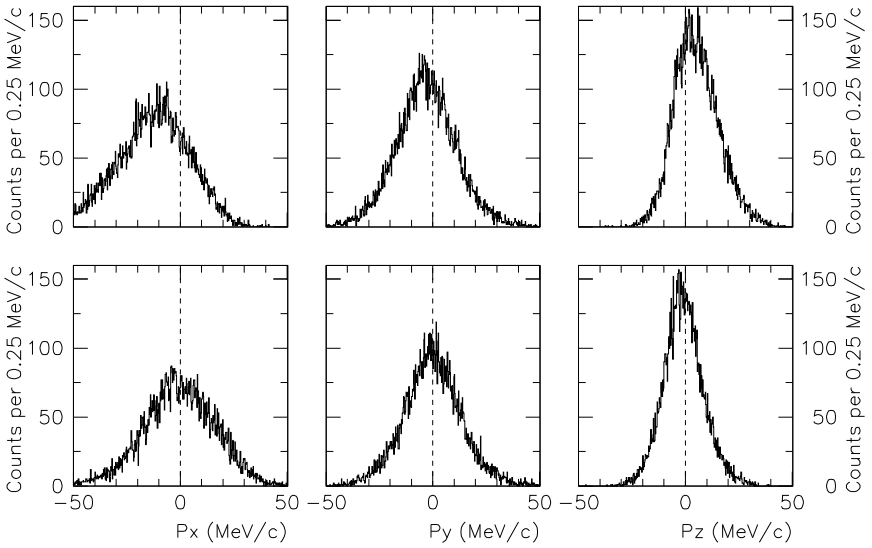

Figure 5.3.1: Sum momentum projections p_x, p_y and p_z for ^{12}N data. Upper row: Momentum reconstruction assuming same beam-spot position as for ^{20}Na data. Lower row: Beam spot moved within the foil plane.

same for the ^{12}N data or the ^{12}B data for that matter. Since the beta decaying nucleus and thereby the intermediate ^{12}C is at rest in the lab frame, at least on average, all three momentum projections must be zero on average. This is certainly not the case if we assume the beam spot positions to be identical, as can be seen in the upper frames of figure 5.3.1. However if we allow a displacement of the beam spot for the ^{12}N data relative to the position for the ^{20}Na data and thus assume the beam spot to be shifted by 2 mm in the right direction within the foil plane all three projections are zero on average as seen in the lower three frames of figure 5.3.1. This demonstrates that the momentum projections are very sensitive to the detailed assumptions on the geometry.

5.3.2 Total energy and momentum

Now returning to the total momentum: Since we will use the total momentum of the three alpha particles to discriminate between true triple alpha events and triples where at least one of the three is a background hit, we must be sure that the intermediate ^{12}C nucleus is essentially at rest before the breakup. "Essentially at rest" is a very accurate description as will be seen in the following where we will investigate the small recoil from the emitted beta particle and neutrino in

the decay to the intermediate ^{12}C state.

The recoil momentum distribution for a given Q value is found from the beta energy distribution and the distribution of the relative angle between the two leptons emitted in the decay. These two distributions should be integrated over all energies and angles contributing to a given recoil momentum. The easiest way to perform this integration is to sample the energies and angles according to their distributions. To do this, the *cumulative distribution function* (cdf) for the energy distribution must be found, and for any such energy the angular cdf is as well needed.

For a given beta decay Q value, the beta energy distribution can be found from the phase space of beta and neutrino. This distribution may be modified by the Coulomb attraction (repulsion) between the nucleus and electron (positron). For high Q values and low nuclear charges however the Coulomb interaction can be neglected. When this is done, the *probability density function* (pdf) in kinetic energy is proportional to:

$$W(T_\beta)dT_\beta \propto (T_\beta^2 + 2T_\beta mc^2)^{1/2}(Q - T_\beta)^2(T_\beta + mc^2)dT_\beta \tag{5.3.1}$$

where m is the electron mass, T_β is the kinetic energy of the beta particle which makes $Q - T_\beta$ the energy of the (anti)neutrino (Krane, 1988). The cdf is then found by normalizing and integrating the pdf.

For any such energy T_β, the angular correlation between the two leptons is given by Hamilton (1947):

$$W_c(\Omega_{\beta\nu})d\Omega_{\beta\nu} \propto \left(1 + a\frac{p_\beta c}{E_\beta}\cos(\theta_{\beta\nu})\right)d\Omega_{\beta\nu} \tag{5.3.2}$$

Where $p_\beta c = \sqrt{E_\beta^2 - m^2c^4}$ is the beta particle momentum, $E_\beta = T_\beta + mc^2$ is the total energy of the beta particle and a, for a pure Gamow-Teller decay such as this, is $-\frac{1}{3}$. Integrating over the azimuthal angle $\phi_{\beta\nu}$, substituting to the dimensionless variables $x = \cos(\theta_{\beta\nu})$, $w = E_\beta/mc^2$ and normalizing yields:

$$W_c(x)dx = \frac{1}{2}\left(1 - \frac{1}{3}\frac{\sqrt{w^2-1}}{w}x\right)dx$$

From this pdf the corresponding cumulative distribution function can be calculated by integration:

$$F_c(x)dx = \frac{1}{2}(x+1) - \frac{1}{12}\frac{\sqrt{w^2-1}}{w}(x^2-1)\,dx$$

With these two cdfs in hand, a uniform random number generator such as TRandom in the Root package (Brun & Rademakers, 1997) can be used to sample the energy-angle parameter space. This is straight forward since the inverse cdf $F_c^{-1}(X)$ of a uniformly distributed stochastic variable X is distributed according

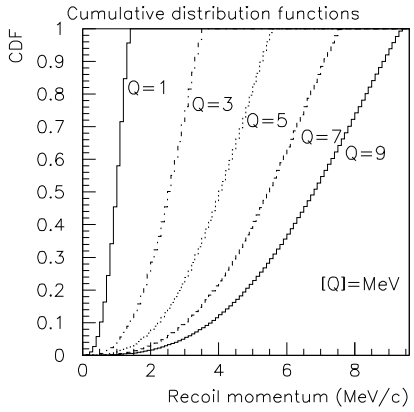

Figure 5.3.2: Sampled distribution of recoil momentum of a mass 12 nucleus in beta decays with Q values ranging from 1 MeV to 9 MeV.

to the corresponding pdf W_c. From any such pair of energy and relative angle in the sample, the recoil momentum can be calculated. The sampled recoil momentum distributions are shown in figure 5.3.2.

As will be seen in the following, a typical recoil momentum of 5 MeV/c, as is read from the plot, does not dominate the total momentum distribution. The left frame of figure 5.3.3 shows the total momentum distribution peaking around 15–25 MeV/c. The effect of daughter nucleus recoil is therefore modest, and the total momentum may be an efficient parameter in discriminating between true triple alpha events and false triples where at least one of the three was a background hit.

In an event with at least three hits, the hit with the highest energy is assumed to be a true alpha particle, and the other two particles are taken as two of the remaining hits. For all possible choices of these last two particles, the total momentum of the triple is calculated, and the different combinations are compared. Such a comparison is shown in figure 5.3.3 where total momentum versus total energy for the three particles are shown for the lowest momentum triple and the second lowest momentum triple in any event. As seen in the figure, the total momentum is a good parameter to discriminate between true and fake triple alpha events, and the cut shown in the figure is applied. This cut requires: E_{sum} >1 MeV and $p_{sum} < 15\,\mathrm{MeV/c} + \frac{160}{8} E_{sum}/\mathrm{c}$ and $p_{sum} < 80\,\mathrm{MeV/c}$. This will significantly reduce background in the final ^{12}C energy spectra.

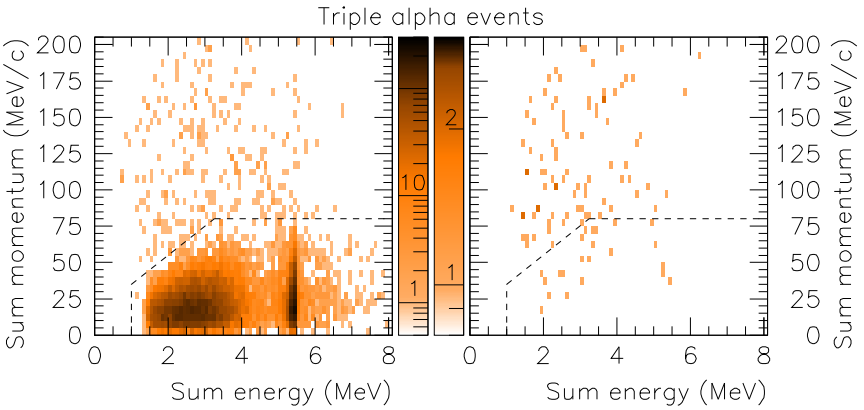

Figure 5.3.3: ^{12}N data, absolute value of sum momentum versus sum energy for three hits in one event. Left frame shows the triple with lowest sum momentum whereas the right frame shows the triple of second lowest momentum, both requiring the highest energy hit to be one of the three.

5.3.3 Reconstructed ^{8}Be energy

Since the ^{12}C states in question may break up through the sequential breakup: $^{12}\mathrm{C}^*(,\alpha)^8\mathrm{Be}(,\alpha)\alpha$ the intermediate ^{8}Be energy is an important parameter. It is therefore necessary to reconstruct this energy from the three individual alpha particle energies.

The kinematics of reactions with a three body final state have been analyzed in detail by Ohlsen (1965). With a slight modification of his arguments two different coordinate systems are very useful: One is the center of mass system of the original $^{12}\mathrm{C}^*$ nucleus, another is the center of mass system of two of the emitted alpha particles. The definition of the second coordinate system leads inevitably to the question: Which two alphas should we choose? This question will be addressed in a moment, since the answer is seen from the following analysis.

Assume a numbering $(\alpha_1, \alpha_2, \alpha_3)$ of the detected alphas and that α_1 is the one being emitted in the $^{12}\mathrm{C}^*(,\alpha)^8\mathrm{Be}$ decay. We may find the energy of the intermediate ^{8}Be relative to the triple-alpha threshold ($E_{^8\mathrm{Be}}$) from the fact that a ^{8}Be nucleus and an alpha particle will share the available kinetic energy as 1:2, that is:

$$E_{\alpha_1} = \frac{2}{3}\left(E_{^{12}\mathrm{C}^*} - E_{^8\mathrm{Be}}\right). \tag{5.3.3}$$

The two remaining alpha particles share the remaining energy, leaving on average

$$E_{\alpha} = \frac{1}{6}E_{^{12}\mathrm{C}^*} + \frac{1}{3}E_{^8\mathrm{Be}} \tag{5.3.4}$$

for each of the two. The second method uses the relative momentum of the two alpha particles from the ^{8}Be breakup. The momentum of both of the two alphas in their common center of mass is $\vec{p}_{2-3} = \frac{1}{2}(\vec{p}_2 - \vec{p}_3)$ (except from a sign difference). From this we can find the available energy in the ^{8}Be breakup as:

$$E_{^8\mathrm{Be}} = 2\frac{\vec{p}_{2-3}}{2m_\alpha}^2 . \tag{5.3.5}$$

With both methods we can reconstruct the ^{8}Be energy, since the remaining parameters are direct observables in the triple coincidence measurements. The two methods are compared in figure 5.3.4, where it is evident that although they both reconstruct the ^{8}Be energy to be the ground state energy of 0.0918 MeV (Tilley et al., 2004), their response to the uncertainties in the measured energies and positions are very different. This results in a bias for the first reconstruction method and a significantly larger spread (a factor of 3–4) compared to the second method. When comparing the upper right and lower left frames it is clearly seen, that the ^{8}Be ground state channel is a very important channel. And furthermore, since the ^{8}Be ground state energies (upper right frame) and the energies in the lower left frame are clearly separated in energy, the assumption of the two lowest energy alphas being the two ^{8}Be alphas is a safe assumption to make when identifying the events from ^{8}Be ground state break up.

The events with a reconstructed ^{8}Be energy within 60 keV from the ground state energy are considered to be events from this breakup channel (illustrated in the upper right frame), whereas events with a reconstructed ^{8}Be energy higher than 200 keV must originate from another breakup channel referred to as the ^{8}Be excited state channel.

5.4 Power and acceptance of cutoffs

In the following, the power and acceptance of the applied cutoffs will be addressed. The *power* of a cutoff being understood as a measure of how powerful the cutoff is in rejecting background events: The part of background to be let through the cutoff. The *acceptance*, on the other hand, should be understood as the cutoff's ability to accept the data of interest. This is basically a hypothesis test as described by Barlow (1989). The relevant hypothesis being for example: *This triple is a physical triple of alpha particles*. A cutoff can be seen as a test of this hypothesis. As in any other hypothesis testing, errors will inevitably occur. Both true events being rejected (type I errors) and false events being accepted (type II errors). With this parallel in mind, the *acceptance* of the cutoff is basically the significance of the test, namely its ability to avoid type I errors. The *power* of the cutoff on the other hand is its ability to avoid type II errors.

For an understanding of the power, the background data rejected by each cut is described as well as the background let through to the final spectra. The acceptance on the other hand is investigated by studying the individual cutoffs effect on simulated data.

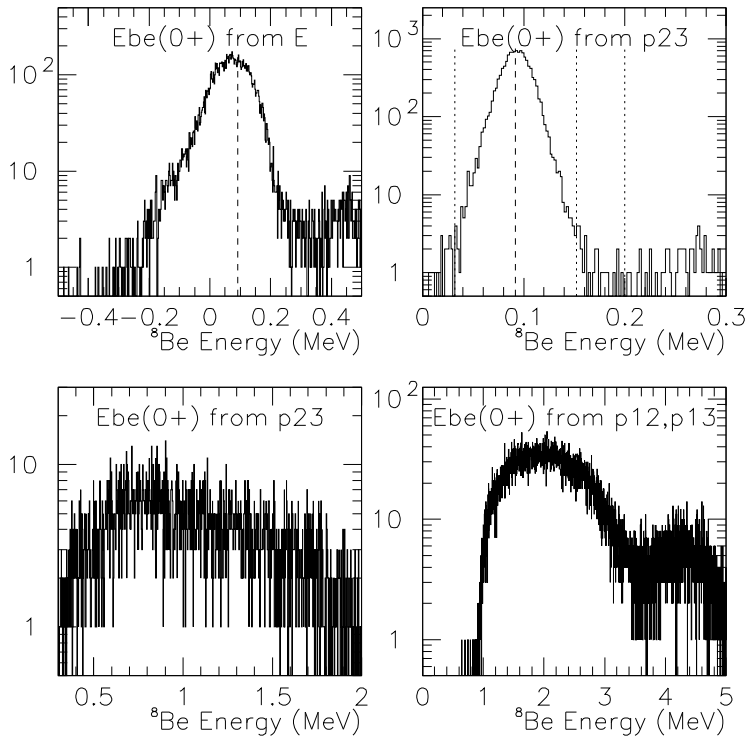

Figure 5.3.4: Upper left frame shows the reconstructed ^{8}Be energy as found from equation 5.3.3 assuming the two lowest energy alphas to originate from the ^{8}Be breakup. The energies in the upper right and lower left frames are reconstructed using equation 5.3.5. The same is the case for the energies plotted in the lower right frame, with the difference, that the first alpha emitted in the decay is not assumed to have the highest energy. The true energy of the ^{8}Be ground state (0.0918 MeV) is indicated as a dashed line.

Cutoff	Exp. data	Sim. ^{8}Be(gs)	Sim. ^{8}Be(ex)
None	12,454,780	1,000,000	200,000
Low energy	657,949	186,462	76,463
Front-back id.	461,393	169,917	70,301
Trigger	149,861	169,917	70,092
At least 3 hits	16,048	30,727	3,572
Sum E and p	15,772	30,727	3,571
^{8}Be ground state	12,225	30,694	17
^{8}Be excited state	3,503	0	3,538

Table 5.4.1: Number of events accepted by individual cutoffs. Data as well as simulations for both a breakup through the ^{8}Be ground state with 3 MeV in total energy and the breakup of the 12.7 MeV 1^+ state through the ^{8}Be 2^+ state.

The first step in understanding the cutoff power and acceptance is to understand how much data is let through each cut until arriving at the final spectra. In table 5.4.1, the total number of events is shown along with the number of events let through each consecutive cutoff. This is shown for the actual ^{12}N decay data as well as for Monte-Carlo simulations of ^{8}Be ground state events from a breaking ^{12}C at 3 MeV above threshold and for the breakup of the ^{12}C 12.7 MeV 1^+ state through the ^{8}Be 2^+ excited state. Though these simulations will not be described in detail until sections 6.2 and 7.3, the individual cutoff acceptances are given here for a coherent description of the cutoff effects. The effect of the cutoffs on experimental data is used for determining the cutoff power, whereas the effect on the simulated data is used to describe the cutoff acceptances and in particular the total acceptance: The energy dependent triple alpha detection efficiency.

5.4.1 Cutoff acceptances

For the simulated data, the number of events shown corresponding to no cutoffs is the total number of generated events. It is clear from table 5.4.1 that the one cutoff with the lowest acceptance is the requirement that a given event must have at least three hits. This is the restriction to only analyze triple coincidence data. Besides this, the identification of front strip — back strip pairs does cut away some data, though not more than 10%. For these energies the trigger threshold is not important, though for lower energies in ^{12}C the acceptance of this cut is decreased. The total detection efficiency is found by comparing the total number of generated events to the number of events in the channel of interest. In the two examples above the efficiencies are 2.7% for the ^{8}Be ground state channel and 1.8% for the ^{8}Be excited state state channel.

5.4.2 Cutoff power and background estimates

From table 5.4.1 alone, the power of the triple coincidence method is clear: Much of the inevitable background, as seen in the total number of analyzed events, does not comply with the triple coincidence requirement and the other cutoff used. The question is now: How much remains.

The background in the ^{8}Be ground state data can be estimated by investigating frame two of figure 5.3.4. In this plot we see a few events to the right of the ^{8}Be peak. This should be considered a potential background. However since the distribution of these events seems to thin out when lowering the energy, it is reasonable to assume we can give an upper limit to the number of such background events in the ^{8}Be ground state region. Between 200 keV and 260 keV we have 25 events corresponding to an upper estimate of 50 events in the region 30 keV to 150 keV. This should be compared to the total number of ^{8}Be ground state events of: 12225. Furthermore it is seen by investigating the ^{12}C energy distribution of the 260–200 keV events that this distribution is not too different from the corresponding distribution of the ^{8}Be ground state events. This shows that, neglecting the effect of this background is a good approximation.

For possible background in the ^{8}Be excited state channel the first approach is to investigate the background indicated by the energy-momentum plot in the left frame of figure 5.3.3. Since the momentum distribution for the removed events is reasonably uniform, an estimate of the background in the accepted region can be found by shifting the momentum down by 80 MeV/c and applying the sum energy-momentum cutoff to these shifted events. This gives the sum energy distribution shown in figure 5.4.1.

Another way of estimating the background distribution is by mixing different events, that is: For two given hits in one event taking the third hit from other events. This can happen experimentally if two physical breakups are recorded as one event by random coincidence because of too high count rate. The method of event-mixing however has the additional advantages that mixing with low energy background is included as well and that no true alpha triples are included, giving a possible background spectrum. The intensity scale on such spectrum however is of course arbitrary, and it will have to be scaled according to the data. This can be done by comparing the energy-momentum plot for the actual data (figure 5.3.3) to the corresponding plot for the event mixed data. This has been done for the momentum range from 80 MeV/c to 100 MeV/c. Yielding the scaled plot shown in figure 5.4.2.

The first background distribution yields an estimate of roughly 150 whereas the second gives an estimate of 75. Note that it is reasonable to assume these estimates to be conservative. Assuming 100 to be a good estimate and comparing this to the original 10^7 events, it yields a power of $1 - 10^{-5}$ for the complete set of cutoffs.

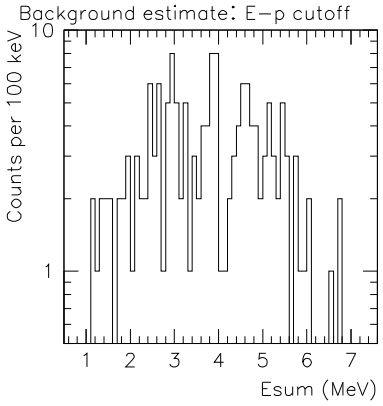

Figure 5.4.1: Background energy distribution estimate for the ^{8}Be excited state channel, found from energy-momentum data plot.

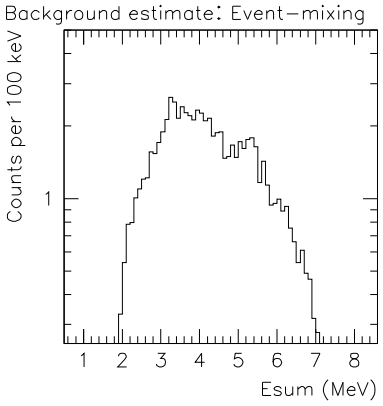

Figure 5.4.2: Scaled estimate of background energy distribution for the ^{8}Be excited state channel, found through event mixing.

5.4.3 Triple versus double coincidence detection

If we only require two alpha particles to be detected we are dealing with double coincidence events. With such an event, the energy and momentum of the undetected alpha particle can be deduced from conservation of momentum since the recoil from the beta decay is very little (as described in section 5.3.2).

As described in the analysis of a previous experiment (Diget et al., 2005) however, triple and double coincidence events yielded consistent results, with the main difference that the double coincidence events are more abundant, reducing the statistical error. An analysis of such data however have no energy-momentum cutoff, and the power of the applied cutoffs for triple coincidence events is therefore higher than the power of the cutoffs applied to get double coincidence data. The systematic uncertainties in this data set is therefore expected to be higher than those for the triple coincidence data. Since it will be clear in the following (section 6.3) that the statistical uncertainties are in general not dominating, including a data set with higher systematic uncertainties and better statistics will not yield a significant improvement to the overall results. For that reason only triple coincidence data will be analyzed in the following chapters.

5.5 Energy spectra

The triple coincidence data is shown in figure 5.5.1 for ^{12}N beta delayed breakup and in figure 5.5.2 for ^{12}B. The complete breakup data including both the ^{8}Be ground state channel as well as the ^{8}Be excited state channel is shown. This "Fynbo plot" was first used in 2000 (Fynbo et al., 2000), and is very illuminating when studying a breakup where two or more breakup channels are possible. This stems from the way kinematics are displayed in such a plot. The plot is a scatter plot of the deduced ^{12}C energy versus the three individual alpha energies. That is: A single event will thereby yield three dots on a horizontal line. If the breakup channel is a narrow state in ^{8}Be, equation 5.3.3 shows the linear relation between the ^{12}C energy and the energy of the first emitted alpha, which is clearly visible in the data. This relation is plotted in the figures as a line with slope 3/2 crossing the E_{sum} axis in 0.0918 MeV. The two remaining alphas sharing the remaining energy are visible as well, centered around a similar line with slope 6. With these scatter plots, many of the physical properties examined in the coming chapters can be seen by first glance. One aspect is the very pronounced structure around 10 MeV in ^{12}C clearly decaying through the ^{8}Be ground state channel and in addition to this the 12.7 MeV 1^+ state in ^{12}C evident not only in the ^{12}N data but in the ^{12}B decay as well. The fact that it is a 1^+ state is immediately visible, since it cannot decay through the ^{8}Be 0^+ ground state (conservation of spin and parity), but must decay through another channel, seen by the completely different sharing of the energy between the three alphas. A third group of breakup events is seen between the two sloped ^{8}Be ground state contributions around 10 MeV in ^{12}C. This is the breakup through excited states of ^{8}Be. The 7.65 MeV Hoyle state is not seen in any of the data sets because of low energy cutoffs.

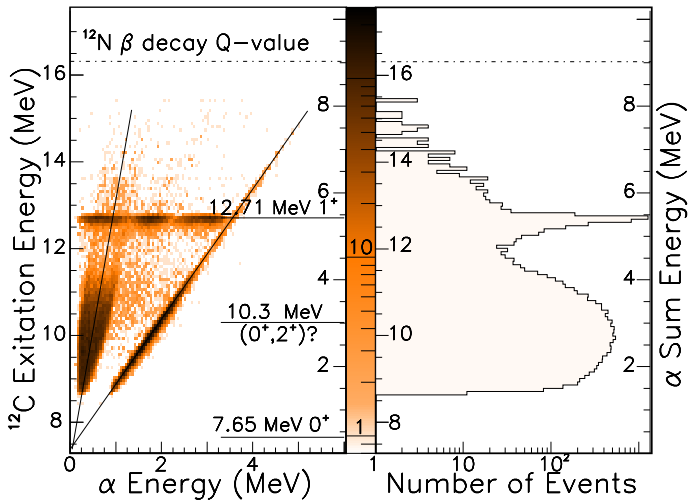

Figure 5.5.1: To the left: Fynbo plot of ^{12}N beta delayed triple alpha breakup. Right hand side is a projection onto the E_{sum} axis.

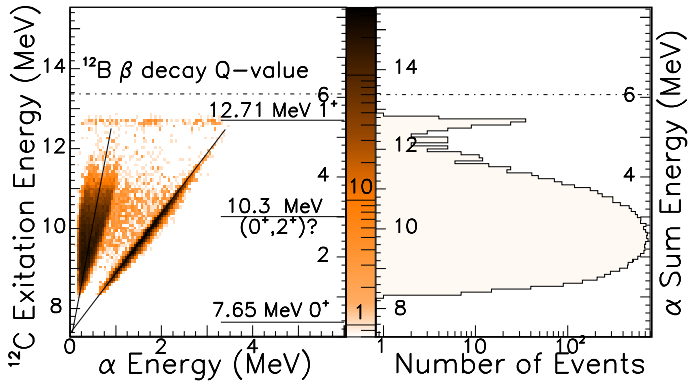

Figure 5.5.2: Equivalent to figure 5.5.1, but for ^{12}B beta delayed triple alpha breakup.

CHAPTER 6

Breakup through the ^{8}Be ground state

6.1 Energy spectrum

As shown in section 5.3.3 the reconstructed energy of the intermediate nucleus ^{8}Be can be used to select events with the ^{8}Be 0.0918 MeV 0^{+} ground state as breakup channel. With this selection, we see two significant contributions to the spectrum. One around 10 MeV and one around 13 MeV. Both broad contributions. This is shown in figure 6.1.1 and 6.1.2. The spectra on the right frames are the ones to be compared to the R-Matrix description, which through fitting will give information on the physical parameters of interest.

6.2 Monte-Carlo simulations

In any experiment, knowing the response of the applied detector setup is crucial. A simple case, is detection of the energy of a single particle with a detector having a constant known detection efficiency in the energy range of interest.

In coincidence detection experiments, such as the experiment presented here, the situation is more complicated. The trigger and low energy threshold for example are not identical. With these thresholds, and other cutoffs, we disturb the spectrum. And even worse, since the energy of the three individual alpha particles depend not only on the ^{12}C energy but as well on the way the three alphas share the energy, the way thresholds effect the detection efficiency depends

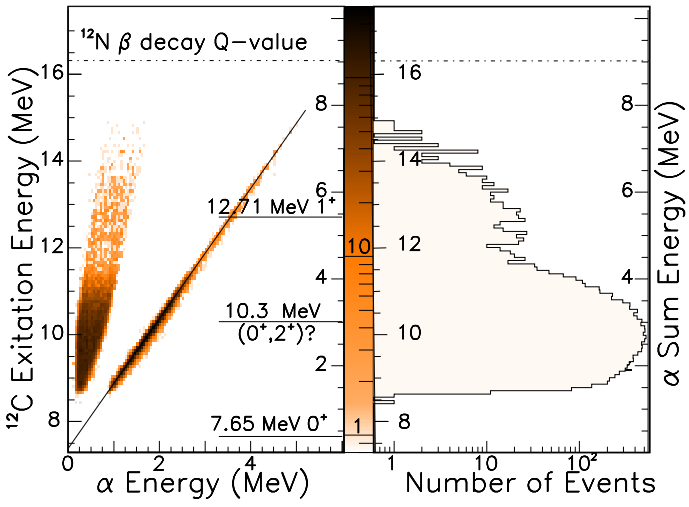

Figure 6.1.1: Fynbo plot of ^{12}N beta delayed triple alpha breakup through the ^{8}Be ground state.

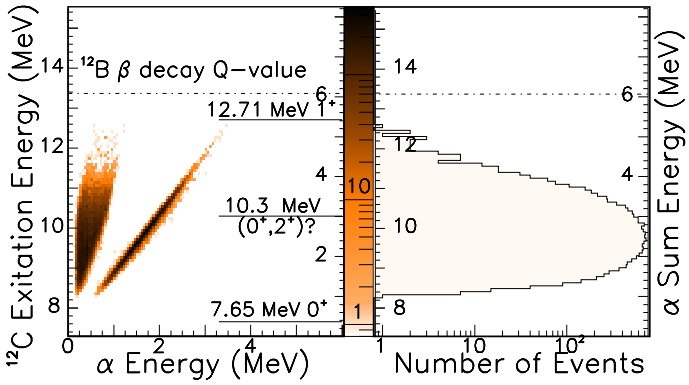

Figure 6.1.2: Equivalent to figure 6.1.1, but for ^{12}B beta delayed triple alpha breakup.

on the breakup channel. Similarly for the geometry: Since our detector setup does not cover all of 4π solid angle, the triple coincidence detection efficiency depends on the relative angles between the three particles and thereby depends on the breakup channel.

The only feasible method for dealing with these effects properly is Monte-Carlo simulations, where triple alpha breakups are simulated for different ^{12}C energies and different breakup channels. This allows a quantitative analysis of the response of the detector setup in combination with the cutoffs applied through the analysis. In the following, such an analysis will be presented for the ^{8}Be ground

state channel. For the ^{8}Be excited state channel the corresponding simulations are presented in chapter 7.

6.2.1 Efficiency, resolution and bias

There are three important steps in such a Monte-Carlo simulation. Firstly a physical description of the breakup process; secondly the effects of the experimental setup; and finally the importance of the data analysis procedures applied to the experimental data.

For a given ^{12}C energy, the energy of the first emitted alpha particle can be found from equation 5.3.3. The direction of this emission follows an isotropic distribution in the laboratory system, since the ^{12}N/^{12}B beam was not polarized, thereby producing a non polarized intermediate ^{12}C state. The direction of the subsequent ^{8}Be breakup relative to the direction of the first alpha is isotropic as well, because the intermediate ^{8}Be ground state has spin 0 and can therefore not be polarized. With this the energy of the two secondary alpha particles can be found by transforming from the ^{8}Be center of mass to the laboratory system i.e. the ^{12}C center of mass system.

When the energies and directions are calculated for all three alpha particles the geometry of the setup allows us to analyze which strips were hit by the alpha particles. Before the detected energies are saved however it is necessary to correct for the energy loss in the foil and the dead layer of the detectors. The energy loss in the foil depends on the implantation depth of the decaying nucleus. This implantation depth distribution is taken from a Srim2003 calculation (Ziegler et al., 2003) or rather an analytical form reproducing the overall shape and especially the mean, width and skewness.

With the energy deposited in each strip have thus been calculated, the individual strip calibration and resolution can be used to generate a simulated event. Such events are then analyzed through the exact same analysis routines as was the data, ensuring that all cutoffs are treated in the exact same way for simulation as was the case for the data. This analysis gives for a ^{12}C input energy of 3 MeV the simulated ^{12}C energy spectrum seen in figure 6.2.1. From this and the total number of simulated events at this energy, the efficiency, E_{sum} resolution and possible bias can be found. In addition, the acceptance after each cutoff can be found by probing the number of events accepted by each cutoff throughout the analysis as discussed in section 5.4. In figure 6.2.3 the efficiency, fwhm triple alpha sum energy resolution and bias are shown as a function of energy for both ^{12}N and ^{12}B. The triple alpha detection efficiency is typically 3–4%, with important energy dependencies. The strong energy dependence of the efficiency at low energies is dominated by the low energy cutoffs and trigger levels. Because of a higher noise level during the ^{12}N data taking requiring an increase in trigger levels this dependence is different for the ^{12}N and ^{12}B simulations. The fwhm resolution is estimated to be around 80 keV with a small energy variation whereas the bias estimate is in the range 0–10 keV for the energies with a sufficient detection efficiency. For the lowest energies, the detection efficiency is so low that 10^{7}

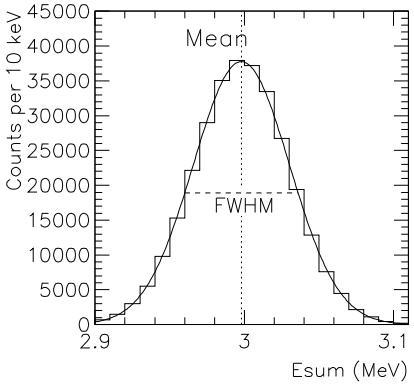

Figure 6.2.1: 10^7 simulated events for a ^{12}C energy 3 MeV above threshold with breakup through the ^{8}Be ground state. Detected 3α sum energies.

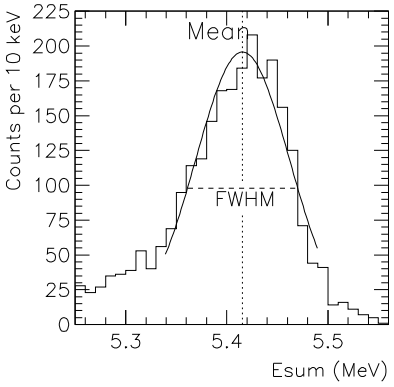

Figure 6.2.2: Triple coincidence resolution found from detected events from ^{12}C 12.71 MeV state. ^{8}Be excited state channel.

events is not sufficient for a good resolution and bias estimate. However because of the low efficiency the amount of data in this energy region is very small, so a good resolution and bias estimate is not crucial.

For comparison a different method for determining the triple coincidence energy resolution is important. Though this involves the data for breakup through the ^{8}Be excited state channel, it is presented here to complete the discussion on the energy resolution. In figure 6.2.2 a part of the detected triple alpha sum energy spectrum is plotted. This corresponds to the right frame of figure 5.5.1. The peak shown here is the 12.71 MeV 1^+ state ^{12}C. By fitting this to a Gaussian distribution an estimate of the resolution and bias can be given. This yields a FWHM resolution of 108 keV and a negative bias of 10 keV. This is in good agreement with the results from simulations through the ^{8}Be ground state channel, and a general triple alpha detection efficiency is chosen as an average of the two, with error bounds including both values.

6.2.2 Beta-neutrino recoil effects

The results shown in section 6.2.1 are simulated by including a β-ν recoil for the ^{12}C nucleus corresponding to the distributions shown in figure 5.3.2. The recoil is assumed to be isotropic relative to the first emitted alpha particle. The validity of this assumption however depends on the spin of the intermediate ^{12}C state, since a ^{12}C spin different from 0 will allow the direction of the beta particle to be correlated to the ^{12}C spin and through this correlated to the direction of the

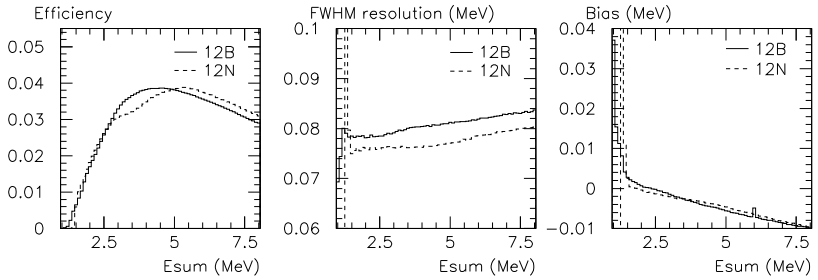

Figure 6.2.3: Efficiency, triple alpha energy resolution and bias found from Monte-Carlo simulation (10^7 events).

first emitted alpha. To be sure that this effect does not introduce systematic uncertainties it is important to have a small recoil.

The effect of the recoil on the detected sum energy and sum momentum is plotted in figure 6.2.4. To make the Monte-Carlo simulations shown here, the $\beta\nu$-recoil is either included or excluded in the generation of the simulated events. The analysis routines on the other hand are the same in both cases, namely the routines used for the analysis of the experimental data. From these simulations it is seen that the $\beta\nu$-recoil effect is indeed modest. The change in the measured sum energy, the energy bias, is less than 1 keV, whereas the average sum momentum is increased by about 1 MeV/c. With a recoil effect this small we will not be sensitive to any correlations between the recoil and the emitted alpha particles.

6.2.3 Beam spot size

Though the best approach for analyzing the experimental data was to neglect the size of the beam spot on the foil, it must be taken into account for a proper simulation of the efficiencies. As in section 6.2.1 it is important to keep the data analysis method identical to the one used for the experimental data, and only change the simulation itself. This is what is done in the following. For simplicity the beam profile is assumed to be a symmetric two dimensional Gaussian distribution, though the shape of the beam spot will most likely be more complicated. The size of the beam spot is then determined from its effect on measured observables by comparing simulated spectra for different beam spot sizes to measured data.

Two observables are especially important in this: The sum energy momentum of the three particles is changed if we assume a wrong decay point, which is exactly what we do for the decays on the rim of the implantation region. Another effect is important as well for these misplaced decays namely the energy loss corrections. Both those in the foil and those in the detector dead layer. If the decay point

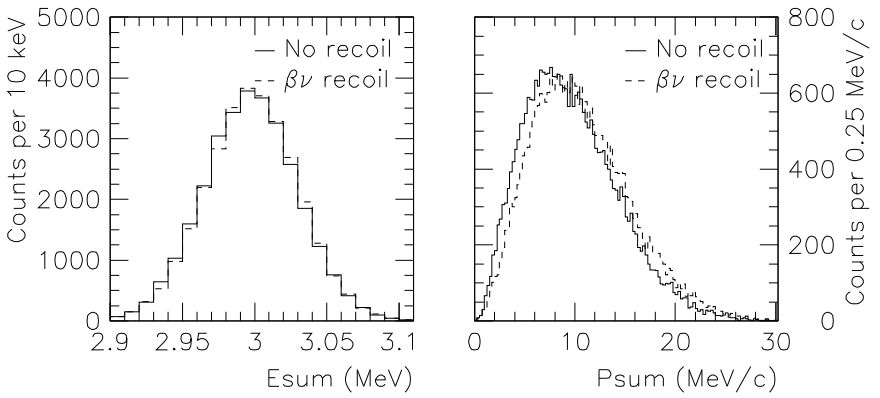

Figure 6.2.4: Beta-neutrino recoil effects in detected sum energy and momentum. Monte-Carlo simulations with 10^6 events.

is shifted a small error is introduced in the calculation of the material traversed by the particle, giving either too high or too low an energy loss. This is most important for the low energy particles where the energy loss is highest. These are the particles from which the ^{8}Be ground state energy is reconstructed according to equation 5.3.5.

A plot of these two observables is shown in figure 6.2.5. In these simulations two different beam spot sizes are compared to the measured data. Unfortunately the simulations turn out to be imperfect, since the 1.0 mm beam spot does the best job in reproducing the ^{8}Be distribution whereas a 2.3 mm beam spot gives a better reproduction of the total momentum distribution. To take this discrepancy into account properly we must accept to have an uncertainty in the beam spot size. This gives rise to a systematic uncertainty in the efficiency as can be seen in figure 6.2.6 and through this an uncertainty in the fitted spectrum. The implications from this on the deduced ^{12}C state properties will be dealt with in section 6.3.7.

6.2.4 Uncertainties in setup geometry

As for the beam spot size, the overall geometry is only known to a certain precision. With the used mounting of the detectors the measured relative angles of detectors, foil and beam has an uncertainty of approximately two degrees. In addition to this, the foil thickness is known to be 30 μg/cm^2 within 10–20%. These uncertainties could potentially be an important contribution to the systematic uncertainty in the fitted parameters, however we do have some additional restric-

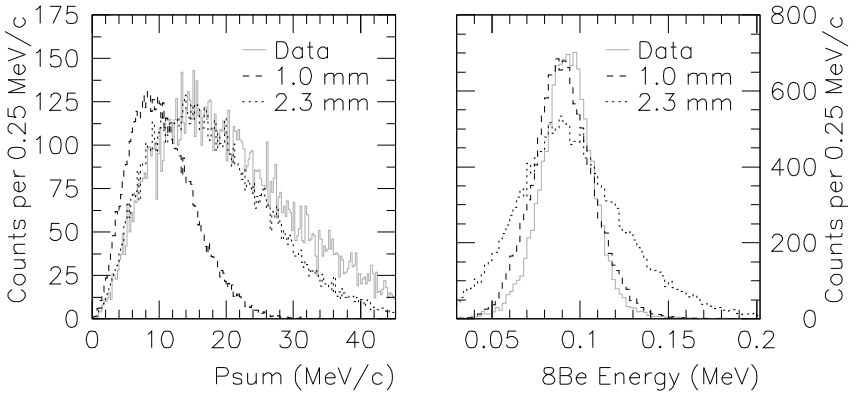

Figure 6.2.5: Beam spot size influence on detected triple alpha sum momentum and reconstructed ^{8}Be ground state energy. 10^6 events Monte-Carlo simulations compared to data.

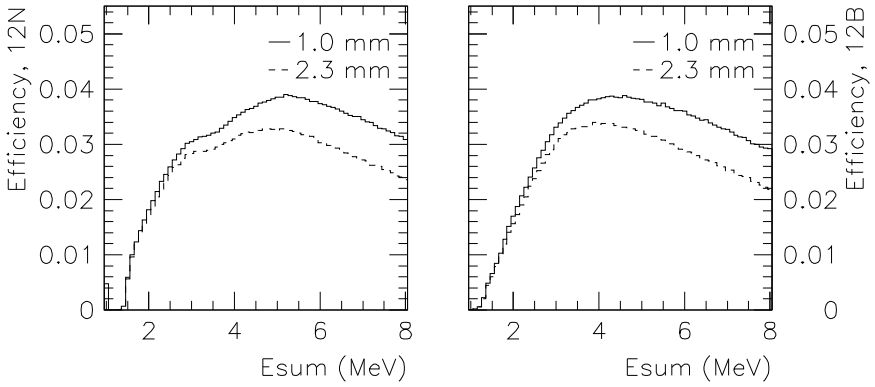

Figure 6.2.6: Beam spot size dependence of triple alpha detection efficiency.

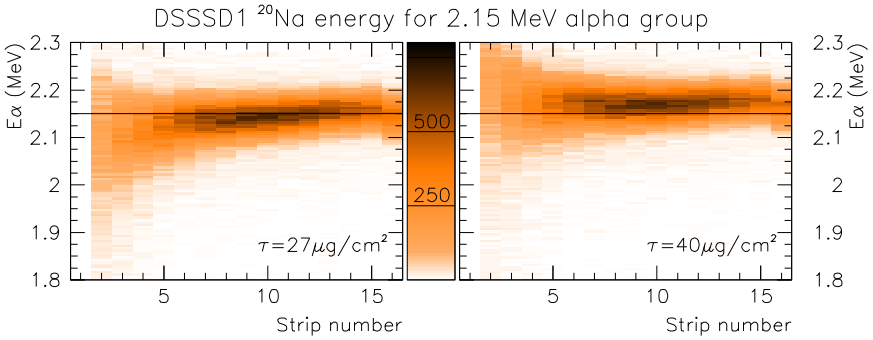

Figure 6.2.7: ^{20}Na data corrected for foil energy loss and dead layer effects. Two different foil thicknesses (τ).

tions on the geometry coming from the effect of changes in the geometry on the energy loss corrections described in section 5.1.3.

In figure 6.2.7 it is shown how these energy loss corrections can be used to test the foil thickness. The plot shows the alpha energy at the decay point calculated from the detected alpha energy and the energy loss corrections calculated for two different setup assumptions. One calculation assuming a $27\,\mu g/cm^2$ foil and one assuming a $40\,\mu g/cm^2$ foil. Strip 1 is close to the foil plane whereas strip 16 is almost perpendicular to the foil plane making the left strips in both plots very sensitive to changes in the foil thickness. From the two plots shown here, it is seen that for a foil width of $27\,\mu g/cm^2$, the applied energy correction is to small, making a downwards bend in the plot. With a $40\,\mu g/cm^2$ foil on the other hand, the energy correction is too large, giving the plot an upwards bend. With this and similar plots for other foil thicknesses in between the two plotted here, we find a best value of the thickness of $33 \pm 3\,\mu g/cm^2$. This procedure can as well be applied to place restrictions on the geometry, for this however we must use the sum momenta for triple alpha events as well. The use of this was illustrated in section 5.1.2, where it was shown how the beam spot position could be found from requiring the three sum momentum projections p_x, p_y and p_z to be zero on average for the triple alpha coincidence events. This can be used again here, since for some assumptions of the geometry this beam spot position would have to be outside the foil plane to fulfill the sum momentum requirement, allowing us to discard some geometries.

With these restrictions on geometry, the effects on the triple alpha detection efficiency from varying the geometry is found through Monte-Carlo simulations as in the previous sections. The result of these simulations is shown in figure 6.2.8 where four different geometry assumptions have been tested and the deduced efficiency compared to the efficiency calculated in section 6.2.1. It is clearly

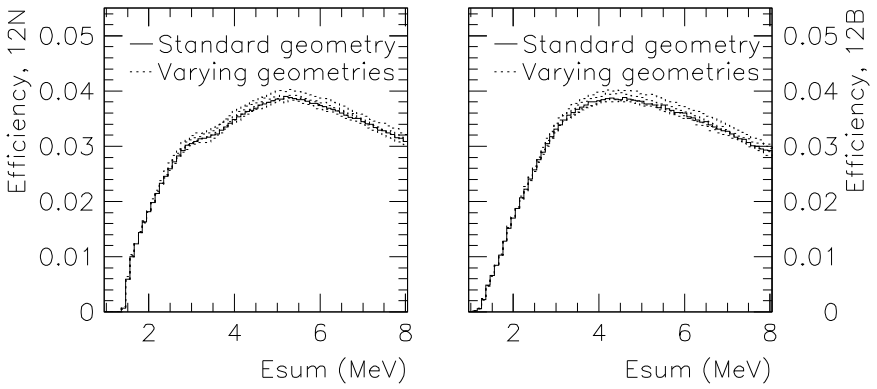

Figure 6.2.8: Effect of uncertainties in setup geometry on the triple alpha detection efficiency.

seen that the efficiency is not altered as much as was the case for the variation of the beam spot size. The systematic uncertainties arising from the geometry uncertainties however will still be investigated in the following chapter.

6.3 ^{12}C states and their properties

With the experimental data under control we are ready to proceed to the physical interpretation. That is, the fitting of our R-Matrix model of the beta delayed alpha emission (section 3.2) to the data. In the following, the fitting procedure will be explained and restrictions on the physical properties of the investigated ^{12}C states will be deduced from the fits. In addition to this a thorough analysis of systematic errors will be given.

6.3.1 Phase space and efficiency corrections

The first step in the fitting procedure is to compare the data sets for ^{12}N and ^{12}B to confirm that a combined analysis of the two spectra is reasonable. There are however important differences between the two data sets both physically and technically. The physical difference between the two decays is first and foremost the Q value. Through this the beta phase space is different for the two decays thereby making the f-factor differ for the two decays at any given ^{12}C energy.

To compare the two data sets we must therefore correct the two by their respective f-factors. Such a spectrum is shown in figure 6.3.1 where the overall

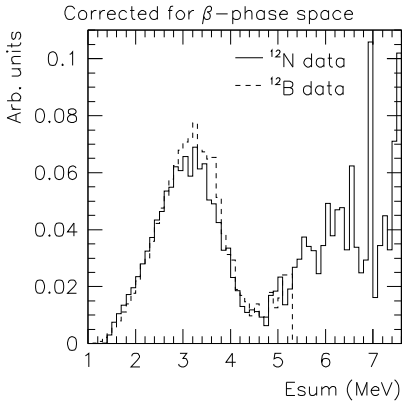

Figure 6.3.1: ^{12}N and ^{12}B spectra corrected for β-phase space f-factor.

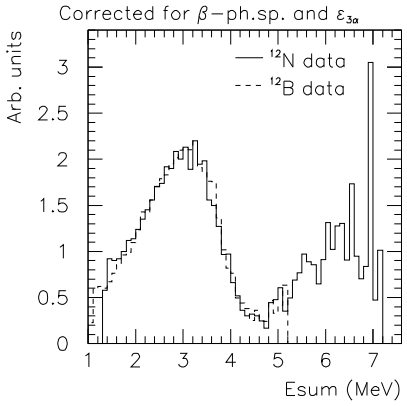

Figure 6.3.2: ^{12}N and ^{12}B spectra corrected for β-phase space and detection efficiency.

consistency of two spectra is apparent. The only exception being the 3–4 MeV range where the ^{12}B data exceeds the ^{12}N data by about 15%. This however is hardly surprising, since this is exactly where the detection efficiencies (figure 6.2.3) differ for the two data sets. If we correct the spectra by the detection efficiencies as well, we get the spectra shown in figure 6.3.2 where the consistency is evident.

This shows two important aspects of the present data and analysis. Firstly it shows very clearly the expected isospin symmetry of the two decaying nuclei. This aspect will be elaborated on in chapter 8 where the branching ratios and B_{GT} values of the two decays are compared. Secondly it confirms that efficiencies are well understood by showing that the differences between the two simulated efficiencies are in fact reflected in the data sets. Though Monte-Carlo simulations can be considered a well established method (Eidelman et al., 2004), it is an important property of the data that the data itself confirms the validity of this key method in our analysis.

6.3.2 Maximum likelihood fitting

Fitting is too often seen as just a formalized method for estimating a set of parameters from a measured data set. In addition to the parameter estimation however, two other aspects must be considered namely estimation of confidence intervals for the parameters and goodness-of-fit tests. The maximum likelihood fitting introduced in the following is capable of dealing with all three parts. The notation here will essentially follow that used by Baker & Cousins (1984),

whereas for a thorough description of the method and other statistical aspects of data analysis the review of Eadie et al. (1971) is very recommendable.

First a bit of notation: Our goal here is to describe a binned data set of n_{bin} bins $\mathbf{n} = (n_1, \ldots, n_{nbin})$ by a model described by n_{par} parameters $\alpha = (\alpha_1, \ldots, \alpha_{npar})$. On these parameters some constraints may be set, allowing only some values of α. We will furthermore let $\mathbf{y} = (y_1, \ldots, y_{nbin})$ denote the number of events in each bin as predicted by the model. With this in hand we can define the Poisson likelihood function as the probability of measuring the actual data set under the condition that bin i is drawn from a Poisson distribution of mean y_i. That is:

$$L_p(\mathbf{y}; \mathbf{n}) = \prod_i \exp(-y_i) \frac{y_i^{n_i}}{n!} \tag{6.3.1}$$

the product of the corresponding likelihoods for the individual bins. This factorization is only correct if the number of events in the individual bins are independent. The best fit to the data is the set of parameters that maximizes the likelihood function. It is however more convenient to work with the log likelihood ratio:

$$\chi^2_\lambda = -2 \ln \left(L_p(\mathbf{y}; \mathbf{n}) / L_p(\mathbf{n}; \mathbf{n}) \right) = 2 \sum_i y_i - n_i + n_i \ln \left(\frac{n_i}{y_i} \right) \tag{6.3.2}$$

Where the likelihood $L_p(\mathbf{n}; \mathbf{n})$ is the likelihood of the observed data assuming the best possible fit function with no restrictions on parameter space, namely the function having $y_i = n_i$. The likelihood ratio is as well known as the likelihood chi squared, since asymptotically it behaves as a χ^2 distribution. This function should then be minimized over the allowed parameter space. The minimization is done using the CERN package MINUIT (James, 1994).

The next step in the analysis is the confidence interval estimation. This is where the likelihood chi squared shows its worth. It is clear that if the likelihood (6.3.1) is very small compared to the best fit, the parameters must be far off the best value, "far off" understood in terms of the uncertainties of the fitted parameters. This can be quantified through the behavior of the likelihood chi squared around its minimum. If the likelihood chi squared is parabolic in all parameters, the 1σ limits (68.3% confidence interval) on a given parameter is the value at which χ^2_λ has increased by 1. In general an increase of k^2 gives the $k\sigma$ confidence intervals. In the following however only the 1σ limits will be given. For the general case, where χ^2_λ is not parabolic, it is not as easy to identify the confidence intervals, it is however still true that an increase of k^2 gives the $k\sigma$ confidence interval. In MINUIT this is facilitated by the MINOS routine, which estimates the confidence interval on a parameter by changing the parameter slightly and minimizing the others. This is done until the upper and lower bounds on the parameter is identified. This method may be important to use even for symmetric confidence intervals, since the parabolic approximation can be very bad even for the symmetric case.

It is worth noting that when two different models with identical *npar* are fitted to the same data, the two models can be compared in exactly the same way. That is if the minimum values for their respective likelihood chi squared differ by e.g. 9 the one with the higher value is excluded at the 3σ level.

The last part of the fitting is the goodness-of fit test. There are many ways to test the goodness of a fit. Here only one method is presented, since the maximum likelihood method provides such a test as well. The reason for this is the fact that the χ^2_λ behaves asymptotically like a χ^2-distribution. That is for different data sets describing the same theoretical function, $\sqrt{2\chi^2}$ follows a Gaussian distribution of standard deviation 1 around $\sqrt{2n_d - 1}$, where $n_d = n_{bin} - n_{par}$ is the degrees of freedom. This is very helpful when trying to reject a fit as a bad fit, purely on grounds of its goodness.

6.3.3 Data fits

When fitting the parameterized R-Matrix model to the data, we first correct the model by the detection efficiency and integrate over an experimental resolution of 96 keV FWHM. Note that the corrections are not done on the data as in section 6.3.1. This is because correcting for the efficiency would prevent the bin values from being Poisson distributed, in which case a different statistic should be used. Unfolding the resolution from the data would be even worse, since this would introduce correlations between the individual bins in the corrected histogram.

The R-Matrix model can deal with several states and interference between the states of same spin and parity. As described previously we already know from beta decay selection rules and spin-parity conservation in the subsequent breakup, that only 0^+ and 2^+ states can contribute to beta delayed triple alpha breakup through the ^{8}Be(0^+) ground state. Therefore only 0^+ and 2^+ states will be included in the R-Matrix description. In addition to this we will as always in R-Matrix theory try to describe the data with as few contributing states as possible, reducing the number of fitting parameters as much as possible.

For one 0^+ state and one 2^+ state in addition to the 7.654 MeV 0^+ Hoyle state, the describing function has 10 parameters in total for the two spectra. For each of the two levels it has: The level energy E_λ; the reduced width γ_λ; and the feedings to the level relative to the feedings to the Hoyle state $g^N_{\lambda,GT}$ and $g^B_{\lambda,GT}$. Note that the data presented here is not sensitive to the absolute value of these feedings since we have no absolute normalization of the spectra. We know that the energy and width of the levels cannot differ for the two spectra, whereas the relative feedings for the levels may be different for the two. In addition to these 8 parameters we have the two factors C_N and C_B scaling the ^{12}N and ^{12}B decay spectra respectively. Such a 10 parameter fit is shown in figure 6.3.3. Yielding the parameters for the three levels (0^+, 0^+ and 2^+) to be the ones shown in table 6.3.1. Where the uncertainties are statistical uncertainties only, and the values for the Hoyle state (*) are those given by Ajzenberg-Selove (1990). The difference in the sign of γ_1 and γ_2 means the two states interfere constructively in the energy region between the two.

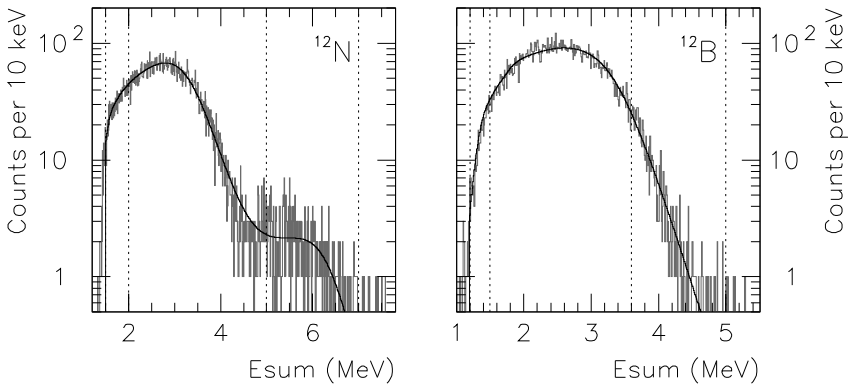

Figure 6.3.3: ^{12}N and ^{12}B spectra and a combined fit to both spectra.

λ	E_λ (MeV)	γ_λ (MeV$^{\frac{1}{2}}$)	$g^N_{\lambda,GT}$	$g^B_{\lambda,GT}$
1	7.6542(∗)	0.59803(∗)	1.0	1.0
2	12.33(6)	−0.766(14)	0.217(16)	0.292(21)
3	13.59(13)	0.419(24)	0.470(32)	0.27(11)

Table 6.3.1: R-Matrix parameters (described in section 3.2) for an $r_0 = 1.87\,\mathrm{fm}$, $0^+0^+2^+$ state fit. Uncertainties on Hoyle state parameters (∗) are discussed in section 6.3.8.

As described in section 3.2, the R-Matrix parameters above must be transformed to get the physical observables for the states, the observed energy and width, along with the relative feeding matrix elements for the states compared to that of the Hoyle state. Because of correlations between the individual parameters, it turns out that the statistical uncertainties on the observed parameters are in general smaller than the corresponding uncertainty of the R-Matrix parameter. With this, however the statistical uncertainties are smaller than the systematic errors found in the following, and only the values of the observed parameters are stated in table 6.3.2. The observed width for the Hoyle state ($\lambda = 1$) is shown as well to illustrate how similar reduced widths can reflect completely different widths.

λ	E^o_λ (MeV)	Γ^o_λ (MeV)	$M^N_{GT;\lambda}/M^N_{GT;h}$	$M^B_{GT;\lambda}/M^B_{GT;h}$
1	7.6542	$7.65 \cdot 10^{-6}$	1.0	1.0
2	11.19	2.47	0.45	0.52
3	13.59	1.58	0.47	0.27

Table 6.3.2: Observed parameters for an $r_0 = 1.87\,\text{fm}$, $0^+0^+2^+$ state fit. For notation see section 3.2.

Fit	Ranges (MeV)	E_2 (MeV)	γ_2 (MeV$^{\frac{1}{2}}$)	E_3 (MeV)	γ_3 (MeV$^{\frac{1}{2}}$)
1	[1.5:7.0,1.2:5.0]	12.33(6)	−0.766(14)	13.59(13)	0.419(24)
2	[1.5:7.0,1.2:3.6]	12.34(7)	−0.775(16)	13.61(13)	0.417(25)
3	[1.5:7.0,1.5:5.0]	12.30(6)	−0.756(14)	13.59(12)	0.422(24)
4	[1.5:7.0,empty]	12.15(7)	−0.710(17)	13.63(16)	0.445(28)
5	[2.0:7.0,1.2:5.0]	12.33(6)	−0.765(14)	13.59(13)	0.421(24)
6	[1.5:5.0,1.2:5.0]	11.85(7)	−0.588(24)	10.44(11)	1.06(13)
7	[empty,1.2:5.0]	12.00(17)	−0.654(49)	10.27(27)	1.14(28)
8	[empty,1.2:5.0]	12.54(11)	−0.821(21)	13.60(∗)	0.41(∗)

Table 6.3.3: R-Matrix parameters for different fit ranges. See text for discussion on fitted parameters.

6.3.4 Fit ranges

The fit above were carried out as a combined fit for the ranges [1.5:7.0] and [1.2:5.0] in the ^{12}N and ^{12}B data respectively. To test the robustness of the fit, fits for 7 different sub-ranges are done, including fits to only one of the two data sets. Table 6.3.3 shows four of the estimated R-Matrix parameters and their statistical uncertainty.

It is clear that we are not sensitive to the lower bounds on the ranges. For the high energy bound in the ^{12}N data on the other hand, a strong sensitivity is seen. This is because this fit only includes the broad peak around 3 MeV. With this assumption we have three states to describe this region instead of two. If instead we require the third state to be defined from the full ^{12}N data fit, the ^{12}B data (fit 8) gives parameter estimates not too different from those found from the ^{12}N data. The difference cannot be explained purely by the statistical errors, but as will be seen in section 6.3.7 the two fits are consistent when taking the systematic uncertainties into account, making a combined fit to the two spectra meaningful.

6.3.5 Different ^{12}C configurations

For up to three states in ^{12}C of either 0^+ or 2^+ character, where the lowest of the three (the Hoyle state) is known to be a 0^+ state, there are 6 possible

Fit	States	χ^2_λ	Δ_χ	States	χ^2_λ	Δ_χ	Fit
1	0	5900	65.5	$0+2$	1698	15.3	8
2	$0+0$	3289	38.1	$0+0+2$	1280	7.7	9
3	$0-0$	1578	13.2	$0-0+2$	954	0.7	10
4	$0+0+0$	1715	15.6	$0+0+2^*$	1206	6.2	11
5	$0+0-0$	1446	10.9	$0-0+2^*$	1698	15.3	12
6	$0-0+0$	988	1.5	$0+2+2$	1673	14.9	13
7	$0-0-0$	1525	12.3	$0+2-2$	1184	6.0	14a
				$0+2-2^{**}$	923	0.0	14b
				$0+2-2^{**}$	946	0.6	14c

Table 6.3.4: Goodness-of-fit for all possible ^{12}C state configurations.

combinations: 0^+, 0^+0^+, $0^+0^+0^+$, 0^+2^+, $0^+0^+2^+$ or $0^+2^+2^+$. In addition to this, for the $0^+0^+2^+$ configuration, it is possible to have either the 2^+ or the 0^+ as the lowest energy level of the two. A further complication when two or more states have the same spin—which is certainly the case for three levels—is the possibility of either constructive or destructive interference. In total this adds up to 14 different possibilities as shown in table 6.3.4. The sign in front of a state identification gives the sign of the reduced width of the state relative to that of the lowest energy state of the same spin. As described in section 6.3.2, for goodness-of-fit tests the difference: $\sqrt{2\chi^2} - \sqrt{2n_d - 1}$ is important since it can be used to describe how good (or bad) a fit is. In the table this difference is denoted Δ_χ, and is calculated taking into account $n_d = 930, 926, 922$ for one, two and three state fits respectively. In all of the fits the high energy limits on the level energies are set to 20 MeV. Except in $(*)$ where in addition the 2+ state was required to have the second lowest level energy, giving the second 0+ state the highest energy of the three states. In the two last fits $(**)$ the upper limit of the second 2^+ state energy was set to 30 MeV and in 14c an additional requirement was set on the relative feeding of the third level.

The first thing to notice from table 6.3.4 is the fact that several of the fits seem promising when looking at the Δ_χ value. This is true for fit 6, 10, 14b and 14c especially. It is clear as well that none of the two level fits reproduce the data, leaving us with only the different three level fits. For these it is easy to compare the χ^2_λ values directly. Keeping in mind that a difference of k^2 in χ^2_λ corresponds to a $k\sigma$ rejection of the worst model, it is easily seen that all of the remaining combinations are rejected at more than the 10σ level when comparing to any of the four. It is clear that the best of these fits is the 14b fit, but before we reject any of the four, we will for a moment look at some of the parameters for the four fits, namely: The observed energy; the dimensionless reduced gamma; and the matrix element ratio for the ^{12}N decay. These parameters are shown in table 6.3.5 where it is clearly seen that the 14b and 14c fits prefer a very high value of the observed energy for the third level. This in itself is not a problem,

Fit	States	λ	E^o_λ (MeV)	θ'_λ	M^N_λ/M^N_H
6	$0-0+0$	2	11.17	-0.645	0.51
		3	13.94	1.020	0.30
10	$0-0+2$	2	11.18	-0.940	0.45
		3	13.59	0.659	0.47
14b	$0+2-2$	2	11.24	1.109	0.31
		3	29.85	0.578	16.39
14c	$0+2-2$	2	10.68	1.057	0.45
		3	27.07	3.65	1.99

Table 6.3.5: R-Matrix parameters for the best three level fits.

since the low energy tail of such a high energy level in R-Matrix theory can be interpreted either as a non resonant $L = 2$ triple alpha continuum contribution to the spectrum or simply a broad level at high energy.

There is however another problem when giving the level parameters a closer inspection. The matrix element ratio $M^N_\lambda/M^N_H \approx 16$ is very high for the 14*b* fit. What this fit suggests is therefore that the B_{GT} value (proportional to M^2) should be roughly $50^2 = 2500$ times as large as the coupling to the resonant 2^+ state (level 2) and $16^2 \approx 250$ times as large as that of the Hoyle state. This is not consistent with the traditional triple alpha cluster interpretation of the Hoyle state and the 2^+ states included in the fit. Furthermore, if we calculate the B_{GT} value of the Hoyle state from the literature value of the ft value ($\log ft = 4.34$ according to Ajzenberg-Selove (1990)) and the relation in equation 3.2.8, we get a B_{GT} value of 0.175 for the Hoyle state. With the ratio mentioned above, this corresponds to a B_{GT} value of about 40 for the higher lying 2^+ state, in conflict with the inequality deduced from the Gamow-Teller sum rule. If on the other hand we require the feeding to level 3 to be more reasonable (fit 14c), the width increases drastically, yielding a dimensionless reduced width of $\theta'_\lambda = 3.65$ corresponding to an observed width of $\Gamma^o_\lambda = 104\,\text{MeV}$. This value of θ'_λ does not comply with the Wigner limit introduced in section 3.2.3, and must thus be rejected. In both of these cases the resulting fit is thus outside the physically acceptable parameter space, and when leading the fits back inside the physically feasible parameter space we end up with a fit like 14*a* which was already rejected on grounds of its χ^2_λ value. The essence of the $0+2-2$ fits is thus that such a three level R-Matrix analysis only reproduces the data if the third level has a very high energy. This high energy will in turn require either an extremely high feeding to this level or an unphysically large width.

This leaves us with only two possibilities: $0-0+0$ (fit 6) and $0-0+2$ (fit 10), for which the difference in χ^2_λ is 34, close to a 6σ rejection of the $0-0+0$ state combination. The following sections will therefore focus on the $0^+0^+2^+$ combination fit with negative sign of the 0^+0^+ state interference.

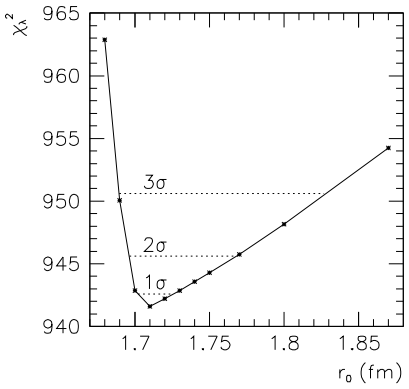

Figure 6.3.4: Best fit χ^2_λ as a function of r_0.

6.3.6 The channel radius

As discussed in chapter 3 the channel radius $a_0 = r_0\left(A_1^{1/3} + A_2^{1/3}\right)$ is actually a free parameter and it should be determined from the data, if not given by previous experiments. For different values of r_0, the data is therefore fitted to the $0^+0^+2^+$ configuration, and the resulting minimum values of χ^2_λ are plotted as a function r_0. This is shown in figure 6.3.4, from which we clearly see that $r_0 = 1.87\,\text{fm}$ as used in the preceding is not the best value. A best estimate is $r_0 = 1.71\left(^{+2}_{-1}\right)$ fm, where the asymmetric confidence interval stems from the shown χ^2_λ dependence on r_0.

With these bounds on r_0 we can deduce the systematic uncertainties on the observed parameters arising from correlations with r_0. This is shown in figure 6.3.5 where the best fit (standard) is compared to those for the upper and lower bounds of r_0. It is clear that this contribution to the total uncertainty is most important for widths and energies.

6.3.7 Setup related systematic uncertainties

In sections 6.2.3 and 6.2.4 we saw that uncertainties in beam spot size and overall geometry had an effect in the simulated detection efficiency. Through this it will naturally influence the parameter estimates. As seen in figure 6.3.5 the effects are very different for the individual parameters. It is natural that the deduced feeding (M_3^X/M_H^X) differs significantly for the standard (1.0 mm) and test (2.3 mm) beam spot size, since their respective efficiencies (figure 6.2.6) differ significantly in the high energy region.

The uncertainty in resolution described in section 6.2.1 however introduces very little uncertainty in the fitted parameters as can as well be seen from figure 6.3.5.

6.3.8 Uncertainties on Hoyle state parameters

The Hoyle state energy is very well determined with an uncertainty of only 0.2 keV (Nolen & Austin, 1976). The Hoyle state width however is only determined within 12% to 7.65 eV. Note that this value differs a bit form that stated by Ajzenberg-Selove (1990) and is found from the two values of Γ_π/Γ and Γ_π identified by Alburger (1977) and Crannell et al. (2005) respectively.

This uncertainty is taken into account by finding the best fit channel radius for a Hoyle state width (Γ_H^o) of 6.73 eV and 8.57 eV in addition to the standard 7.65 eV. The best estimate of r_0 was found to be 1.67 fm and 1.74 fm respectively, and the estimates of the remaining parameters found. This yielded the values shown in figure 6.3.5, where $\Gamma_H^o = 8.57$ eV gives the highest values for all of the $\lambda = 2$ state parameters. Not surprisingly, the Hoyle state uncertainty is most important for the $\lambda = 2$ state, since it is at the lowest energy and interfering with the Hoyle state. This uncertainty will be reduced when Sam Austin and collaborators will re-measure the pair branching Γ_π/Γ of the Hoyle state in the near future (Austin, 2005; Tur & Austin, 2006).

The best fit χ^2_λ values for the three Γ_H^o values: 6.73 eV, 7.65 eV and 8.57 eV were found to be 938.7, 941.6 and 944.5 respectively showing a 1–2σ preference for the lower bound value compared to the central value. Caution however should be taken since this may be influenced by details of the spectrum not accounted for by the simple three level, one channel model described here. This does nonetheless point to an important application of studying the 10 MeV region of ^{12}C, namely that the total width of the Hoyle state may be probed by its effect in the 10 MeV region. Such a measurement will be a valuable independent test of the Γ_π/Γ, Γ_π measurements especially since the present measurements (Crannell et al., 2005) and (Strehl, 1970) of Γ_π are inconsistent at about the 2σ level. This is essential for the measurement of the radiative width of the Hoyle state $\Gamma_\gamma + \Gamma_\pi$ which at present is the primary source for uncertainty in the triple alpha reaction rate calculations at temperatures corresponding to the helium burning in the Asymptotic Giant Branch (AGB) stars (Austin, 2005). If the triple alpha spectrum could be measured well below the cutoffs necessary in a coincidence measurement such as this, the measured spectrum may prove sensitive to the strong correlations experienced here between the Hoyle state width and the channel radius.

Such an experiment has just been performed using in-detector decay of ^{12}N and ^{12}B, as described in section 2.5. If the systematic uncertainties from the beta background and beta summing can be controlled sufficiently, this may provide the needed independent detection of the Hoyle state width.

J^π_λ	E^o_λ (MeV)	Γ^o_λ (MeV)	M^N_λ/M^N_H	M^B_λ/M^B_H
0^+_1	7.65420(15)	$7.65(90)\cdot 10^{-6}$	1.0	1.0
0^+_2	$11.47(^{+14}_{-14})(^{+5}_{-7})$	$3.44(^{+20}_{-20})(^{+25}_{-30})$	$0.361(^{+10}_{-10})(^{+35}_{-8})$	$0.430(^{+10}_{-10})(^{+25}_{-20})$
2^+_3	$13.61(^{+14}_{-11})(^{+2}_{-3})$	$1.68(^{+17}_{-17})(^{+2}_{-9})$	$0.447(^{+32}_{-26})(^{+40}_{-10})$	$0.29(^{+9}_{-12})(^{+4}_{-2})$

Table 6.3.6: Final estimates of observed parameters with uncertainties. This fit is an $r_0 = 1.71\,\text{fm}$, $0^+0^+2^+$ state fit with negative sign of the 00 interference. The first uncertainty is the statistical, whereas the second is the systematic.

6.3.9 Conclusions

With this we must conclude from the beta delayed triple alpha breakup through the ^{8}Be ground state, that the data is well described by a three level R-Matrix model. Furthermore that of the three ^{12}C states corresponding to the three levels, the second lowest must be a 0^+ state interfering with the 0^+ Hoyle state known to be the lowest state in the triple alpha continuum. For the third state there is a strong (6σ) preference for the spin and parity to be 2^+, giving no interference with the two lower lying states.

Regarding uncertainties of the observed parameters, the systematic are taken from figure 6.3.5 whereas the statistical errors are estimated from the corresponding errors on the R-Matrix parameters. This yields the results for the three examined continuum states shown in table 6.3.6, where only the results for $\lambda = 2, 3$ are from this experiment, but all three are listed for completeness. Furthermore, since the systematic uncertainty, and in particular the uncertainties coming from the channel radius and the uncertainty in the Hoyle state width are so important to the total uncertainty in the final parameter estimates, we must conclude that this type of experiment cannot be improved significantly with regards to detection of the breakup through the ^{8}Be ground state.

To the results in table 6.3.6, one further complication is actually added. This stems from the fact that the ^{8}Be ground state channel is not the only breakup channel of the ^{12}C states. Breakup through higher energies in ^{8}Be is possible as well. This breakup mode is dealt with in detail in the following chapter. Here however we must be aware of the way the results stated in the table can be affected by the other breakup channel. Having such additional breakup channels actually means the level matrix is slightly different, since the contribution from the othre channels must be included as described in equation 3.4.4.

As will be seen in the following chapters (directly seen in figure 8.1.1) the branching ratio for the ^{8}Be high energy breakup channels in the breakup of the 0^+_2 state is modest (about 10%). For the 13.6 MeV 2^+ state on the other hand, the contribution from these breakup channels is significant. Because of this, I will expect the inclusion of these channels to have a modest (about 10% decrease) and significant (up to 50% decrease) in the partial widths to the ^{8}Be ground state channel for the two states respectively. For the total widths, as

well as the positions of the states, no significant effect is expected. So as long as Γ_λ^o is understood as the total observed widths of the states, the estimates in table 6.3.6 still holds true. Since the Hoyle state (0_1^+) and the 0_2^+ state behaves similarly in the 10 MeV energy region of ^{12}C with regards to the ^{8}Be high energy breakup channel, the matrix element ratios fro the 0_2^+ state are furthermore not expected to to be affected by this channel. For the 13.6 MeV state on the other hand the feeding strength—that is, the square of the matrix elements—could potentially be altered with up to a factor of two increase in the worst case scenario. The incertainty introduced by this should therefore be taken into account when estimating uncertainties of ${M_\lambda}^2$ in section 8.6 (the B_{GT} values).

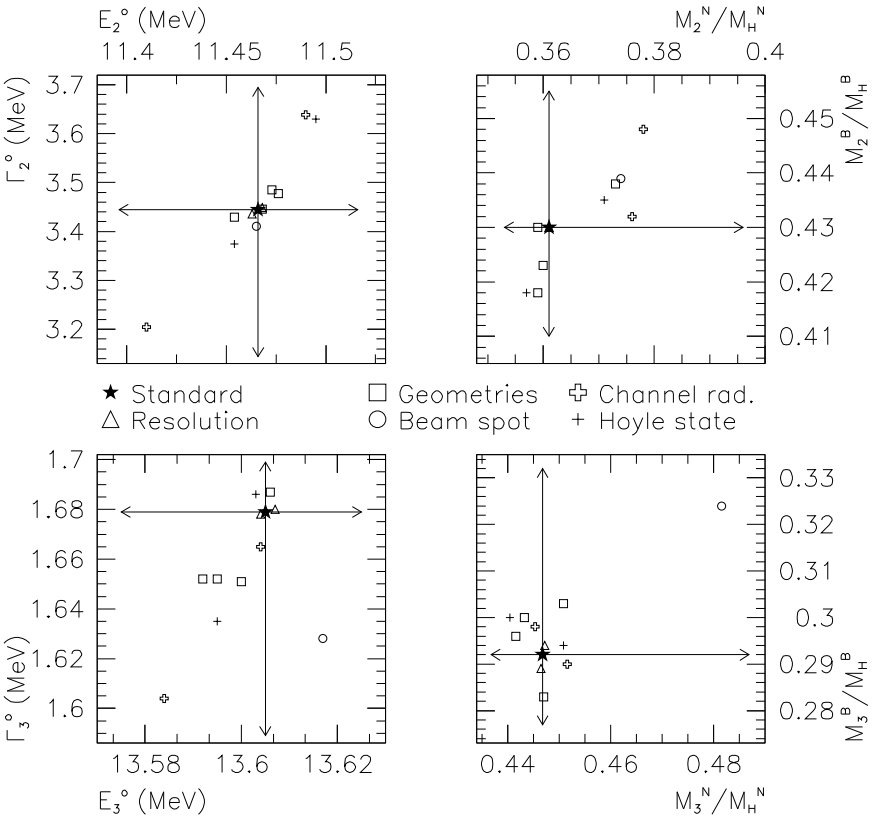

Figure 6.3.5: Systematic uncertainties from uncertainties in geometry, beam spot size, resolution, channel radius and Hoyle state parameters. Estimate of total systematic uncertainty is shown as bars on the standard parameters.

CHAPTER 7

The ^{8}Be excited state channel

As described in section 5.3.3, the breakups that do not proceed through the ^{8}Be ground state are referred to as breakups through the ^{8}Be excited state channel. Assigning this name to a breakup already indicates some knowledge of the breakup channel, namely that the breakup is sequential and proceeds through an intermediate ^{8}Be resonance. For the time being however it should be seen as nothing more than a name, since we cannot a priori claim to know that an excited state resonance of ^{8}Be is playing a role here, instead of a direct breakup to the free triple alpha continuum.[1] And as we will see in sections 7.3.3 and 7.4.3 we may even have a resonant ^{8}Be contribution here that isn't really an excited state of ^{8}Be.

7.1 Energy spectra

7.1.1 ^{12}C spectrum

In figures 7.1.1 and 7.1.2 we see the Fynbo plots for breakup through the ^{8}Be excited state channel for ^{12}N and ^{12}B data respectively. As indicated in figure 5.3.4 a cutoff for this was set at 200 keV in reconstructed ^{8}Be energy.

[1] A discussion on sequential versus direct decays in the context of two-proton deays can be found in Blank et al. (2003).

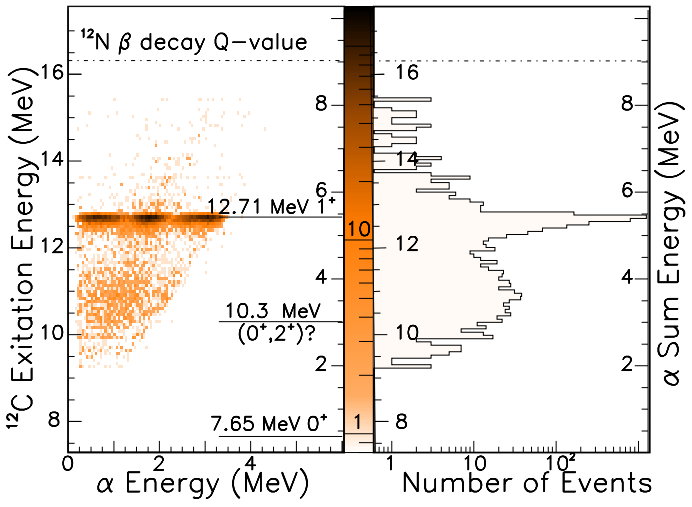

Figure 7.1.1: Fynbo plot of ^{12}N beta delayed triple alpha breakup through the ^{8}Be excited state channel, and projection onto sum energy axis.

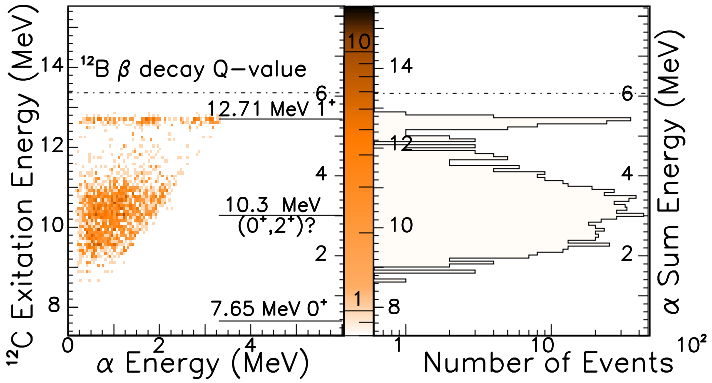

Figure 7.1.2: Equivalent to figure 7.1.1, but for ^{12}B beta delayed triple alpha breakup.

7.1.2 Phase space distributions

There has previously been published a thorough discussion of the breakup of the 12.7 MeV 1^+ state of ^{12}C (Fynbo et al., 2003). This showed that the breakup could in fact be successfully described as a resonant breakup through the 3 MeV 2^+ state of ^{8}Be if the intermediate state was properly described in a full symmetrized R-Matrix model. The direct breakup model (Korsheninnikov, 1990) could not reproduce the data. Keeping this in mind, we will try to describe these

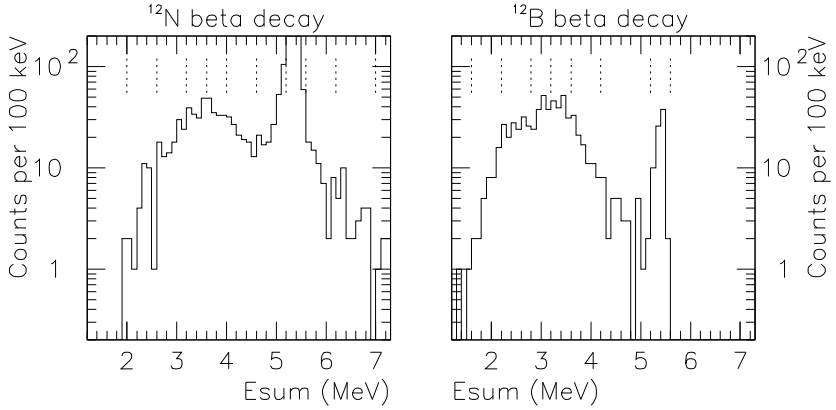

Figure 7.1.3: ^{12}N beta delayed triple alpha breakup through the ^{8}Be excited state channel. Binning for phase space projections are indicated.

breakups through an R-Matrix description of the intermediate ^{8}Be resonances, not only for the 12.7 MeV state but as well for the broad 0^+ and 2^+ states of ^{12}C.

The relevant observables to investigate here are observables describing which parts of three particle phase space dominate in the breakups. The energies of the individual alpha particles is one such observable. As seen in the Fynbo plots, these individual alpha energies are very different at different sum energies, so to describe the data quantitatively we divide the data into bins according to the sum energy as shown in figure 7.1.3. The binning has been chosen so that individual bins have similar number of events (around 100), except from the very abundant 12.7 MeV state in the ^{12}N decay data. In the following we will focus on the 5.4 MeV bin where the 12.7 MeV state dominates and—for the ^{12}N data—the 3.8 MeV and 5.9 MeV bins. The situation for the other bins and for the ^{12}B data is similar except we have no ^{12}B data in the upper energy region.

For the three mentioned bins, Dalitz plots are shown in figure 7.1.4. The plots are defined as described in section 4.2.2 except here only one sixth of the circular Dalitz plot is shown, since sorting the three alpha particles ensures $E_1 > E_2 > E_3$, thus confining all data to this part of the full Dalitz plot. Below the Dalitz plots the individual alpha energies are plotted, scaled according to the region between 0 and 1 with the maximal kinematically allowed alpha energy $\frac{2}{3}E_{sum}$. This scaled single alpha energy is denoted X_α.

The single alpha energy distributions directly reflects the Dalitz plot distributions as can be seen by comparing the upper and lower plots in figure 7.1.4. The 3.8 MeV bin shows a close to uniform distribution in the Dalitz plot which

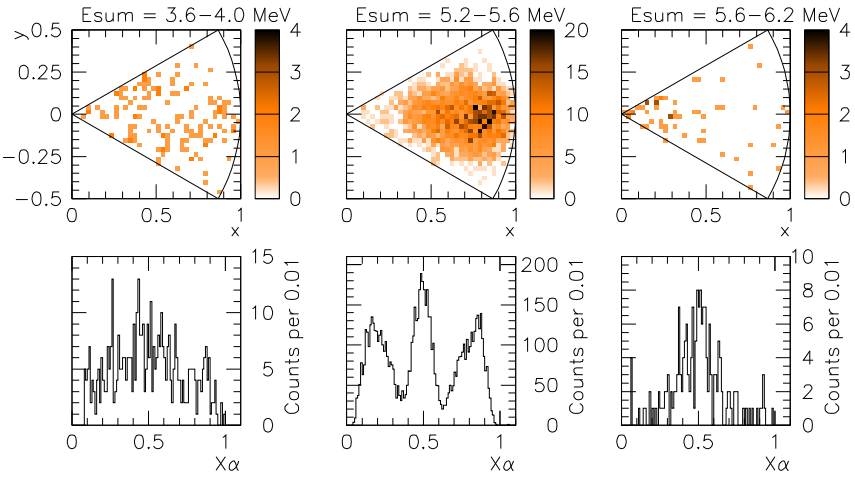

Figure 7.1.4: ^{12}N data, Dalitz plot and individual alpha energies. Sum energy binning according to figure 7.1.3.

is reflected in a very broad distribution in the single alpha plot, without any pronounced peak structure. At this energy the distribution is thus relatively close to the raw three particle phase space distribution. The 5.9 MeV bin on the other hand has a sharp peak close to the origin of the Dalitz plot, corresponding to events where the three alpha particles share the energy evenly. This is reflected in the sharp peak at $X_\alpha = 0.5$ corresponding to a single alpha energy of $\frac{1}{3}E_{sum}$ for all three alpha particles. The central plots containing the 5.4 MeV bin data is completely different from both of the others. Here we have again a pronounced peak structure but not at the Dalitz plot origin rather around $(0, \frac{3}{4})$. This again corresponds to $X_2 = 0.5$ since the vertical position gives the X_2 value as shown in figure 4.2.3. With a well defined value of X_2 the horizontal position defines the distance to the two upper sides of the equilateral triangle indicated in the figure i.e. the remaining two energies X_1 and X_3. With this position of the Dalitz plot peak X_1 is much bigger than X_3, giving rise to the three peak structure of the X_α plot for this sum energy bin.

7.2 Background estimate

In section 5.4.2 we saw an estimate of the energy distribution of the background. This, however, is not all that is to be said about the background. We should as well investigate the distribution of the background in three particle phase space.

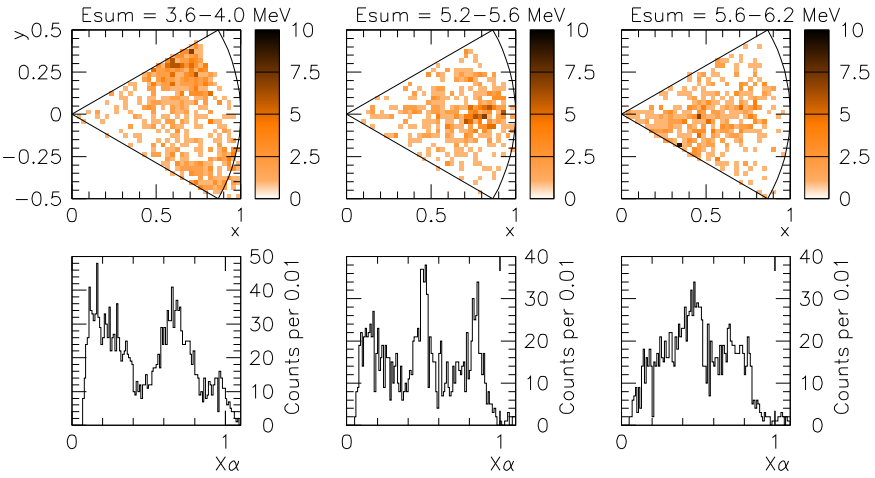

Figure 7.2.1: Event mixed data, Dalitz plot and individual alpha energies. Sum energy binning according to figure 7.1.3.

As in section 5.4.2 this is estimated using event mixing.

7.2.1 Phase space distribution from event mixing

Figure 7.2.1 contains the Dalitz plot three particle phase space distributions from triples mixed from two events. When comparing figure 7.1.4 and 7.2.1 it is clear that at neither of the three shown energies the background can be a dominant contributions to the data set. This fits well with the total background estimates in section 5.4.2. Here we saw a total background estimate of 100. With the energy distributions shown in figure 5.4.1 and 5.4.2 we get an estimate ranging from about 1.5 background counts per 100 keV sum energy in the 5.9 MeV region up to about 3 counts per 100 keV in the 3.8 MeV region, yielding an estimate of 10 background events for each of the three energy intervals shown in figure 7.1.4 and 7.2.1. Even with a background as different from the total data set as in the case of the 3.8 MeV in terms of Dalitz plot distributions and thereby X_α distributions a 10 count contribution is not in conflict with the data set distribution.

7.3 Simulated phase space distributions

Before investigating the breakup of broad 0^+ and 2^+ states in ^{12}C, we will take a look at the breakup of the 12.7 MeV 1^+ state of ^{12}C. With this we can verify the

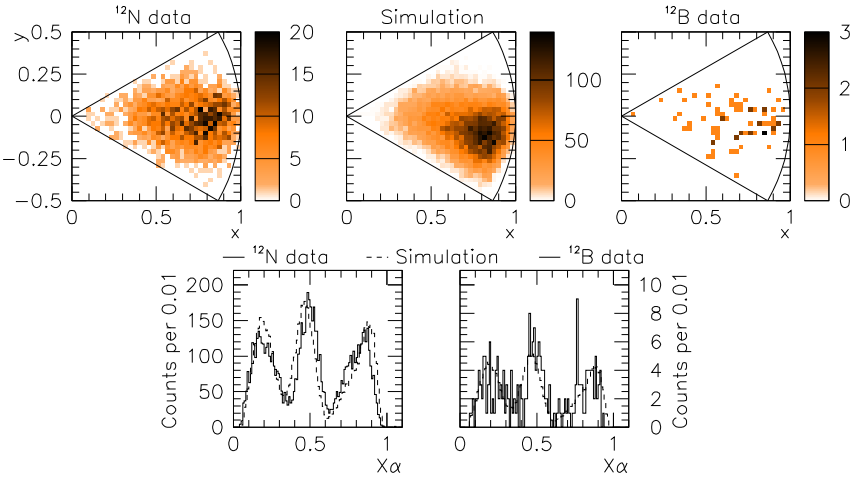

Figure 7.3.1: ^{12}C 1^+ state breakup through ^{8}Be 2^+ state. Upper row: Dalitz plot for ^{12}N and ^{12}B data along with R-Matrix simulated distribution. Below: Same data, single alpha energy scaled according to maximal alpha energy. Simulation scaled down to reproduce the area.

overall simulation method and identify the precision of the simulations in order to validate the following evaluation of the 0^+ and 2^+ state data.

7.3.1 The ^{12}C(1^+) breakup

The physical three particle phase space distribution for ^{12}C breakup through the ^{8}Be(2^+) excited state is found using the three particle distribution and the Von Neumann sampling method described in section 3.3.1. With the events distributed according to the physical distribution, each events is processed in the same way as was the case for the ^{8}Be ground state breakup (section 6.2) namely: First an analysis of how the detector setup would respond to the event and secondly by processing the detected event through the same data analysis as used for the experimental data. This analysis gave the effect of the individual cutoffs as shown in table 5.4.1.

For the ^{12}C(1^+) breakup, the R-Matrix weight calculation is straight forward, since the parity of the states in play requires the orbital angular momentum of the ^{8}Be(2^+) + α system to be even and conservation of the total spin of the system excludes any even angular momenta except 2. In figure 7.3.1 the result of such a simulation is shown. This simulation is performed for 10^6 physical events yielding in total 18407 detected triple coincidence events corresponding to

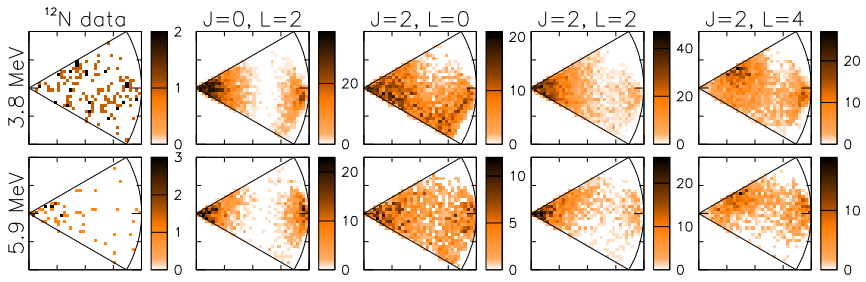

Figure 7.3.2: Dalitz plots for ^{12}N data in two different sum energy bins. Simulated distributions for breakup through ^{8}Be 2^+ state. Two different possible spins (J) of the ^{12}C state, all possible angular momenta (L) for the $^{8}\mathrm{Be}(2^+) + \alpha$ intermediate system.

an efficiency of 1.84%. When investigating the figure, it is clear that the overall properties are reproduced in the Dalitz plot as well as in the X_α plot. There is however a negative bias in the X_2 values of the simulation, corresponding to a lowering of the peak in the Dalitz plot. The grounds for this bias could not be identified, so what this says is that care should be taken when using the plots to discuss the possible breakup channels for broad ^{12}C 0^+ and 2^+ states in the following.

Note that since the distribution in three particle phase is peaked, the Von Neumann sampling used here is not the most efficient Monte-Carlo simulation method. It would be convenient to use an importance sampling focused on the peak of the distribution, this would be extra preferable since some of the breakup simulations in the following section are even more peaked. The distributions however depend on both decay channel and ^{12}C energy, so to make an importance sampling effective would require several different sampling methods, essentially one for each distribution. The gain from importance sampling was in this case not sufficient to justify the complications of it.

7.3.2 The $^{8}\mathrm{Be}(2^+)$ breakup channel

The phase space distributions for breakup of a ^{12}C 0^+ and 2^+ contribution at any given ^{12}C energy can be sampled in the same way as was done for the $^{12}\mathrm{C}(1^+)$ breakup. Here however more than one angular momentum value is possible if the ^{12}C state in question is a 2^+ state, namely 0, 2 and 4. Such simulations for $2 \cdot 10^5$ physical events are shown in figure 7.3.2 for all possible combinations of ^{12}C spin and angular momentum.

Before making a statistical comparison of the simulated Dalitz plots and the corresponding experimental data, we can get the overall picture from what we

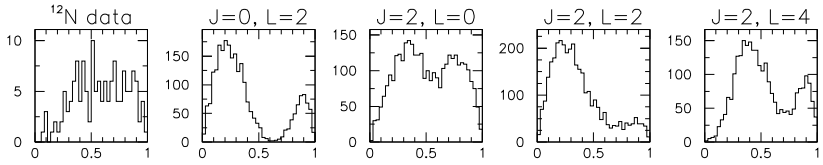

Figure 7.3.3: Dalitz plot projections on horizontal axis, 3.8 MeV sum energy. ^{12}N data and four simulations as in figure 7.3.2.

can see by eye. What we should look for in the comparison is not the overall scale of the distributions but in which parts of the Dalitz plots the intensity is located. That is we should understand the simulated distributions as approximations to the physical distributions from which the actual data has been drawn. With this we should describe which of the distributions are most likely to dominate the data distributions. Note that we cannot necessarily require all of the data to be described by one of the distributions and also that we expect a small contribution from the background, so the correspondence is not expected to be exact.

The most pronounced structure seen in the simulations is the fact that $L = 2$ simulations are strongly peaked at the origin of the Dalitz plot whereas the others—especially $L = 0$—show a distribution closer to a uniform distribution. This is very clear if we look at the projections on the horizontal axis as seen in figure 7.3.3. It is clear that neither of the $L = 2$ breakups can be a dominant contribution to the data. For the 5.9 MeV bin the situation is quite the opposite, and a strong intensity is seen near the origin of the data plot, pointing towards a significant $L = 2$ contribution. With this understanding of the overall picture, we are ready to proceed to a statistical analysis of the data.

The shown Dalitz plots are all 36×36 pixels. As noted in the preceding section however the precision of the simulations does not justify such a fine binning of the Dalitz plots. For this reason, the following comparison between data and simulations are done for a binning 6 times as rough yielding 36 pixels in total. Of these pixels 8 are outside the piece of the Dalitz plot obeying $E_1 > E_2 > E_3$ leaving 28 relevant pixels. The distribution predicted by the simulation is fitted to the data with one free parameter, a scale factor. Besides this contribution from the simulated distribution, a background component estimated from event mixing (figure 7.2.1) is added, scaled as in figure 5.4.2. The fitting method used here is exactly the same as described in section 6.3.2. Compared to the previous fits we have here a smaller number of bins and a two dimensional simulated distribution to describe the theoretically predicted content of each bin. The essentials of the Maximum Likelihood method however remains the same. In these fits, the most interesting parameter is actually the χ^2_λ minimum quantifying the goodness of the individual fits. This is shown for the individual fits in the first four columns of

$J_{^{12}\mathrm{C}}, J_{^{8}\mathrm{Be}}, L$	$0,2,2$	$2,2,0$	$2,2,2$	$2,2,4$	$0,0,0$	$2,0,2$
$\chi^2_\lambda(3.8\,\mathrm{MeV})$	98.6	60.2	92.3	34.1	35.1	46.5
$\chi^2_\lambda(5.9\,\mathrm{MeV})$	37.8	35.2	20.5	40.2	41.4	43.9

Table 7.3.1: Goodness-of-fit χ^2_λ for fits of simulated Dalitz plot distributions (figure 7.3.2 and 7.3.4) to data.

table 7.3.1. The overall trends identified by eye are confirmed by the fitting. The $L = 2$ fits to the 3.8 MeV region data are very poor. A bit surprising is the fact that the $J = 2, L = 4$ fit is better than the $J = 2, L = 0$ fit for the same region. When we looked at figure 7.3.3 it seemed as if it would be the opposite. This however is not a problem, since the projection removed all vertical information, leaving only some of the information in the original plot.[2] For the 5.9 MeV sum energy bin, the situation is almost the opposite. $J = 2, L = 2$ gives by far the best fit, though admittedly the $J = 2, L = 0$ distribution is not that bad. In general it is seen that the discrimination between the different distributions is best in the 3.8 MeV sum energy bin compared to the 5.9 MeV bin. This is primarily because of the lower amount of data in the latter of the two having 61 events compared to the 149 events in the 3.8 MeV bin.

7.3.3 Breakup through the ^{8}Be(0^+) ghost

Though with the analysis in the preceding it is very tempting, we should not stop here, since another channel actually exists. The ^{8}Be ground state is not only important around 92 keV above threshold. Just as was the case for the Hoyle state, the upper tail of the state is determined by the competition between the standard Breit-Wigner distribution cutting off the high energy region and the penetrability for the α–α breakup through the barrier increasing the width in the Breit-Wigner distribution drastically with energy. This is seen in figure 3.1.1 where the Breit-Wigner distribution for resonant α–α scattering through the ^{8}Be(0^+) ground state is shown. This blown up high energy tail of the ^{8}Be ground state distribution is what is called the ghost of the ^{8}Be ground state (see section 3.1).

With this "excited state" of ^{8}Be an analysis similar to that of the preceding sections can be made. Only here the ^{8}Be spin ($J_{^8\mathrm{Be}}$) is 0 requiring the ^{12}C spin to be identical to the orbital angular momentum of the intermediate ^{8}Be(0^+)+α system. The Dalitz plot for simulations corresponding to a ^{12}C spin ($J_{^{12}\mathrm{C}}$) of 0 and 2 are shown in figure 7.3.4. When comparing these simulations to the experimental data as was done for the ^{8}Be(2^+) state simulations, we get the results shown in table 7.3.1. From this—and actually from a simple comparison

[2] The same is in principle the case for the reduction from 36×36 pixels to 6×6 pixels. This reduction however seems to do a better job in keeping the information in the Dalitz plot. The effect of these reductions have not been analyzed in detail, but for a description of such an analysis see (Eadie et al., 1971).

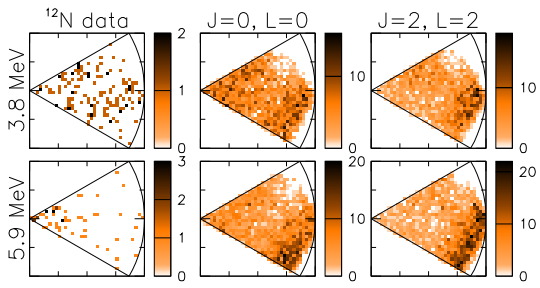

Figure 7.3.4: Dalitz plot for ^{12}N data along with simulated distributions for breakup through ghost of ^{8}Be 0^+ ground state. Angular momentum (L) equals ^{12}C state spin (J).

by eye as well—it is clear that they reproduce the data very well in the low energy region whereas for higher energies the correspondence is very poor. For the low energy region, the detected phase space distribution is reproduced just as well by the simulated $0, 0, 0$ $(J_{^{12}\mathrm{C}}, J_{^8\mathrm{Be}}, L)$ distribution as is the case for the $2, 2, 4$ distribution. We will return to the discussion of this breakup channel in section 7.4.3 where it will be shown how the energy distribution in ^{12}C corresponding to this breakup channel can be found directly from the information we already have on the ^{8}Be ground state channel.

7.3.4 Conclusions from Dalitz plot simulations

From the Dalitz plots and fits to data presented here, we must conclude that the high energy region (above the ^{12}C 1^+ state at 12.7 MeV) is dominated by the breakup of a ^{12}C 2^+ state through the 3 MeV 2^+ state of ^{8}Be. Besides this we may conclude that at these energies the breakup has predominately a d-wave ($L = 2$) in the intermediate $^8\mathrm{Be} + \alpha$ system.

For the low energy region the situation is a bit more complicated, since the $2, 2, 4$ and $0, 0, 0$ distributions reproduce the data equally well. There is however one very significant physical complication for the $2, 2, 4$ possibility, namely the angular momentum barrier. In itself, seeing a $2, 2, 4$ contribution at low energy is hard to exclude. However one would expect the $2, 2, 0$ and $2, 2, 2$ contributions (with $L = 0$ and $L = 2$) to overcome their angular momentum barriers at lower energies than is the case for the $2, 2, 4$ contribution (with $L = 4$). Since the $2, 2, 2$ contribution is seen to dominate at an energy of about 5.9 MeV above the threshold, the $2, 2, 4$ would be expected to come in at even higher energies. With this possibility excluded we must conclude that the low energy region is dominated by a ^{12}C 0^+ state breaking through the $^8\mathrm{Be}(0^+)$ ghost channel.

These two conclusions comply with the conclusions from the analysis of the breakup through the 92 keV ^{8}Be ground state channel (chapter 6). The resulting spin assignments from the analysis of these two channels can thereby be seen as independent tests of the ^{12}C state properties. Firstly because the data are statistically independent. Secondly because the analysis in the first case is built on an understanding of the shape of the ^{12}C spectrum whereas the second analysis focuses on the energy sharing between the three alpha particles. With these differences, a systematic error can hardly cause the same erroneous conclusion in both cases, which is exactly what characterizes independent measurements.

7.4 Energy spectrum calculations

The last remaining challenge regarding the ^{8}Be excited state channel is to describe the ^{12}C spectrum for this channel. This spectrum is determined by the beta feeding of the states and the widths for breakup through this channel. It is furthermore influenced by other channels, in particular the ^{8}Be ground state channel, through their effect on the level matrix $A_{\lambda\mu}$. The developed formalism describing breakup of broad states through such broad exit channels was described in section 3.4 and will not be repeated here in detail.

There are however a few things worth noting. The formalism uses a description of the distribution of relative energies similarly to what was done in section 7.3 for the Dalitz plot distributions. The main difference being the importance of the overall scale. This distribution is then integrated over all angles and over the ^{8}Be energy from 200 keV and upwards as in the data analysis cutoffs. This yields a ^{12}C spectrum with the overall scale factor taken from the analysis of the ^{8}Be ground state channel. The angular integration is performed as an integration over the direction of the first alpha and over the angle of the secondary breakup relative to that of the first alpha. This however causes one problem that has not yet been overcome: In the integration the two alphas constituting the intermediate ^{8}Be state are defined, in conflict with the idea of symmetrizing in the three alpha coordinates. For this reason, the following integrated spectra have not been symmetrized (sections 7.4.3 and 7.4.4).

7.4.1 Detection efficiencies

Before describing the spectra theoretically we must however be able to correct the measured spectra for detection efficiencies. These efficiencies are found in the same way as was done for the ^{8}Be ground state channel, namely through Monte-Carlo simulations. As described in section 7.3.1 the efficiency for detecting three alpha particles from the breakup of the ^{12}C(1^+) state 5.4 MeV above the threshold, was estimated to be 1.84%. In exactly the same manner, the efficiency must be simulated for all other possible state spins and breakup channels $(J_{^{12}\mathrm{C}}, J_{^8\mathrm{Be}}, L)$. This is because the triple alpha detection efficiency in general depends on the decay channel, as is especially clear when comparing the efficiency

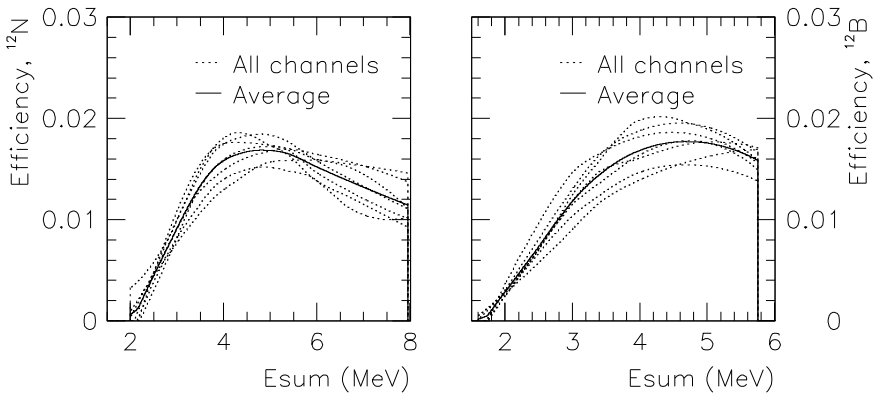

Figure 7.4.1: Simulated efficiencies, different ^{8}Be excited state channels.

corresponding to the breakup of the 12.7 MeV 1^+ state. Furthermore it should be calculated at all relevant energies. In practice the efficiencies are simulated for all center values for the bins illustrated in figure 7.1.3. After this the efficiencies and their different energy dependencies are found by interpolating between the simulated efficiencies. This is the most effective way of finding the energy dependencies, since the simulations are rather time-consuming. The energy dependence of all seven efficiencies $(0,2,2;\ 2,2,0;\ 2,2,2;\ 2,2,4;\ 0,0,0;\ 2,0,2;$ and $1,2,2)$ are plotted in figure 7.4.1. As can be seen, all efficiencies are within $\pm 20\%$ of the average of the seven which is shown as well. So unless details finer than 20% are needed, the average efficiency is perfectly acceptable as a common efficiency estimate.

7.4.2 Phase space and efficiency corrections

With such an understanding of the triple alpha coincidence detection efficiency, we can correct the measured ^{12}N and ^{12}B decay spectra for detection efficiencies as well as for the f-factor from the beta decay phase space, allowing us to compare spectra for the two decays. These corrected spectra are seen in figure 7.4.2 for the f-factor corrected spectrum and in figure 7.4.3 where both corrections are applied. The ^{12}N and ^{12}B spectra have been scaled relative to each other by the same ratio as used for the ^{8}Be ground state channel (figure 6.3.1 and 6.3.2) making use of the fact that the scale factor is determined solely by the total number of decaying ^{12}N and ^{12}B nuclei. With this scaling it is once again clear that the physics governing the two decays are very similar.

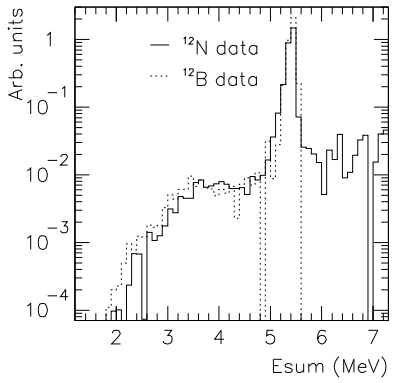

Figure 7.4.2: ^{12}N and ^{12}B spectra for breakup through the ^{8}Be excited state channel corrected for β-phase space f-factor.

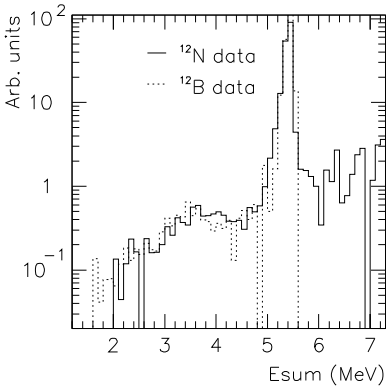

Figure 7.4.3: Same as figure 7.4.2 but corrected for the average efficiency of figure 7.4.1 in addition to the β-phase space correction.

7.4.3 Direct prediction for breakup through the ^{8}Be(0^{+}) ghost

Since the ^{8}Be(0^{+}) ghost channel and the ^{8}Be ground state channel are exactly the same breakup channel from a quantum mechanical perspective, we can use the results from chapter 6 to make a direct prediction of the ^{12}C spectrum for breakup through the ghost channel. The predicted spectrum is seen in the right frame of figure 7.4.4 where it is compared to the experimental ^{12}N decay data. Note that in this prediction there are no free parameters, not even the overall scale. To test the validity of the integration, the integration is performed over the narrow ^{8}Be ground state peak 92 keV above the threshold, giving the spectrum seen in the left frame of the figure. This clearly shows the validity of the integration method.

As seen in figure 7.4.4 the predicted spectrum reproduces the shape and intensity of the measured spectrum very well in the 2–3 MeV region. Above this value, the correspondence is only within a factor of three or so. The decay of the 2^{+} state at higher energies does not reproduce the measured high energy range, well in agreement with the Dalitz plot conclusions claiming this energy region to be dominated by a 2^{+} state decaying through the excited 2^{+} state of ^{8}Be.

7.4.4 Possible ^{12}C spectra for the ^{8}Be(2^{+}) channel

In addition to the ^{8}Be(0^{+}) ghost channel, we can similarly calculate spectra for breakups through the ^{8}Be(2^{+}) excited state at 3 MeV. Such a calculation however

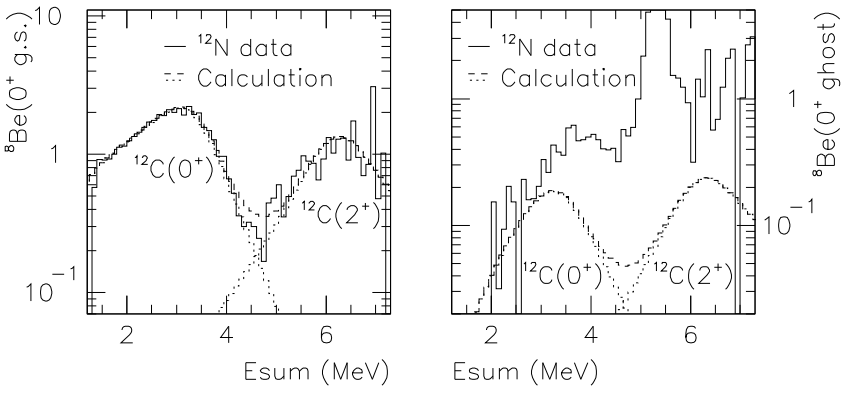

Figure 7.4.4: ^{12}C breakup through ^{8}Be ghost predicted from breakup through ^{8}Be ground state. Compared to ^{12}N decay data. Both spectra are corrected for beta phase space and detection efficiency.

has a lot of free parameters compared to the ghost channel calculations. This is because we have up to three new decay channels $L = 0, 2, 4$ with their respective decay widths. Or in the R-Matrix formalism: The reduced widths $\gamma^{J_C}_{\lambda J_{Be} L}$ from the level λ of spin J_C by a decay with angular momentum L through the ^{8}Be level of spin J_{Be}. In this case $J_{Be} = 2$ and since we saw in table 7.3.1 that the $J_C = 0$, $J_{Be} = 2$, $L = 2$ was unlikely to contribute significantly, we focus on the $J_C = 2$ levels. For simplicity the $L = 4$ contribution is excluded as well, leaving us with $\gamma^2_{\lambda 20}$ and $\gamma^2_{\lambda 22}$ for at least one, possibly more levels λ of ^{12}C.

With a single high energy level at 13.6 MeV above the ground state of ^{12}C and values of $\gamma^2_{\lambda 20}$ and $\gamma^2_{\lambda 22}$ similar to that of $\gamma^2_{\lambda 02}$ as found in chapter 6, we get the calculated spectrum shown as the dashed line in figure 7.4.5. In contrast to the ^{8}Be ghost channel calculation, the scale for this calculation relative to that of the ^{8}Be ground state is quite arbitrary. This ratio is in essence defined by the ratio between the decay widths of the two channels and may be seen as a free parameter. As seen in the figure, a level at such a high energy has no way of producing a significant contribution in the low energy range, which is hardly surprising. We will therefore consider the possibility of a second 2^+ level at a lower energy. Such a state would necessarily interfere with the higher lying 2^+ state.

If the low energy level should have a low energy tail as pronounced as possible, the interference between the two levels should enhance the low energy tail thus giving a destructive interference in the intermediate region. Such calculations are shown as the dotted and dot-dashed lines in the figure for a low energy level

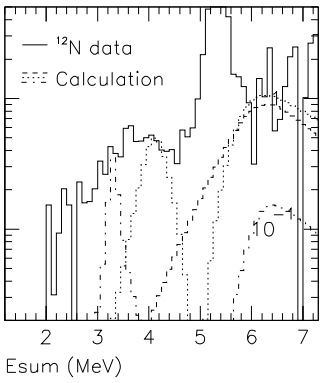

Figure 7.4.5: Calculated spectra for 2^+ states at different energies with breakup through ^{8}Be(2^+) state channel.

just above 3 MeV and 4 MeV in three alpha sum energy corresponding to states around 10.5 MeV and 11.5 MeV in ^{12}C. As seen, the state is very narrow if placed at an energy as low as 10.5 MeV, and it is clearly seen that a breakup through the ^{8}Be(2^+) state cannot reproduce the low energy part of the spectrum.

7.4.5 Conclusions from energy spectrum calculations

With these spectra in hand, we can conclude: Firstly that the ^{8}Be(0^+) ghost channel is very important and as seen from figure 7.4.4 it receives about 10% of the total ^{12}C 0^+ strength in the region about 3 MeV above the triple alpha threshold, and dominates the breakups through high energies of ^{8}Be completely at this ^{12}C energy and below. It is thus essential for understanding the ^{8}Be excited state breakup channel. Secondly we may conclude that this breakup channel seems to be reasonably well described by an R-Matrix formalism without symmetrization. Thirdly, for the energy range around 4 MeV above threshold, the situation is more ambiguous. In this energy range a ^{12}C 2^+ state decaying through the ^{8}Be(2^+) channel would easily have a width of half an MeV or more, enabling the state to contribute significantly to the broad measured spectrum without standing out as a narrow peak in the spectrum. At the same time the breakup through the ^{8}Be ghost is apparently not sufficient to describe the spectrum. We should however hesitate in excluding the ghost channel at these energies because of the complications arising from the symmetrization when determining the spectrum as predicted from the R-Matrix model.

As noted in section 3.4.1 the symmetrization should be done by interchanging

the three alphas in equation 3.4.1 and summing the three contributions each arising from a different pair of alphas assigned to the ^{8}Be intermediate state. If more than one of these three contributions are significant, they are added as complex numbers before calculating the norm squared. This may give up to a factor of three in the sum, if they have the same size and add constructively. Taking the norm squared makes this up to a factor of 9. Outside the norm squared however the symmetrization requires a factor of $\frac{1}{3}$, yielding in total up to a factor of three increase in the spectrum. The symmetrization may thus potentially cause the ghost channel to reproduce the channel at higher energies than the 3 MeV seen in figure 7.4.4. The question is just: Is the ghost channel capable of producing such a symmetrization interference? Unfortunately the answer is yes, which can be seen from a short argument involving only the energies of the states in play. We can as an example look at a 3.8 MeV breakup such as the one simulated in section 7.3.3. In figure 3.1.1 we see that the ^{8}Be(0^+) ghost has a very broad distribution over the 0–3 MeV energy range, and it has thus a significant contribution around for example 1.7 MeV. A breakup through this ^{8}Be energy will leave 2.1 MeV for the initial breakup yielding an energy of 1.4 MeV for the first emitted alpha. This is very close to the energies of the two remaining alphas (1.2 MeV) if they share the energy evenly, thus making the two other choices for the first emitted alpha equally important. Such events are the ones close to the origin of the upper central Dalitz plot of figure 7.3.4. For these events at least, the symmetrization may therefore be very important, but because of the broad distribution in ^{8}Be, a more uneven sharing of the energy between the three alphas may as well give rise to significant contributions from more than one of the three different choices of the first emitted alpha particle. A similar argument can be used for the breakup of the high energy (approximately 6 MeV triple alpha energy) 2^+ state of ^{12}C through the 3 MeV ^{8}Be(2^+) state, making it likely that as well for this breakup, the symmetrization will be important for a proper description of the spectrum.

The breakup on the other hand of the high energy 2^+ state of ^{12}C through the ghost is not likely to be influenced that heavily by the symmetrization. This is because seen from a total triple alpha energy of 6 MeV, the ghost is a rather narrow state and it has such a low energy that the energy of the first emitted alpha particle is rather well defined and much higher in energy than the remaining two alpha energies.

CHAPTER 8

Branching ratios

There are two important ways of describing how the ^{12}N and ^{12}B decays populate the individual states in ^{12}C. Firstly the branching ratios and secondly the B_{GT} values. Though it can be done it is however difficult to extract the B_{GT} values, when two broad levels have a significant interference as described in section 3.2.2. As described there, the energy dependence of the beta phase space factor and the decay width must be corrected for. On top of that the interference must be unraveled. Because of this, the derivation of B_{GT} values builds on the interpretation of the spectrum and is in this way at least to some degree model dependent.

In the following the branching ratios to different energy regions will therefore be described first. Both through a completely model-independent summing of the spectrum and through an integration of the fit from chapter 6 corrected for decays through the ^{8}Be excited state channel. This integration will allow us to extrapolate the branching ratios down below the measured energies, giving even the branching ratio to the Hoyle state. Furthermore these branching ratios have been normalized using the well studied decay to the 4.44 MeV state in ^{12}C. After this the matrix elements, B_{GT} values and ft values corresponding to each level will be identified. Summarizing these results will be compared to the previously available data.

12.7 MeV state	Energy (MeV)	Counts	Uncert.	Counts/MeV
^{12}N decay peak	[5.0:5.6]	2726	52	
Background	[4.5:5.0]	96		192
Background	[5.6:6.0]	52		130
Backgr. estimate	[5.0:5.6]	96	20	160
^{12}N detected	12.7 MeV	2630	56	
Decays in total	12.7 MeV	$\mathbf{1.46 \cdot 10^5}$	$\mathbf{0.14 \cdot 10^5}$	
^{12}B decay peak	[5.0:5.7]	79	9	
Background	[4.7:5.0]	8		27
Background	[5.7:6.0]	0		0
Backgr. estimate	[5.0:5.7]	9	7	13
^{12}B detected	12.7 MeV	70	11	
Decays in total	12.7 MeV	$\mathbf{3.9 \cdot 10^3}$	$\mathbf{0.7 \cdot 10^3}$	

Table 8.1.1: Number of triple alpha events detected in the ^{12}N and ^{12}B decays populating the 12.7 MeV state of ^{12}C, and total number of nuclei corrected for detection efficiency.

8.1 Model independent relative branching ratios

The measured ^{12}C spectra yield a direct information on the branching ratios for the two decays to the different energy regions, and thereby the branching ratios to the individual states. Since we have no absolute normalization of these spectra, it must be noted that only relative branching ratios are measured. The branching ratios of interest are to the 0^+ strength in the 10.3 MeV energy region corresponding to a triple alpha energy of about 3 MeV; to the 2^+ strength in the 13 MeV region corresponding to triple alpha energy of about 7 MeV; and to the 12.7 MeV 1^+ state 5.4 MeV above the triple alpha threshold.

From the ^{12}C spectra (figure 7.1.3) for breakups through the ^{8}Be excited state channel, the feeding to the 12.7 MeV state can easily be identified. The estimated number of counts for this beta decay channel is listed in table 8.1.1. Along with the detected number of counts in the peak, the estimated background is shown as well. The background is estimated from the number of counts in the surrounding region as indicated. The stated uncertainty of the total number of counts is the statistical uncertainty, whereas the background uncertainty is a reasonable upper limit estimated from the difference between the two surrounding intervals.

With efficiencies of 1.84(18)% and 1.86(19)% for the ^{12}N and ^{12}B data respectively, this corresponds to a total of $1.43(14) \cdot 10^5$ and $3.8(7) \cdot 10^3$ produced nuclei in the 12.7 MeV state of ^{12}C for the two decays respectively. The 12.7 MeV state however does not decay entirely to the triple alpha continuum states. The total width of the state is 18.1(28) eV of which 0.40(5) eV is the gamma decay width to the two bound states of ^{12}C corresponding to a 2.2% gamma decay branch (Ajzenberg-Selove, 1990). This branch is missing in this measurement

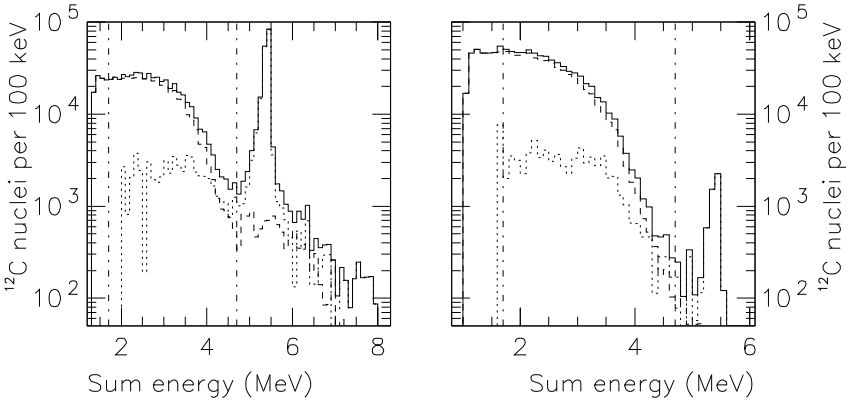

Figure 8.1.1: Spectra for ^{12}N and ^{12}B decays, detection efficiency corrected. ^{8}Be ground state channel (dashed); ^{8}Be excited state channel (dotted); and sum of the two (solid) are plotted. The definition of "the 10.3 MeV region" is indicated.

and it must therefore be corrected for,[1] yielding the results shown in table 8.1.1. An uncertainty of about 10% for the efficiencies is reasonable even though the beam spot size uncertainty shown in figure 6.2.6 shows a dependence of the efficiency of up to 20%, since what we need here is really the relative efficiency when comparing different energies or different breakup channels. If the absolute number of decays is needed, a additional systematic uncertainty of 15% should be included.

For the feedings to the states different from the 12.7 MeV state, the situation is a bit more complicated, since they are broad. If we remember the efficiency and beta phase space corrected spectra shown in figure 6.3.2 however, we see that a reasonable distinction between high and low energy contributions could be set to 4.7 MeV in sum energy corresponding to a ^{12}C energy of 12 MeV. Because of the limited statistics in the low energy range, we must choose a low energy cutoff for the lower energy region as well. This may conveniently be set to 1.7 MeV, corresponding to a ^{12}C energy of 9 MeV. The maximum of the upper region is only defined by the Q value of the beta decay. The feedings of these regions must be found taking the energy dependent detection efficiency into account, as shown in figure 8.1.1. The spectrum integrals as used for branching ratio estimation are shown table 8.1.2. For the low energy range the uncertainties are dominated by the 10% uncertainty in efficiency, whereas for the upper energy

[1] Though this is smaller than the estimated uncertainty we should not neglect it, since it is an expected systematic bias of our measurement.

	0^+,2^+ states	Energy (MeV)	Nuclei	Uncert.
^{12}N	(gs)	[1.7:4.7]	$5.32 \cdot 10^5$	10%
	(ex) estimate	[1.7:2.0]	$0.06 \cdot 10^5$	$0.03 \cdot 10^5$
	(ex)	[2.0:4.7]	$0.58 \cdot 10^5$	10%
^{12}N	10.3 MeV total	[1.7:4.7]	$\mathbf{6.0 \cdot 10^5}$	$\mathbf{0.6 \cdot 10^5}$
^{12}N	(gs)	[4.7:6.0]	$0.79 \cdot 10^4$	10%
	(gs)	[6.0:7.0]	$0.27 \cdot 10^4$	10%
	(ex)	[6.0:7.0]	$0.28 \cdot 10^4$	10%
	(ex)	[7.0:8.0]	$0.15 \cdot 10^4$	10%
^{12}N	13.6 MeV min	[4.7:8.0]	$1.3 \cdot 10^4$	
^{12}N	13.6 MeV max	[4.7:8.0]	$2.3 \cdot 10^4$	
^{12}N	13.6 MeV total	[4.7:8.0]	$\mathbf{1.8 \cdot 10^4}$	$\mathbf{0.4 \cdot 10^4}$
^{12}B	(gs)	[1.7:4.7]	$6.03 \cdot 10^5$	10%
	(ex)	[1.7:4.7]	$0.69 \cdot 10^5$	10%
^{12}B	10.3 MeV total	[1.7:4.7]	$\mathbf{6.7 \cdot 10^5}$	$\mathbf{0.7 \cdot 10^5}$
^{12}B	(gs)	[4.7:6.1]	$0.34 \cdot 10^3$	$0.15 \cdot 10^3$
	(ex) min	[4.7:6.1]	$0.10 \cdot 10^3$	
	(ex) max	[4.7:6.1]	$1.30 \cdot 10^3$	
^{12}B	13.6 MeV min	[4.7:6.1]	$0.3 \cdot 10^3$	
^{12}B	13.6 MeV max	[4.7:6.1]	$1.7 \cdot 10^3$	
^{12}B	13.6 MeV total	[4.7:6.1]	$\mathbf{1.0 \cdot 10^3}$	$\mathbf{0.4 \cdot 10^3}$

Table 8.1.2: Estimates of produced nuclei for the ^{12}N and ^{12}B decays in different energy ranges of ^{12}C. Both ^{8}Be ground state channel (gs) and ^{8}Be excited state channel (ex).

range, the uncertainties from subtracting the 12.7 MeV state contribution are substantial. The uncertainty on the total ^{12}N feeding to the upper energy region is thus found from estimated minimum and maximum bounds of $1.3 \cdot 10^4$ and $2.3 \cdot 10^4$. The lower bound is found from the assumption that at least the counts up to 7 MeV where the ground state channel is no longer present are real decay events, whereas the upper bound is found under the assumption that all the measured events are real events and furthermore that the excited state channel for the broad states contribute as much as the ground state channel in the region where they are overlaid by the peak of the 12.7 MeV state. These bounds yield a standard deviation of $0.3 \cdot 10^4$.[2] In addition to this, the efficiency uncertainty is taken into account. The estimation of the uncertainty for the upper energy region of the ^{12}B decay is made in a similar manner, though here the total number of counts is so small that the total is almost consistent with zero, so the given value should mainly be seen as an upper bound. Furthermore, the events that are unquestionable are all close to 4.7 MeV, so had the division between the ranges

[2] With the worst case assumption of a uniform uncertainty distribution within these bounds, the standard deviation is $\sqrt{12}$ of the total width as described e.g. by Barlow (1989).

^{12}N	^{12}C	^{12}B
BR/BR$_{12.7}$	Energy (MeV)	BR/BR$_{12.7}$
4.1(5)	10.3	171(37)
0.12(3)	13.6	0.28(13)

Table 8.1.3: Branching ratios relative to those of the 12.7 MeV 1^+ state in ^{12}C. Two different energy regions: 10.3 MeV and 13.6 MeV referring to the 0^+ and 2^+ strength in the intervals [1.7:4.7] and [4.7:8.0] MeV respectively in total alpha energy.

been placed just a bit higher, the ^{12}B branching to this region would definitely have been consistent with zero.

With the number of nuclei in different energy regions under control, we can give a completely model independent estimate of the relative branching ratios of the three parts of the ^{12}C spectrum. In table 8.1.3 the relative branchings are therefore summarized.

8.2 Relative branching ratios near the threshold

As noted in section 3.2.2 we can extrapolate the branching ratios down below our experimental low energy cutoff, since the fitted three level R-Matrix model describes the spectrum of both the 10.3 MeV region as well as the Hoyle state peak. As seen in figure 8.2.1 the total spectrum has a minimum at 0.46 MeV corresponding to 7.73 MeV in ^{12}C. This is where the Hoyle state ghost begins. The most useful definition of branching ratio regions is therefore to separate the two at exactly this energy. With this we can then calculate the integrals, and thereby estimate how many ^{12}C nuclei were produced in the individual regions. These estimates are given in table 8.2.1 corrected for the breakup through the ^{8}Be excited state channel as in table 8.1.2. By normalizing to the 12.7 MeV state (table 8.1.1) we get the relative branching ratios. The uncertainty of these are dominated by the 10% uncertainty in detection efficiency except for the ^{12}B decay where the uncertainty in the population of the 12.7 MeV state is higher. For the 13.6 MeV state similar integrated relative branching ratios can be found. This yields 0.070 and 0.055 for the ^{12}N and ^{12}B decays respectively, which should be multiplied by about a factor of two to take into account the fact that for this state about half of the breakup is through the ^{8}Be 2^+ state. These values are consistent with those given in table 8.1.3, but is not expected to be more accurate.

Though these are the best estimates of the branching ratios to the Hoyle state and the 10.3 MeV energy region, it must be emphasized that they are to some degree model dependent. For the branching to the Hoyle state peak it is 100% extrapolated, whereas for the 10.3 MeV strength only the difference between the

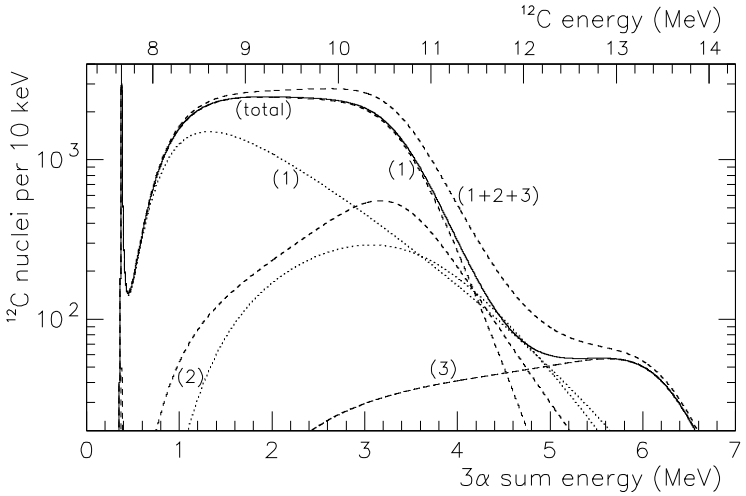

Figure 8.2.1: Three level R-Matrix fit to ^{8}Be ground state data. 0^+ Hoyle state with its ghost (1); 11.5 MeV 0^+ state (2); and 13.6 MeV 2^+ state (3). Dotted lines are the individual states in the single level approximation; dashed lines are the individual state contributions as described in equation 3.2.15 and the sum of all three; whereas the solid line is the total intensity including the full interference (equation 3.2.1).

^{12}N		^{12}C	^{12}B	
$BR/BR_{12.7}$	Populating decays	Energy (MeV)	Populating decays	$BR/BR_{12.7}$
38(6)	$5.6(6)\cdot10^6$	7.65	$1.62(17)\cdot10^7$	$4.2(9)\cdot10^3$
4.7(7)	$6.9(6)\cdot10^5$	10.3	$1.11(12)\cdot10^6$	$2.8(6)\cdot10^2$

Table 8.2.1: Estimated number of ^{12}C nuclei produced in low energy intervals: 7.65 MeV Hoyle state peak and 10.3 MeV region respectively, where the latter covers the [0.46:4.7] MeV interval. Branching ratios are given relative to those of the 12.7 MeV state.

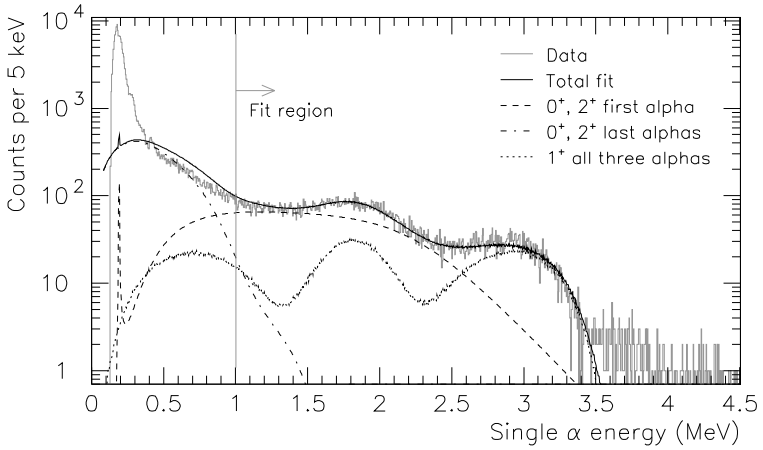

Figure 8.3.1: Single alpha energy, data and three component fit for region above 1 MeV as indicated (S. G. Pedersen, private communication).

values in tables 8.1.3 and 8.2.1 is model dependent.

8.3 Relative branching ratios from single alpha spectra

In addition to the analysis of triple alpha coincidence events presented in the preceding, the single alpha spectrum has been analyzed as well.[3] This analysis is in essence the same as the one previously performed by Schwalm & Povh (1966). The difference being our much improved statistics and a better theoretical understanding of the spectrum. Since the new analysis takes the interference between the Hoyle state ghost and the higher lying 0^+ state into account, the shape of the 0^+ contribution to the single alpha spectrum is much better understood yielding a more correct separation between this and the contribution from the 12.7 MeV 1^+ state as showed in figure 8.3.1. The resulting relative branching ratios are shown along with those from the triple coincidence analysis in table 8.3.1.

When comparing the branching ratios from the analysis of single alpha spectra and the triple coincidence spectra the two can be seen as independent measurements of the branching ratios to the degree that the two analysis are decoupled.

[3]For the data analysis and results presented in this and the following section all credit should be given to Solveig G. Pedersen.

^{12}N				^{12}B		
Comb.	Triple alpha	Single alpha	Energy (MeV)	Single alpha	Triple alpha	Comb.
43(6)	38(6)	53(9)	7.65	$5.5(11)\cdot10^3$	$4.2(9)\cdot10^3$	$4.7(9)\cdot10^3$
5.1(6)	4.7(7)	6.2(11)	10.3	$3.5(7)\cdot10^2$	$2.8(6)\cdot10^2$	$3.1(5)\cdot10^2$
1.	1.	1.	12.7	1.	1.	1.
0.12(3)	0.12(3)*	0.12(6)†	13.6	1.1(10)†	0.28(13)*	0.28(13)

Table 8.3.1: Relative branching ratio recommendations for the decays of ^{12}N and ^{12}B to the triple alpha continuum. For the 0^+ strengths (7.65 MeV and 10.3 MeV) the energy intervals are defined as in table 8.2.1. $*$ For the 2^+ strength (13.6 MeV) the energy interval is defined in table 8.1.3. † Here found from an integration of the fitted 2^+ contribution over the entire energy range. Combined values are found as described in text.

This is because the two data sets are to a high degree statistically independent. In addition to this the main systematic uncertainty for the triple coincidence data analysis, the coincidence detection efficiency, does not come into play for the single alpha energy spectra. This makes the low energy cutoffs and the trigger levels the only common feature in the two analysis. Furthermore, effects from low energy cutoffs and trigger levels are avoided in the single alpha analysis by excluding the low energy region.

When comparing, it is evident that the branching ratios from the two methods are consistent. For the Hoyle state and the 10.3 MeV energy region the values from triple coincidence (T) and single alpha (S) spectra are combined with relative weights according to their uncertainty (S) (see e.g. Barlow, 1989):

$$\mathrm{BR} = \frac{\mathrm{BR}_T {S_T}^{-2} + \mathrm{BR}_S {S_S}^{-2}}{{S_T}^{-2} + {S_S}^{-2}}.$$

For the 10.3 MeV region the uncertainty is similarly found through

$$S^{-2} = {S_T}^{-2} + {S_S}^{-2},$$

which is reasonable since the analysis methods are independent. This however is not the case for the Hoyle state, since its contribution is extrapolated from the R-Matrix description of the 10.3 MeV region. The single and triple alpha estimates are therefore influenced by the same systematic uncertainties, and a realistic uncertainty is therefore the smallest of the two uncertainties. For the high energy region, the triple coincidence estimate is given.

8.4 Normalizing to the 4.44 MeV state

Since the detector setup included a germanium detector in addition to the silicon detectors, it is possible to detect the gammas emitted when the bound 4.44 MeV

^{12}N			^{12}B	
Literature value (%)	BR(%) Igisol	Energy (MeV)	BR(%) Igisol	Literature value (%)
94.55(60)	?	g.s.	?	97.22(30)
1.898(32)	?	4.44	?	1.182(19)†
2.7(4)	5.2(8)	7.65	1.66(25)	1.5(3)
0.46(15)	0.62(7)	10.3	0.109(10)	0.08(2)
0.31(12)	0.121(15)	12.7	$3.5(7)\cdot10^{-4}$	?
?	0.015(5)	13.6	$1.0(5)\cdot10^{-4}$	?
0.0044(15)	?	15.1	–	–

Table 8.5.1: Absolute branching ratio recommendations. Comparison with (Ajzenberg-Selove, 1990) where possible. For † an alternative value of 1.283(40) is given.

2^+ state in ^{12}C is populated. With this detection we can use the known branching ratio to this state to normalize the measured relative branching ratios. This analysis yields an absolute value of the branching ratio to the 0^+ strength in the 10.3 MeV region of 0.618(73)% for ^{12}N and 0.1092(97)% for ^{12}B (S. G. Pedersen). For ^{12}B the value of course depends on which branching ratio for the 4.44 MeV state is used. The above value is derived using $BR(4.44) = 1.182\%$ whereas for $BR(4.44) = 1.283\%$ the 10.3 MeV branching ratio is scaled correspondingly.

8.5 Recommended branching ratios

With the absolute value of the branching ratios to the 10.3 MeV region in place (section 8.4), the absolute values of the remaining branching ratios can be found from the relative values. These new recommendations for the branching ratios are presented in table 8.5.1, where they are compared to literature values. The values for the ^{12}B decay are under the assumption that $BR(4.44) = 1.182\%$, so if $BR(4.44) = 1.283\%$ holds true instead, the values in the table must be scaled by a factor of 1.283/1.182. For the ^{12}B decay, the results are consistent with the literature values whereas for the ^{12}N decay, the values for the Hoyle state and for the 12.7 MeV state differ significantly. With two independent measurements both showing a significant deviation in the 10.3 MeV to 12.7 MeV ratio, the branching ratios presented here however seem sufficiently well founded.

8.6 B_{GT} values for individual levels

With a narrow state such as the 12.7 MeV state, the B_{GT} values are easily calculated from equation 3.2.8, stating that

$$B_{GT} = \frac{g_V^2}{g_A^2}\frac{B}{f_\beta t_{1/2;\lambda}}.$$

The absolute branching ratios to this state were found in the preceding section 8.5.1 and the half lives of ^{12}N and ^{12}B are known to be 11.000(16) ms and 20.20(2) ms respectively (Ajzenberg-Selove, 1990). The partial half lives of the two decays to the 12.7 MeV state are therefore found from $t_{1/2;12.7} = t_{1/2}/\mathrm{BR}_{12.7}$ to be 9.1(11) s and $5.8(11)\cdot 10^3$ s respectively. Besides this, the beta phase space factors are calculated from (Wilkinson & Macefield, 1974) to be 924 and 1.059 for ^{12}N and ^{12}B decays respectively. With this the B_{GT} values for the two decays are found to be 0.456(57) and 0.63(13) respectively.

For the decays to the 7.65 MeV Hoyle state peak, the f_β factor can be found as for the 12.7 MeV state but in this case it is much larger, namely $5.40\cdot 10^4$ and $1.007\cdot 10^4$ for the ^{12}N and ^{12}B decays respectively. With this and the relative beta decay branching ratios as seen in table 8.3.1, we can calculate the relative B_{GT} values to be 0.65(11) and 0.46(10) for the two decays respectively from:

$$\frac{B_{GT;7.65}}{B_{GT;12.7}} = \frac{f_{\beta;12.7}\, t_{1/2;12.7}}{f_{\beta;7.65}\, t_{1/2;7.65}} = \frac{f_{\beta;12.7}}{f_{\beta;7.65}}\frac{\mathrm{BR}_{7.65}}{\mathrm{BR}_{12.7}}. \tag{8.6.1}$$

This way of calculating the B_{GT} values is what has traditionally been done. It does however not really do justice to the Hoyle state, since it ignores the Hoyle state ghost and therefore does not take into account the entire beta strength to the Hoyle state. To take this threshold effect into account I will use the broad state formalism introduced in section 3.2.2 (Barker & Warburton, 1988). To emphasize this difference, the entire Hoyle state decay branch will in the following be denoted h instead of 7.65.

$$\frac{B_{GT;h}}{B_{GT;12.7}} = \frac{f_{\beta;12.7}\, t_{1/2;12.7}}{f_{\beta;h}\, t_{1/2;h}} = \frac{f_{\beta;12.7}}{\frac{I_h}{J_h}}\frac{\mathrm{BR}_h}{\mathrm{BR}_{12.7}} \tag{8.6.2}$$

Where I_h and J_h are defined for the 0^+ Hoyle state ($\lambda = 1$) from equations 3.2.17 and 3.2.18. In case of the fitted function, the decay probability is not scaled to yield an integral of $\ln 2/t_{1/2}$ but is scaled to fit the measured spectrum. With this scaling of the front factor C^2, the integral over any energy region is 1% of the total number of ^{12}C nuclei populated in the region, since the used energy unit is 1 MeV and bin width is 1% of this, namely 10 keV. We therefore have:

$$I_h = \frac{1}{\left(g_{h,GT}\right)^2 C^2}\int w_h(E)dE = \frac{N_h}{100\left(g_{h,GT}\right)^2 C^2}, \tag{8.6.3}$$

^{12}N	^{12}C	^{12}B
$B_{GT}/B_{GT;12.7}$ 3α data only	Energy (MeV)	$B_{GT}/B_{GT;12.7}$ 3α data only
0.65(6)	7.65^{p}	0.45(10)
1.12(10)(11)	7.65^{h}	0.74(7)(14)
$0.146(^{+30}_{-10})(15)$	11.47	0.137(20)(25)
1.	12.71	1.
$0.224(^{+190}_{-30})(20)$	13.61	$0.062(^{+70}_{-40})(10)$

Table 8.6.1: B_{GT} values relative to those of the 12.7 MeV state. Values for the Hoyle state; the 11.47 MeV 0^+ state; and 13.61 MeV 2^+ state are given. In the case of the Hoyle state the values are given for the traditional method including only the 7.65 MeV peak (p) as well as for the full Hoyle state contribution (h).

with N_h as the total number of decays populating the Hoyle state. Consequently

$$\frac{B_{GT;h}}{B_{GT;12.7}} = \frac{f_{\beta;12.7}J_h}{I_h}\frac{N_h}{N_{12.7}} = 100 f_{\beta;12.7}J_h \left(g_{h,GT}\right)^2 C^2 \frac{1}{N_{12.7}} \tag{8.6.4}$$

The value of $f_{\beta;12.7}$ is given in the preceding and $N_{12.7}$ is given in table 8.1.1 for both decays. The value of $\left(g_{h,GT}\right)^2 C^2$ on the other hand is found from the fit in chapter 6 to be 0.564 and 8.75 for the ^{12}N and ^{12}B decays respectively. This gives us the B_{GT} values for the Hoyle state relative to those of the 12.7 MeV state as 1.12(10)(11) and 0.74(7)(14) for the two decays. The first uncertainty is an estimated uncertainty from the fit, whereas the second is the uncertainty on $N_{12.7}$.

As seen in table 8.6.1 the results using the traditional method and the method used by Barker & Warburton (1988)[4] are clearly different. This is because the traditional method of calculating B_{GT} values neglects threshold effects. One should therefore be very cautious when assigning B_{GT} values to states with significant ghost contributions and it is thus essential to state whether the traditional method or the full R-Matrix description has been used.

For the 11.47 MeV 0^+ state and the 13.61 MeV 2^+ state, the B_{GT} values as found in the R-Matrix formalism relative to those of the Hoyle state can easily be found from the square of the corresponding matrix elements (equation 3.2.21). The ratios of these matrix elements were found from the fit in chapter 6 where they are stated in table 6.3.6. Taking into account the estimated uncertainties and scaling to get the values relative to those of the 12.7 MeV state instead of the Hoyle state we get the values shown in table 8.6.1. The uncertainties given in the first parentheses are the uncertainties from the $B_{GT;\lambda}/B_{GT;h}$ ratio whereas the second are from the $B_{GT;h}/B_{GT;12.7}$ ratio. For the 13.61 MeV state the first part includes the mentioned uncertainty from the effects of the ^{8}Be exited

[4] Barker & Warburton describes as well an alternative method for narrow levels. This gives very similar results to the method used here

^{12}N			^{12}B		Isospin asym.
Literature value	log ft IGISOL	Energy (MeV)	log ft IGISOL	Literature value	$\log(\delta+1)$ IGISOL
4.120(3)	?	g.s.	?	4.066(2)	
5.149(7)	?	4.44	?	5.143(7)†	
4.34(6)	4.11(7)	7.65^{p}	4.13(14)	4.13(9)	
	3.87(9)	7.65^{h}	3.91(12)		−0.04(15)
4.36(17)††	4.76($^{+12}_{-8}$)	11.47	4.64(16)	4.2(2)††	0.12(20)
3.52(14)	3.92(6)	12.71	3.78(9)	?	0.14(12)
?	4.57($^{+12}_{-30}$)	13.61	5.0($^{+4}_{-5}$)	?	−0.4(5)
3.30(13)	?	15.11	–	–	–

Table 8.7.1: Recommendations for log ft values. Comparison with (Ajzenberg-Selove, 1990) where possible. For † an alternative value of 5.108(14) is given. For †† the literature values to compare with are those of the so-called 10.3 MeV state. The isospin asymmetry parameter is found as discussed in the text.

state channel (see section 6.3.9). For the latter parts the fit uncertainties on the $B_{GT;h}/B_{GT;12.7}$ are not included, since systematic uncertainties from the fits are already included in the $B_{GT;\lambda}/B_{GT;h}$ ratios. To get the full uncertainty the two uncertainties should then be combined. If however the $B_{GT;\lambda}/B_{GT;h}$ ratios are calculated from the values given in the table the first parenthesis gives the full uncertainty of this ratio.

8.7 Recommended log ft values

The central quantum mechanical observables in the description of the Gamow-Teller beta decays are the Gamow-Teller strengths (B_{GT}), the quantum mechanical overlap between the decaying state and the state it decays to. This B_{GT} value however is often given in terms of the log ft value. From the f_β and the $t_{1/2}$ values for the two decays to the 12.7 MeV state—as given in section 8.6—we therefore find the log ft values for that level to be: 3.92(6) and 3.78(9) for the ^{12}N and ^{12}B decays respectively. With these values and the relative B_{GT} values in table 8.6.1, the absolute log ft values for the states can be found as:

$$\log ft_x = \log ft_{12.7} - \log\left(\frac{B_{GT;x}}{B_{GT;12.7}}\right), \tag{8.7.1}$$

The resulting log ft values for the two decays can then be compared to the values in the available literature as shown in table 8.7.1. The log ft values for the ^{12}B decay given in the table are all calculated under the assumption that the literature value of 5.143 holds for the decay to the 4.44 MeV state, corresponding to the branching ratio value of 1.182%. If instead the alternative value of 5.108

is correct, all calculated values should be reduced by the difference of 0.035. In the table, the calculated values are furthermore compared to those given in the data evaluation by Ajzenberg-Selove (1990). This comparison will be discussed in the following.

For the ^{12}N decay to the 12.7 MeV state the deviation is significant, a bit more than 2σ. This difference corresponds directly to the difference in the branching ratios as presented in table 8.5.1. As discussed in section 8.5 the new value for this branching seems well founded and we can thus have confidence in the log ft value presented here as well. For the Hoyle state and the 11.47 MeV state (or 10.3 MeV state as it has been denoted in litterature) the situation is more involved. This stems from the fact that the two states are actually very broad states, and moreover they interfere. The log ft values should therefore be calculated from the R-Matrix description of the states and their interference. Since this is unavoidable for the 11.47 MeV state, I would recommend using the same formalism for the Hoyle state log ft value. This will allow calculation of the log ft values for the two states in a single theoretical model, and thereby make a direct comparison with the experimental values possible. In the R-Matrix formalism (equation 3.2.21 and Barker & Warburton, 1988) The contribution from the ghost of the Hoyle state is taken into account. Since this contribution is at higher energies, the contribution of the ghost to the Hoyle state log ft values is furthermore enhanced by the energy dependent f-factor. This means the beta decay is enhanced because of the ghost and the log ft value (7.65^h) is lowered significantly relative to the traditional value (7.65^p). This has the additional consequence that the value of the higher lying 0^+ state (11.47) is increased, since some of the 0^+ strength prevoiusly assigned to this state is now known to be caused by the Hoyle state ghost.

The difference in log ft values also corresponds to the difference between observed and direct R-Matrix parameters through the factor $\left(1+\gamma^2_{\lambda c}\frac{\mathrm{d}}{\mathrm{d}E}\mathcal{S}_c(E)\right)^{-1}$. When the Hoyle state is assumed to have an observed width of 7.65 eV, and the calculation is made for a channel radius corresponding to $r_0 = 1.71$ fm as in this case, the factor is 0.58. This corresponds to a difference in log ft of $\log_{10}(0.58) = -0.24$, exactly the difference between the two Hoyle state values given in the table. The difference between the 7.65^h and 7.65^p values is therefore well understood, and I would personally prefer the 7.65^h value to ease the comparison with the log ft values for the 11.47 MeV state and the 13.61 MeV state.

8.7.1 Isospin symmetry

As a final comment on the beta decays of ^{12}N and ^{12}B the isospin symmetry for the two decays can be descussed now that whe have log ft values for the decays to individual states. The possibility of an asymmetry in the two decays is conveniently discussed using the δ parameter as defined by Smirnova & Volpe

(2003) from the ratio of the beta plus and beta minus decay ft values.

$$\delta = \frac{(ft)_+}{(ft)_-} - 1 = \frac{ft(^{12}\mathrm{N})}{ft(^{12}\mathrm{B})} - 1 \tag{8.7.2}$$

For convenience, the values given in table 8.7.1 are the values of $\log(\delta + 1)$, with uncertainties given as rather conservative estimates. As seen in the table we cannot pinpoint any isospin asymmetry, except that a small preference for beta minus decay could be indicated in the case of decays to the 12.7 MeV state ($\delta > 0$).

CHAPTER 9

The stellar triple alpha process

This chapter is first and foremost intended to give a thorough documentation of the triple alpha reaction rate calculations presented recently in (Fynbo et al., 2005). This paper deals primarily with the extreme temperature ranges, relevant primarily in explosive helium burning scenarios. The results and method for calculating the reaction rate is presented in section 9.2.

Another aspect of the triple alpha reaction rate however is so important that it should not be disregarded here, namely the work presently being done on improving the triple alpha reaction rate at the temperatures relevant for hydrostatic helium burning as it takes place in Asymptotic Giant Branch (AGB) stars. Section 9.1 will therefore present the current status of the reaction rate calculations and the measurements necessary for these calculations, even though the actual work being done in this field is done by other groups and is thus not part of the work otherwise presented in this dissertation.

9.1 Hydrostatic helium burning

Before Hoyle et al. (1953) identified a 7.65 MeV 0^+ state in ^{12}C just above the triple alpha threshold, the reaction

$$3 \times {}^4\mathrm{He} \rightarrow {}^{12}\mathrm{C} + \gamma \tag{9.1.1}$$

was thought to take place through a two step reaction

$$\begin{aligned} {}^4\mathrm{He} + {}^4\mathrm{He} &\rightleftharpoons {}^8\mathrm{Be(gs)} \\ {}^8\mathrm{Be(gs)} + {}^4\mathrm{He} &\rightarrow {}^{12}\mathrm{C} + \gamma \end{aligned}$$

where the latter reaction was described as a direct reaction, that is with no intermediate ^{12}C state in the triple alpha continuum, as described by Öpik (1951) and Salpeter (1952). But as described in chapter 1 it is now known that the 7.65 MeV state (the Hoyle state), dominates the reaction rate at the temperatures where helium burning takes place. Namely $T_9 = 0.1$–2 where T_9 is the temperature in giga Kelvin (see e.g. Hoyle, 1954).

Being dominated by the Hoyle state, the reaction rate can be determined from an investigation of this state. This section will describe how the relevant information on the Hoyle state is determined and how the reaction rate is calculated from this information. The reaction rate is used in stellar evolution models, and as described by Herwig, Austin, & Lattanzio (2006) the stellar evolution can be very sensitive to the triple alpha reaction rate at these temperatures and for some scenarios it will be important to determine the rate within an uncertainty of about 5% or less.

9.1.1 The resonant triple alpha reaction rate

In the temperature range from $T_9 = 0.1$ up to $T_9 = 2$, the reaction proceeds through the two alpha cluster resonances: The ^{8}Be ground state and the ^{12}C 7.65 MeV Hoyle state, both of them 0^+ states so that with their natural parity they are available in collisions of alpha particles. The following will explain how to calculate the reaction rate of this resonant two step process. This description will largely follow the introduction of Nomoto, Thielemann, & Miyaji (1985).

At these temperatures and with the available pressure the two reactions

$$\begin{aligned} {}^4\mathrm{He} + {}^4\mathrm{He} &\rightleftharpoons {}^8\mathrm{Be(gs)} \\ {}^8\mathrm{Be(gs)} + {}^4\mathrm{He} &\rightleftharpoons {}^{12}\mathrm{C(Hoyle)} \end{aligned}$$

are in complete thermal equilibrium. This means that at any time a certain part of the available ^{4}He is actually not in the form of free helium nuclei, but has combined to form either ^{8}Be or the Hoyle state. At any time it is the population of the latter state that determine the reaction rate, since a small fraction of the populated Hoyle state nuclei does not break up into three alpha particles again, but decay electro-magnetically to the bound states in ^{12}C. With a given population n of the Hoyle state, the production $\dot{n}$ of ^{12}C nuclei is therefore:

$$\dot{n}\left({}^{12}\mathrm{C}\right) = n\left({}^{12}\mathrm{C(Hoyle)}\right)\frac{\Gamma_{\mathrm{rad}}}{\hbar}, \tag{9.1.2}$$

since the radiative width Γ_{rad} divided by $\hbar$ is the decay probability per time.

With the thermal equilibrium, the population of the individual states is governed by the Saha equation (Saha, 1920), which for the Hoyle state yields:

$$n\left({}^{12}\mathrm{C(Hoyle)}\right)\left(\frac{2\pi\hbar^2}{M_{12}k_BT}\right)^{\frac{3}{2}} = n\left({}^4\mathrm{He}\right)^3\left(\frac{2\pi\hbar^2}{M_4k_BT}\right)^{\frac{9}{2}}\exp(-Q/k_BT), \tag{9.1.3}$$

where k_BT is Boltzmann's constant times the temperature; Q is the energy difference between the three free alpha particles and the Hoyle state; and M_{12} and M_4 are the masses of the Hoyle state and the individual alpha particles respectively. With this, the rate of the triple alpha process is given by:

$$\dot{n}\left({}^{12}\mathrm{C}\right) = n\left({}^{4}\mathrm{He}\right)^3 \left(\frac{2\pi\hbar^2}{k_BT}\right)^3 \frac{M_{12}^{\frac{3}{2}}}{M_4^{\frac{9}{2}}} \exp(-Q/k_BT)\frac{\Gamma_{\mathrm{rad}}}{\hbar}. \tag{9.1.4}$$

On this we can use the approximation $M_{12} \approx 3M_4$ valid at the 10^{-4} level. Furthermore if we write it in terms of the abundances $Y_i = n_i/(\rho N_A)$ for the ^{12}C ground state ($i = 12$) and of helium ($i = 4$) where N_A is Avogadro's number and ρ is the density of the stellar plasma, we get:

$$\dot{Y}_{12} = 3^{\frac{3}{2}} Y_4^3 \rho^2 N_A^2 \left(\frac{2\pi\hbar^2}{M_4 k_BT}\right)^3 \exp(-Q/k_BT)\frac{\Gamma_{\mathrm{rad}}}{\hbar}. \tag{9.1.5}$$

With the commonly used notation:

$$N_A^2\langle\alpha\alpha\alpha\rangle = 6\dot{Y}_{12}/(\rho^2 Y_4^3) \tag{9.1.6}$$

this can be written as:

$$N_A^2\langle\alpha\alpha\alpha\rangle = 3^{\frac{3}{2}} 6 N_A^2 \left(\frac{2\pi\hbar^2}{M_4 k_BT}\right)^3 \frac{\Gamma_{\mathrm{rad}}}{\hbar} \exp(-Q/k_BT). \tag{9.1.7}$$

It is clearly seen that this reaction rate can be very temperature dependent and furthermore that the reaction rate at temperatures where this approximation is valid only depend on two properties of the Hoyle state: Its energy relative to the triple alpha threshold (Q) and its radiative width (Γ_{rad}).

9.1.2 Secular equilibrium

To illustrate how the temperature is important in determining whether complete thermal equilibrium is obtained or not, we can look at the more general assumption of secular equilibrium, which holds in a wider temperature range. In this case it is only assumed that the abundances of ^{8}Be and of the ^{12}C Hoyle state are constant in time, that is:

$$\dot{Y}\left({}^{8}\mathrm{Be}\right) = \dot{Y}\left({}^{12}\mathrm{C}(\mathrm{Hoyle})\right) = 0. \tag{9.1.8}$$

Here the ^{8}Be ground state abundance can be related to the cross section for producing the state in alpha alpha scattering, since the yield in a ^{4}He(^{4}He,)^{8}Be reaction is proportional to the relative velocity v of the helium nuclei times the cross section $\sigma_{\alpha\alpha}$. Here however we have a stellar environment where the velocities of the individual alpha particles in the plasma are not fixed, but distributed according to the Maxwell-Boltzmann distribution at the temperature of

the plasma:

$$\xi_{MB}(E)dE = \left(\frac{8}{\pi mc^2}\right)^{\frac{1}{2}} \left(\frac{1}{k_B T}\right)^{\frac{3}{2}} E \exp\left(-E/k_B T\right) dE, \tag{9.1.9}$$

where m is the reduced mass of the two colliding particles, the two being either two helium nuclei or a helium nucleus and a beryllium nucleus, depending on which of the two processes is to be calculated. Because of that σv should be averaged over the Maxwell-Boltzmann distribution:

$$\langle \alpha\alpha \rangle \equiv \langle \sigma v \rangle = \int_0^\infty \sigma_{\alpha\alpha}(E) v(E) \xi_{MB}(E) dE. \tag{9.1.10}$$

We are now in a position to investigate the beryllium abundance:

$$\begin{aligned} 0 = \dot{Y}\left({}^8\mathrm{Be}\right) \quad = \quad & \frac{1}{2}\rho N_A \langle \alpha\alpha \rangle Y_4^2 - \frac{\Gamma_\alpha({}^8\mathrm{Be})}{\hbar} Y\left({}^8\mathrm{Be}\right) \\ & -\rho N_A \langle \alpha {}^8\mathrm{Be} \rangle Y_4 Y\left({}^8\mathrm{Be}\right) \\ & + \frac{\Gamma_\alpha\left({}^{12}\mathrm{C(Hoyle)}\right)}{\hbar} Y\left({}^{12}\mathrm{C(Hoyle)}\right). \end{aligned} \tag{9.1.11}$$

Here the first term describes the production of ^{8}Be through $\alpha\alpha$ scattering and the second term describes the decay of ^{8}Be back into the $\alpha\alpha$ continuum. The two last terms deal with the contribution from the $\alpha + ^8$ Be scattering as described by Cox & Giuli (1968, pg. 499), and $\langle \alpha {}^8\mathrm{Be} \rangle$ denotes the averaged cross section for the reaction $^8\mathrm{Be}(\alpha,)^{12}\mathrm{C(Hoyle)}$. As noted by Nomoto et al. these terms are small compared to the first two, and may be neglected. With this, the beryllium abundance is found to be:

$$Y\left({}^8\mathrm{Be}\right) = \frac{1}{2}\frac{\hbar}{\Gamma_\alpha({}^8\mathrm{Be})} \rho N_A \langle \alpha\alpha \rangle Y_4^2. \tag{9.1.12}$$

The next step is to calculate the production of ^{12}C from the helium and beryllium abundances. This can be calculated directly from the cross section of the $^8\mathrm{Be}(\alpha,\gamma)^{12}\mathrm{C}$ reaction, where the intermediate ^{12}C(Hoyle) state is required to emit a gamma instead of breaking up again. This cross section must again be integrated over the Maxwell-Boltzmann distribution as in equation 9.1.10 to find $\langle \alpha {}^8\mathrm{Be} \rangle$. With this we get:

$$\dot{Y}_{12} = \rho N_A \langle \alpha {}^8\mathrm{Be} \rangle Y_4 Y\left({}^8\mathrm{Be}\right). \tag{9.1.13}$$

With the notation defined in equation 9.1.6 and with the ^{8}Be abundance (equation 9.1.12) inserted we get:

$$N_A^2 \langle \alpha\alpha\alpha \rangle = 3 N_A^2 \frac{\hbar}{\Gamma_\alpha({}^8\mathrm{Be})} \langle \alpha\alpha \rangle \langle \alpha {}^8\mathrm{Be} \rangle. \tag{9.1.14}$$

With knowledge of the energy dependence of the cross sections—and thereby the σv integrals—it will be clear how this determines the temperatures at which the resonant reaction rate is valid.

9.1.3 Cross sections and the Gamow window

The cross section of the alpha alpha scattering as a function of the center of mass kinetic energy E can be found from a scattering theory such as the R-Matrix theory (Lane & Thomas, 1958):

$$\begin{aligned}\sigma_{\alpha\alpha}(E) &= \frac{\pi(2j_\lambda+1)}{k_{\alpha\alpha}^2}\frac{\Gamma_\alpha(^8\mathrm{Be})^2}{\left(E_\lambda - E + \Delta_\alpha\right)^2 + \left(\Gamma_\alpha(^8\mathrm{Be})/2\right)^2} \\ &= \frac{\pi(2j_\lambda+1)}{k_{\alpha\alpha}^2}\left|\mathcal{P}_\alpha\gamma_{\lambda\alpha}^2 A_{\lambda\lambda}\right|^2 . \end{aligned} \tag{9.1.15}$$

Here the notation is the same as in chapter 3 equations 3.2.1 and 3.2.3, and j_λ is the spin of the contributing state λ and $k_{\alpha\alpha}$ is the wave number in the alpha alpha scattering so that

$$k_{\alpha\alpha} = \frac{2m_{\alpha\alpha}c^2E}{\hbar^2c^2}. \tag{9.1.16}$$

In the case of the alpha alpha scattering we can safely use the one level approximation, since we have no possibility of interfering states. For the alpha beryllium reaction on the other hand, we could in principle have contributions from interfering states, since as we have seen in chapters 6 and 7 that the 11.5 MeV 0^+ state interferes with the Hoyle state ghost. With that in mind, we must write the cross section as a function of the relative energy E taking into account the possibility of interference:

$$\sigma_{\alpha^8\mathrm{Be}}(E) = \frac{\pi(2j_\lambda+1)}{k_{\alpha^8\mathrm{Be}}^2}\left|\sum_{\lambda\mu}\mathcal{P}_\alpha^{\frac{1}{2}}\gamma_{\lambda\alpha}\Gamma_{\mu\mathrm{rad}}^{\frac{1}{2}}A_{\lambda\mu}\right|^2 . \tag{9.1.17}$$

Here the incoming and outgoing channels of the reaction are not the same as in the alpha alpha scattering, but rather the alpha channel and the radiative channel for incoming and outgoing channels respectively. The situation here is very similar to that of the beta decay (equation 3.2.1) and the level matrix $A_{\lambda\mu}$ is indeed defined as in equation 3.2.2. The only difference is that in the triple alpha process the incoming and outgoing channels differ from those in the beta decay. The width for the incoming channel $\alpha + ^8$ Be is thus $\Gamma_{\lambda\alpha} = \mathcal{P}_\alpha\gamma_{\lambda\alpha}^2$, whereas for the outgoing channel the width $\Gamma_{\mu\mathrm{rad}}$ is the radiative width of level μ and scales with E_γ^5, the energy available in the E2 gamma transition. The relative sign of $\gamma_{\lambda\alpha}$ and $\Gamma_{\mu\mathrm{rad}}^{\frac{1}{2}}$ when comparing two levels sets the sign of the interference, just as in the beta decay. The cross section could be written with the notation used in the one level approximation (Lane & Thomas, 1958, eqn:XII.4.2), but it gets very cumbersome and the level matrix notation ($A_{\lambda\mu}$) is therefore preferable. When calculating the level matrix for the Hoyle state one should in principle add all channel widths. What has actually been done is to neglect the small width to the gamma channel, which is a good approximation at the resonance energy, but not at lower energies far from the resonance. At these energies however we are

far from the resonance compared to the total width and the width does not play an important role in $|A_{\lambda\mu}|^2$ anyway. This is similar to the cross section seen in equation 9.1.15 where the denominator ($|A_{\lambda\lambda}|^2$) is dominated by the first term, making the second term negligible.

To identify the relevant temperatures for the resonant reaction rate approximation (section 9.1.1) we will for the time being neglect the fact that we have any resonances at all and only look at the overall energy dependence of the reaction rate. The resonances make the denominator (in for instance equation 9.1.15) approach zero thereby making the cross section diverge. Apart from this effect, the energy dependence of the cross section is determined by the penetrability $\mathcal{P}_c$ and the factor $1/k^2 \propto 1/E$. Though we actually have $\mathcal{P}_c^2$ in equation 9.1.15 one of these are canceled by the $\mathcal{P}_c$ factor in the width $\Gamma_\alpha(^8\text{Be})$ in equation 9.1.14. Writing these two factors explicitly, the cross sections can be written as:

$$\sigma(E) = S(E)\frac{1}{E}\exp\left(\left(-\frac{E_G}{E}\right)^{\frac{1}{2}}\right) \tag{9.1.18}$$

where the last part is the penetrability as described for the inverse process of alpha decay by Gamow (1928). The S-factor is slowly varying if no resonances contribute, and diverges around narrow resonances. The S-factor therefore carries all the nuclear structure information.

If σv is integrated assuming a constant S-factor, the resulting energy distribution is for a temperature peaked at a certain energy, the Gamow peak energy, which scales with $T^{\frac{2}{3}}$. This peak determines at which energies it is important to know the S-factor and thereby determines which intermediate state(s) are populated. At temperatures from $T_9 = 0.1$ to $T_9 = 2$, the ^{8}Be ground state as well as the ^{12}C Hoyle state are within the Gamow window, ensuring that the triple alpha process proceeds resonantly through these two states, making the resonant reaction rate approximation (section 9.1.1) valid. At these temperatures, the reaction rate (equation 9.1.14) reduces to the rate found from the thermal equilibrium approximation (equation 9.1.7).

9.1.4 Current status of the resonant reaction rate

With the reaction rate at resonance given in equation 9.1.7 we need measurements of the radiative width of the Hoyle state and the energy of the Hoyle state relative to the triple alpha threshold. The energy of the state is a straight forward measurement and has been determined within 0.2 keV as seen in table 9.1.1. The radiative width is more complicated, and it has been measured only through the factorization:

$$\Gamma_{rad} = \frac{\Gamma_\gamma + \Gamma_\pi}{\Gamma}\frac{\Gamma}{\Gamma_\pi}\Gamma_\pi, \tag{9.1.19}$$

where the individual factors are the radiative branching ratio, the inverse of the pair production branching ratio and the total pair width. The pair width, the width corresponding to the decay channel $^{12}\text{C(Hoyle)} \rightarrow ^{12}\text{C}(gs) + e^+e^-$, is

(a)	Q	=	$379.38 \pm 0.20\,\mathrm{keV}$	(1.2 %)
(b)	$\frac{\Gamma_\gamma+\Gamma_\pi}{\Gamma}$	=	$(4.12 \pm 0.11)\,10^{-4}$	(2.7 %)
(c)	$\frac{\Gamma_\pi}{\Gamma}$	=	$(6.8 \pm 0.7)\,10^{-6}$	(10 %)
(d)	Γ_π	=	$60.5 \pm 3.9\,\mu\mathrm{eV}$	(6.4 %)
(e)	Γ_π	=	$52.0 \pm 1.4\,\mu\mathrm{eV}$	(2.7 %)

Table 9.1.1: Parameters for determining the resonant triple alpha reaction rate. Evaluated values and errors are given along with the contributions to the error on the reaction rate. For a discussion of the individual values see text. The evaluations are listed by Ajzenberg-Selove (1990) and the latest experiment in the individual evaluations are:
(a) Nolen & Austin (1976).
(b) Markham, Austin, & Shahabuddin (1976).
(c) Alburger (1977).
(d) Strehl (1970).
(e) Crannell et al. (2005).

measured though the equivalent process: Electron scattering on the ^{12}C ground state. The two remaining on the other hand are detected in direct counting experiments, where the Hoyle state is populated in a reaction experiment, and a low background setup is used to allow detection detection of the small branching ratios. The results as used in the present evaluations of the triple alpha reaction rate are shown in table 9.1.1 references (a–d). It is clear that the combined uncertainty from these values are slightly larger than 10% and dominated by the uncertainty in the pair branch with some contribution from the pair width. There has however recently been performed a new experiment and with that a new evaluation of the pair width. This evaluation gives a significant improvement of the uncertainty. However, since the value differs by about 15% corresponding to two sigma, care should be taken when the value is used in calculating the triple alpha reaction rate. Because of this, it would be an important contribution to the understanding of the triple alpha reaction rate, if for example the total width (Γ) of the state could be measured directly, independent of the pair width. The possibility of such a detection through beta decay studies was briefly discussed in section 6.3.8.

Assuming the pair width to be under control, the uncertainty in the pair branch dominates completely. For that reason a joint collaboration from Michigan State University and Western Michigan University (Austin, 2005) is launching an experiment that is intended to improve the present value of this branching ratio. The experiment is just about to start and is expected to reduce the uncertainty to about 5%. This would yield a total uncertainty of 6% on the resonant triple alpha reaction rate, in compliance with the astrophysical requirements.

9.2 Explosive burning and extreme temperatures

At the more extreme temperatures, the reactions cannot be assumed to be resonant and in particular for the very low temperatures neither the $\alpha\alpha$ nor the α^8Be reaction are dominated by the resonant contribution (Nomoto et al., 1985).

9.2.1 The non-resonant triple alpha reaction rate

The advantage of the secular equilibrium formalism, described in sections 9.1.2 and 9.1.3, is that in the calculation of the $\langle\sigma v\rangle$ values, one does not assume that the ^{12}C state mediating the reaction is populated at resonance.

For the derivation presented above however it was assumed when calculating $\langle\alpha^8\text{Be}\rangle$, that the incoming alpha beryllium channel was an α particle and a ^{8}Be nucleus in its ground state, that is at 92 keV above the two alpha threshold (Ajzenberg-Selove, 1988). Such an assumption on the ^{8}Be energy was necessary since the energy difference between the ^{12}C intermediate state populated in the reaction and the ^{8}Be energy sets the energy available when the alpha particle penetrates the Coulomb barrier in the reaction. Since this penetrability is strongly energy dependent, the reaction rate is very sensitive to the ^{8}Be energy populated in the alpha alpha scattering. Besides this the energy difference also sets the kinetic energy required from the Maxwell-Boltzmann distribution.

At the very low temperatures below $T_9 = 0.03$ the intermediate ^{8}Be nucleus is not predominantly populated at the resonance energy but rather in the low energy tail of the resonance. To take this into account when calculating $\langle\alpha^8\text{Be}\rangle$ we must calculate this for all populated energies in ^{8}Be and find the total production of ^{12}C as the integral over the contributions from different ^{8}Be energies as done by Nomoto et al. (1985). In other words we assume secular equilibrium to be valid for all ^{8}Be energies (E):

$$\begin{aligned} 0 &= \dot{Y}\left(^8\text{Be}, E\right) dE \qquad (9.2.1)\\ &= \frac{1}{2}\rho N_A Y_4^2 \sigma_{\alpha\alpha}(E) v(E) \xi_{MB}(E) dE - \frac{\Gamma_\alpha(^8\text{Be}, E)}{\hbar} Y\left(^8\text{Be}, E\right) dE. \end{aligned}$$

That is

$$Y\left(^8\text{Be}, E\right) dE = \frac{1}{2}\hbar\rho N_A Y_4^2 \left[d\langle\alpha\alpha\rangle^\dagger(E)/dE\right] dE, \qquad (9.2.2)$$

if we define

$$\left[d\langle\alpha\alpha\rangle^\dagger(E)/dE\right] = \frac{\sigma_{\alpha\alpha}(E) v(E) \xi_{MB}(E)}{\Gamma_\alpha(^8\text{Be}, E)}, \qquad (9.2.3)$$

the integrand of the $\langle\alpha\alpha\rangle$ integration divided by the energy dependent width. Note, that since we here use the cross sections directly and not a parameterization of the S-factor as in the calculation of Nomoto et al. (1985) the width $\Gamma(E) = \mathcal{P}_c(E)\gamma^2$ appears explicitly. For that reason it is more convenient to include the entire $1/\Gamma_\alpha(^8\text{Be}, E)$ factor and not just the energy dependent part of it as done by Nomoto et al..

With this we can calculate the reaction rate as

$$N_A^2\langle\alpha\alpha\alpha\rangle = 3N_A^2\hbar\int_0^\infty \left[d\langle\alpha\alpha\rangle^\dagger(E)/dE\right]\langle\alpha^8\mathrm{Be}(E)\rangle dE. \tag{9.2.4}$$

Here the alpha alpha cross section is still as given in the preceding (equation 9.1.15). When calculating the ^{8}Be cross section however, we must take special care, since as described in section 3.4 and restated in equation 9.2.5 the level matrix is more complicated when the decay channel is not a narrow state but either a broad state or as in this case the low energy tail of a narrow state. Compared to chapter 7 however the situation does simplify a bit when the ^{12}C energy is so low that only the ^{8}Be 0^+ ground state can contribute to the breakup of the intermediate ^{12}C state and thereby contribute to the level matrix. With this the level matrix is:

$$\begin{aligned}&\left(A(E_{^{12}\mathrm{C}})^{-1}\right)_{\lambda\mu} = (E_\lambda - E_{^{12}\mathrm{C}})\delta_{\lambda\mu} \\ &-\int_0^\infty \gamma_{\lambda\alpha}\gamma_{\mu\alpha}\left(\mathcal{S}_\alpha(E_{^{12}\mathrm{C}} - E_{^8\mathrm{Be}}) - \mathcal{B}_\alpha + i\mathcal{P}_\alpha(E_{^{12}\mathrm{C}} - E_{^8\mathrm{Be}})\right)\rho_{\alpha\alpha}(E_{^8\mathrm{Be}})dE_{^8\mathrm{Be}}.\end{aligned} \tag{9.2.5}$$

For negative values of $E_{^{12}\mathrm{C}} - E_{^8\mathrm{Be}}$ the penetrability ($\mathcal{P}$) is of course zero whereas the shift function can contribute at negative energies. The negative energy contribution to the shift function integral however was not included in the calculation for which the results were shown in (Fynbo et al., 2005), but should be included in future compilations of the reaction rate at low energies. As we will see in section 9.2.5 however the present tests of stellar evolution models indicate little sensitivity on the low temperature triple alpha reaction rate.

9.2.2 Summary of contributions

With the method for calculating the reaction rate in hand, we will in the following review the nuclear physics input to the calculations. The needed input is the possible contributing states in the reaction along with threshold effects beyond the Breit-Wigner shape of the individual states. This is summarized in tables 9.2.1 and 9.2.2 for the low temperature and high temperature regions respectively. As seen in the preceding section, for the non-resonant contributions to the reaction rate it is necessary to know not only the energy and the radiative width of the state but the total width as well. All three are therefore listed.

For the low temperature region below $T_9 = 0.1$ the only relevant contribution is from 0^+ strength in the two intermediate nuclei. This is because higher angular momentum contributions are precluded by their larger angular momentum barrier. This means the most important contribution is the low energy tails of the Hoyle state and the ^{8}Be ground state. As described in the preceding sections, one must be careful when describing these low energy tails. Firstly because the tail (the non resonant contribution to the rate) is dominating the reaction rate at these temperatures (Nomoto et al., 1985) and secondly because the tails of the states do not really follow the Breit-Wigner distribution because of threshold

^{12}C	J^π	E_λ	Γ	Γ_{rad}
(a)	0^+	7.65420(15) MeV	8.5(10) eV	3.7(5) meV
(b)			7.6(10) eV	3.2(4) meV
(c)	Direct $L = 0$, E2 radiative capture to 4.44 MeV state.			
^{8}Be	J^π	E_x	Γ	
(d)	0^+	91.8 keV	5.57(25) eV	
^{8}Be and ^{12}C				
(e)	Non-resonant contribution to reaction rate.			
(f)	Threshold effects on low energy tail of continuum states.			

Table 9.2.1: Possible contributions to the low temperature reaction rate. For discussion of the individual contributions see text. Energy in ^{12}C is relative to the ground state whereas in ^{8}Be it is given relative to the $\alpha\alpha$ threshold.
(a) Ajzenberg-Selove (1990).
(b) Ajzenberg-Selove (1990) and Crannell et al. (2005).
(c) Langanke et al. (1986).
(d) Tilley et al. (2004).
(e) Nomoto et al. (1985).
(f) Section 9.2.1 and Fynbo et al. (2005).

effects. For an alternative treatment of effects beyond the Breit-Wigner shape of the states, Langanke, Wiescher, & Thielemann (1986) has described direct $L = 0$ capture with radiative E2 decay to the 4.44 MeV bound state of ^{12}C. This was described in a potential model and indicated an increase of about a factor of two relative to the reaction rate from a Breit-Wigner distribution with energy dependent width.

For the high temperature region above $T_9 = 2$, higher spin states can come into play, though only natural parity states can contribute since the reacting alpha particles carry an internal spin-parity of 0^+. All relevant contributions are listed in the table. As is clearly seen, the radiative widths are in general poorly known, as is to be expected since they are weak decay branches.

For the 0^+ strength, the ghosts of the ^{8}Be ground state and of the Hoyle state can potentially be of importance, and to the degree that the Hoyle state ghost is important, it is important to take into account the interference with the 11.47 MeV state. For this interference however we have no information on the sign. This is because the sign of the interference depends on the incoming and outgoing channels in the reaction, and since the measurement presented in this dissertation probed the state through beta decay, i.e. another channel, the measured sign is not directly related to the sign entering in the reaction rate calculations. The uncertainty introduced by this ambiguity however is fortunately very small, as will be seen in section 9.2.5.

The 2^+ strength suggested by Descouvemont & Baye (1987) would contribute

^{12}C	J^π	E_λ	Γ	Γ_{rad}
(a)	0^+	7.65420(15) MeV	8.5(10) eV	3.7(5) meV
(b)			7.6(10) eV	3.2(4) meV
(c)	0^+	11.47(16) MeV	3.44(35) MeV	unknown
(d)	2^+	9 MeV	0.56 MeV	0.2 eV
(e)	2^+	11.46(20) MeV	0.43(10) MeV	
(f)	2^+	9–11 MeV	1 MeV	
(a)	3^-	9.6 MeV	35(5) keV	0.3 meV $< \Gamma_{rad} <$ 14 meV
(a)	1^-	10.8 MeV	315(25) keV	unknown
^{8}Be	J^π	E_x	Γ	
(g)	0^+	91.8 keV	5.57(25) eV	
(h)	ghost	1 MeV	1 MeV	
(g)	2^+	3.12 MeV	1513(15) keV	

Table 9.2.2: Possible contributions to the high temperature reaction rate. For discussion of the suggested states see text. Energies are given as in table 9.2.1.
(a) Ajzenberg-Selove (1990).
(b) Ajzenberg-Selove (1990) and Crannell et al. (2005).
(c) Chapter 6, table 6.3.6.
(d) Descouvemont & Baye (1987).
(e) Bency John et al. (2003).
(f) Itoh et al. (2004).
(g) Tilley et al. (2004)
(h) Chapter 3, figure 3.1.1.

significantly to the reaction rate, but the current experimental data suggesting such a 2^+ state places it at a somewhat higher energy (Bency John et al., 2003; Itoh et al., 2004). If placed at an energy as high as that suggested by Bency John et al., the contribution will certainly be very small, since the contribution from the individual states depend strongly on the state energy as seen already from the resonant reaction rate contribution (equation 9.1.7). If however a 2^+ state in this energy range is included, one will have to take special care in describing its shape, since it will interfere with the 13.6 MeV 2^+ state as illustrated in figure 7.4.5.

For the negative parity contributions 3^- and 1^-, the states are well established, but the radiative widths are poorly known. Assuming the uncertainties are taken into account properly, the states should be included in reaction rate calculations though the effect of these states is modest.

Regarding the ^{8}Be states, the 2^+ state is positioned at such a high energy that it is unlikely to contribute significantly. The ghost of the ground state on the other hand should be taken into account, since it will be important whenever states in ^{12}C at high energies contribute. This is the case if the 3^- state or the suggested 9 MeV 2^+ state are included. The formalism stated in equation 9.2.4

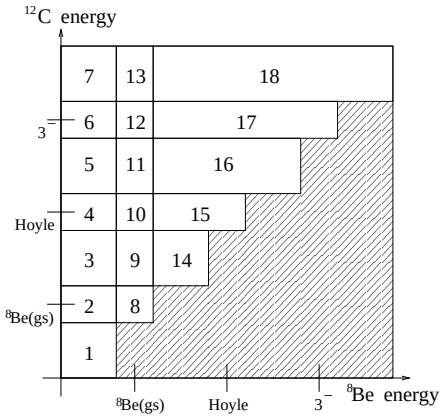

Figure 9.2.1: Integration regions for numerical integration of reaction rate, equation 9.2.4. The integration is performed over regions 1–18 whereas the marked region does not contribute to the reaction rate.

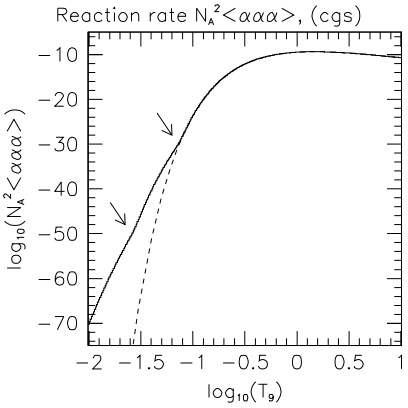

Figure 9.2.2: Numerically integrated triple alpha reaction rate (solid line) and (dashed) the resonant reaction rate as in equation 9.1.7. Arrows mark the temperatures where the $\alpha\alpha$ and α^8Be reactions become dominated by the resonant reaction rate.

however does include this effect as long as one remembers the high energy region when evaluating the integral.

9.2.3 Numerical integration of the cross sections

The numerical integration is performed using the multidimensional adaptive routine DCUHRE (Berntsen et al., 1991a,b) as in section 3.4. This integration routine requires the integration regions to be rectangular, and since we furthermore have narrow states as well as broader contributions, the integration regions are defined as shown in figure 9.2.1. The regions around the narrow states: The ^{8}Be ground state; the Hoyle state; and the 9.6 MeV 3^- state in ^{12}C are all defined as the state energy plus-minus 20 times the width of the state. This ensures that the numerical integration routine identifies both the narrow resonance contributions and the broader contributions from tails of the states or from narrow resonances. Though not essential, it turns out to be convenient to introduce separate regions in the ^{12}C energy around the ^{8}Be ground state energy, since especially the integrated level matrix (equation 9.2.5) varies significantly over this energy region. The reaction rate as found through the numerical integration is shown in figure 9.2.2. As illustrated, the reaction rate is dominated by the resonant rate (section 9.1) above $\log(T_9) = -1$ while the $\alpha\alpha$ reaction is resonant already from

1	$2.43 \cdot 10^9$	8	23.570	15	$3.26 \cdot 10^2$
2	13.490	9	0.16	16	$3.07 \cdot 10^{-16}$
3	$2.25 \cdot 10^{-2}$	10	$1.307 \cdot 10^2$	17	29.1
4	$6.09 \cdot 10^5$	11	3.338	18	$1.308 \cdot 10^3$
5	1.054	12	$2.51 \cdot 10^4$	19	$3.44 \cdot 10^{-16}$
6	74.5	13	20.307	20	$1.58 \cdot 10^{-2}$
7	$2.76 \cdot 10^7$	14	5.47	21	0.65

Table 9.2.3: Reaction rate parameterization from the Nacre compilation (Angulo et al., 1999).

$\log(T_9) = -1.5$ and upwards.

9.2.4 Analytical form for the reaction rate

In the reaction rate compilation by Angulo et al. (1999), the triple alpha rate has been described by the following analytical approximation.

$$\begin{aligned} \chi_{11} &= P_1 \cdot T_9^{-2/3} \cdot \exp(-P_2 \cdot T_9^{-1/3} - T_9^2/P_3) \\ \chi_{12} &= P_4 \cdot T_9^{-3/2} \cdot \exp(-P_5/T_9) \\ N_A\langle\sigma v\rangle^{\alpha\alpha} &= \chi_{11} \cdot (1 + P_6 \cdot T_9) + \chi_{12} \end{aligned}$$

$$\begin{aligned} \chi_{21} &= P_7 \cdot T_9^{-2/3} \cdot \exp(-P_8 \cdot T_9^{-1/3} - T_9^2/P_9) \\ \chi_{22} &= P_{10} \cdot T_9^{-3/2} \cdot \exp(-P_{11}/T_9) \\ \chi_{23} &= P_{12} \cdot T_9^{-3/2} \cdot \exp(-P_{13}/T_9) \\ N_A\langle\sigma v\rangle^{\alpha\,{}^8\mathrm{Be}} &= \chi_{21} \cdot (1 + P_{14} \cdot T_9 + P_{15} \cdot T_9^2) + \chi_{22} + \chi_{23} \end{aligned}$$

$$\begin{aligned} f &= \begin{cases} P_{16} \cdot (1 - P_{17} \cdot T_9 + P_{18} \cdot T_9^2) & T_9 \leq 0.03 \\ P_{19} \cdot (1 + P_{20} \cdot T_9^{-P_{21}}) & T_9 \geq 0.03 \end{cases} \\ N_A^2\langle\alpha\alpha\alpha\rangle &= N_A\langle\sigma v\rangle^{\alpha\alpha} \cdot N_A\langle\sigma v\rangle^{\alpha\,{}^8\mathrm{Be}} \cdot f \end{aligned} \tag{9.2.6}$$

For astrophysical usage of the reaction rate it is important to have a continuous parameterization of the reaction rate. To ensure this continuity one may define P_{19} as:

$$P_{19} = P_{16} \cdot \frac{1 - P_{17} \cdot T_x + P_{18} \cdot T_x^2}{1 + P_{20} \cdot T_x^{-P_{21}}}. \tag{9.2.7}$$

In the Nacre parameterization, a good set of parameters were found to be the set stated in table 9.2.3. This described their calculated reaction rate within 5% over most of the temperature range. In this parameterization P_1 to P_6 describe most of the effect from the $\alpha\alpha$ reaction whereas parameters P_7 to P_{15} similarly

1	$2.368 \cdot 10^{9}$	8	23.6448	15	$3.629 \cdot 10^{2}$
2	13.6672	9	$3.274 \cdot 10^{-2}$	16	$1.603 \cdot 10^{-16}$
3	$4.300 \cdot 10^{-3}$	10	88.7912	17	25.207
4	$6.090 \cdot 10^{5}$	11	3.3432	18	85.453
5	1.0631	12	$2.493 \cdot 10^{4}$	19	$5.4266 \cdot 10^{-16}$
6	162.52	13	158.4144	20	$-3.989 \cdot 10^{-2}$
7	$2.76 \cdot 10^{7}$	14	5.4986	21	0.0798

Table 9.2.4: Reaction rate parameterization, fit to numerical integration.

describe the α^8Be reaction. For that reason, denoting the two parts as $N_A\langle\sigma v\rangle^{\alpha\alpha}$ and $N_A\langle\sigma v\rangle^{\alpha\,^8\mathrm{Be}}$ is reasonable even though the reaction rate does not strictly speaking factorize in the two contributing reactions at all temperatures as can be seen from the integral in equation 9.2.4.

For the rate presented in figure 9.2.2 a good set of parameters is presented in table 9.2.4. This parameterization describes the reaction rate within 2.5% in most of the presented temperature range, except at low temperature where the deviation is up to 5% and at high temperatures where up to 15% discrepancy is seen. In this parameterization however it must be noted that most of the parameters have been free when fitting to the integrated reaction rate. The distinction between the $\alpha\alpha$ part and the α^8Be part is therefore no longer meaningful. For the same reason the rate parameterization should not be expected to hold outside the plotted $T_9 = 0.01$–10 temperature range.

9.2.5 Comparison with the reaction rates in literature

With the calculation of the integrated reaction rate and the analytical parameterization of the rate in hand we are ready to compare our rate to commonly used rates in the literature.

With the many orders of magnitude variation in the reaction rate over the investigated temperature region (figure 9.2.2) it is convenient to view the reaction rates relative to each other. Since the NACRE reaction rate (Angulo et al., 1999) is commonly used especially in Europe, the reaction rates are presented relative to that rate in figure 9.2.3 (as in: Fynbo et al., 2005). To allow a direct comparison with the NACRE rate, the triple alpha rate calculation is here done using the same Hoyle state parameters as used by Angulo et al.. These deviates from the parameters in table 9.2.1 in the three values: $E_\lambda(^8\mathrm{Be}) = 92.08\,\mathrm{keV}$, $\Gamma(\mathrm{Hoyle}) = 8.3(10)\,\mathrm{eV}$ and $\Gamma_{rad}(\mathrm{Hoyle}) = 3.7(5)\,\mathrm{meV}$. The temperature dependent uncertainty is not calculated for the presented rate, but since the uncertainties are dominated by the uncertainties in the nuclear physics input, it is reasonable to assume that the uncertainty is similar to that of the NACRE rate.

As noted in section 9.2.2, different states may contribute to the reaction rate. The calculated rates presented in figure 9.2.3 are therefore not only the pure Hoyle state reaction rate, but as well reaction rates where interference with

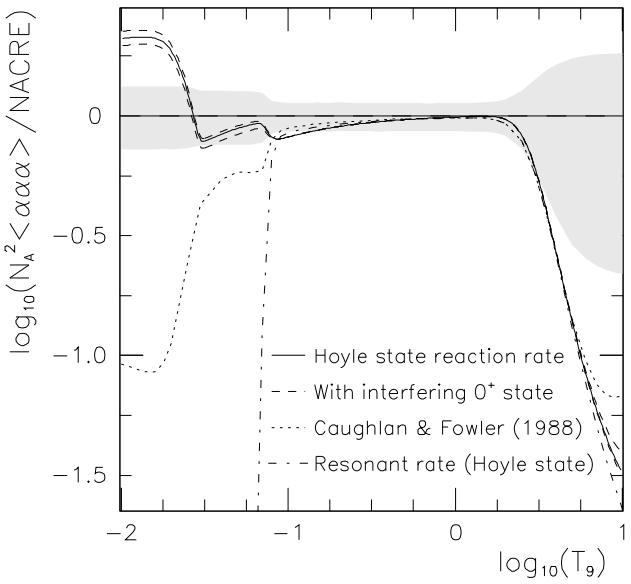

Figure 9.2.3: Comparison of calculated reaction rates to the Nacre rate, which is shown with its stated uncertainty. Integrated reaction rate (equation 9.2.4) for pure Hoyle state rate as well as for Hoyle state interfering with higher lying 0^+ state (chapter 6). Furthermore comparison to Caughlan & Fowler (1988) and the resonant reaction rate for pure Hoyle state triple alpha reaction.

the 11.47 MeV 0^+ state is taken into account. The two presented interference rates are calculated under the assumption that the higher lying state has the radiative width of the Hoyle state scaled with the E_γ^5 energy dependence from the E2 decay to the 4.44 MeV state. The two rates have been calculated for opposite interference, but as seen in the figure, the uncertainty introduced by this ambiguity is small. The radiative width of the higher lying state would have to be increased by more than a factor of three for this uncertainty to be significant in comparison to the uncertainty estimate given in the Nacre rate. For simplicity, all three reaction rates are calculated without the contribution from the 9.6 MeV 3^- state.

As seen in the figure, all rates agree quite well in the central region where the resonant Hoyle state reaction rate dominates. In the upper temperature

region on the other hand, the deviation between the NACRE rate and the others is significant. This difference is primarily caused by the inclusion/exclusion of the 9 MeV 2^+ state. In this temperature region I would therefore recommend the Caughlan & Fowler (1988) reaction rate. At temperatures above $T_9 = 5$ this rate exceeds the Hoyle state reaction rate slightly, because of the inclusion of the 3^- state. Very few—if any—astrophysical scenarios however are sensitive to the triple alpha reaction rate at these temperatures, so for practical purposes the Hoyle state reaction rate is almost as good.[1]

For the low temperatures, the correspondence is best between our rate and the NACRE rate and I would therefore recommend using our rate, or alternatively the NACRE rate. There has so far been published at least one test of the influences from these low temperature reaction rate changes on the evolution of stars with very low metalicity, stars that have no—or very little—carbon in its initial composition (Weiss et al., 2005). Is this paper the authors find that the difference between our rate and the NACRE rate has no significant effect on the evolution of such stars. One deviation however is worth noting, namely the (1.5σ) difference of about 20% around $T_9 = 0.1$. This disagreement will have to be settled before we can claim to know the triple alpha reaction rate to 5% from $T_9 = 0.1$ up to $T_9 = 2$ which as stated in section 9.1 is an important goal for the future.

[1] As a warning for those using the Caughlan & Fowler rate, note that the rate of Caughlan et al. (1985) is not in agreement with the 1988 rate. For astrophysical simulations where the 1985 rate is still hidden somewhere in the code, it will therefore be important to update that rate.

CHAPTER 10

Summary

In this dissertation I have presented experimental results on ^{12}C states in the triple alpha continuum, probed in the beta decays of ^{12}N and ^{12}B. Furthermore I have applied these results to the description of the stellar triple alpha reaction rate. The dissertation presents three different aspects of the continuum states besides the investigation of the internal structure of the states: Firstly their coupling to the triple alpha continuum; secondly their Gamow-Teller coupling to the isobaric neighbors of ^{12}C, the ^{12}N and ^{12}B ground states; and thirdly how their coupling to the bound states of ^{12}C determines the stellar triple alpha reaction rate. These three aspects of the analysis are illustrated in figure 10.0.1.

Starting with *the internal properties of the states*, I have investigated the 0^+ and 2^+ strengths in ^{12}C in the energy range from 8.5 MeV up to 14.3 MeV corresponding to the interval (1.2 MeV:7.0 MeV) above the triple alpha threshold. With an R-Matrix model including interference, it is possible to describe this strength in terms of three states in ^{12}C *if* the included states are: The well known Hoyle state (0^+; 7.65 MeV) contributing with its ghost; a higher energy 0^+ state at 11.47(16) MeV overlapping with the ghost of the Hoyle state and interfering with it; and a 2^+ state at 13.61(14) MeV. A 2^+ state at lower energies as for example the three suggestions by Descouvemont & Baye (1987), Bency John et al. (2003) and Itoh et al. (2004) is not confirmed. Note however for further studies that such a state, if present, will interfere with the 13.61 MeV state.

Regarding *the coupling of the states to the triple alpha continuum*, the state at 11.47 MeV has a width of 3.44(35) MeV dominated by the breakup through the narrow ground state of ^{8}Be. For the entire 0^+ strength however, there is a small fraction ($\approx 10\%$) of the breakups that go through higher energies of ^{8}Be. Within

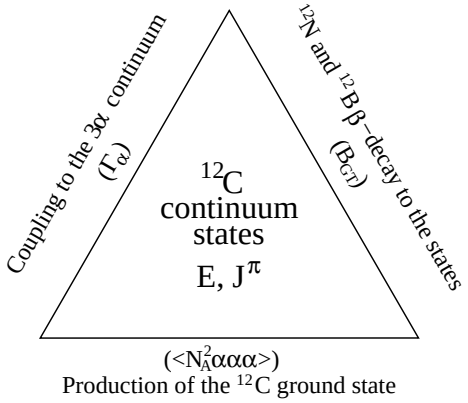

Figure 10.0.1: Three properties of the triple alpha continuum states as presented in this dissertation.

the uncertainty of the model, this breakup channel can be adequately described by a breakup through the ghost of the ^{8}Be ground state, in terms of the ^{12}C energy distribution as well as in the breakup kinematics. For the 13.61 MeV 2^+ state on the other hand, the breakup through the ^{8}Be ground state can only account for about half of the measured breakups. The remaining are breakups through the ^{8}Be 2^+ excited state, dominated by breakups where the first alpha particle carries an angular momentum of $L = 2$ relative to the two remaining alpha particles. The total width of the 13.61 MeV state is $\Gamma_\alpha = 1.68(20)$ MeV.

For *the coupling to the beta decaying nuclei ^{12}N and ^{12}B*, branching ratios to different energy regions as well as coupling constants to the individual states have been calculated. This has been done for the three mentioned 0^+ and 2^+ states as well as for the 1^+ state at 12.7 MeV in ^{12}C. For the beta decay of ^{12}B, the measured branching ratios are consistent with the values given in literature where such are available. For the ^{12}N decay, the branching ratios identified in this work differ from the literature values by more than 2σ for the Hoyle state as well as for the 12.7 MeV state. All values are given in table 8.5.1. The beta decay coupling constant (the B_{GT} value) is given in terms of the logarithm of its inverse, the log ft value. For this the same deviations are seen as was the case for the branching ratios in the ^{12}N decay. All measured log ft values are between 3.7 and 5.0 consistent with the beta decays being allowed Gamow-Teller transitions. For all four states the isospin symmetry has furthermore been confirmed within the experimental uncertainties.

The last process investigated with regards to the triple alpha continuum states is *the stellar triple alpha process* in which ^{12}C is produced. This process is strongly dependent on the properties of the contributing ^{12}C states. With the results mentioned above, and in particular with the lacking confirmation of a 9 MeV 2^+ state, the triple alpha reaction rate at high temperatures ($T > 2$ GK) is

reduced significantly relative to the much used NACRE rate (Angulo et al., 1999). For high temperature reaction rates I would therefore recommend using either the rate presented in this dissertation or alternatively the rate of Caughlan & Fowler (1988). For the low temperatures ($T < 0.1\,\mathrm{GK}$) on the other hand, I recommend the use of either my reaction rate calculation or the NACRE rate. For medium range temperatures, all three rates are similar, though smaller differences around $T = 0.1\,\mathrm{GK}$ must be clarified before we can reach the future goal of a precision of 5% in the 0.1 GK to 2 GK temperature range.

Bibliography

Agostinelli, S., Allison, J., Amako, K., et al. 2003, GEANT4—a simulation toolkit, Nuclear Instruments and Methods A, 506, 250

Ajzenberg-Selove, F. 1988, Energy levels of light nuclei A = 5–10, Nuclear Physics A, 490, 1

Ajzenberg-Selove, F. 1990, Energy levels of light nuclei A = 11–12, Nuclear Physics A, 506, 1

Alburger, D. E. 1977, Pair decay of the 7.65-MeV level of ^{12}C, Physical Review C, 16, 2394

Angulo, C., Arnould, M., Rayet, M., et al. 1999, A compilation of charged-particle induced thermonuclear reaction rates, Nuclear Physics A, 656, 3

Arndt, M., Nairz, O., Vos-Andreae, J., et al. 1999, Wave-particle duality of C_{60} molecules, Nature, 401, 680

Audi, G., Bersillon, O., Blachot, J., & Wapstra, A. H. 2003, The NUBASE evaluation of nuclear and decay properties, Nuclear Physics A, 729, 3

Austin, S. M. 2005, Making carbon in stars, Nuclear Physics A, 758, 375

Äystö, J. 2001, Development and applications of the IGISOL technique, Nuclear Physics A, 693, 477

Äystö, J., Bergmann, U. C., Borge, M. J. G., et al. 2002, Study of the β-decay of ^{12}B, proposal to the ISOLDE and Neutron Time-of-Flight Experiments Committee (INTC)

Baker, S. & Cousins, R. D. 1984, Clarification of the use of Chi-square and likelihood functions in fits to histograms, Nuclear Instruments and Methods, 221, 437

Balamuth, D. P., Zurmühle, R. W., & Tabor, S. L. 1974, Isospin-forbidden alpha decay of the 15.11-MeV state in ^{12}C, Physical Review C, 10, 975

Barker, F. C. 1969, 2^+ states of ^{8}Be, Australian Journal of Physics, 22, 293

Barker, F. C. 1972, The boundary condition parameter in R-Matrix theory, Australian Journal of Physics, 25, 341

Barker, F. C., Hay, H. J., & Treacy, P. B. 1967, 0^+ states of ^{8}Be, Australian Journal of Physics, 21, 239

Barker, F. C. & Treacy, P. B. 1962, Nuclear levels near thresholds, Nuclear Physics, 38, 33

Barker, F. C. & Warburton, E. K. 1988, The beta-decay of ^{8}He, Nuclear Physics A, 487, 269

Barlow, R. J. 1989, Statistics: A guide to the use of statistical methods in the physical sciences (John Wiley & Sons, Inc.)

Becchetti, F. D., Fields, C. A., Raymond, R. S., & Bhang, H. C. 1981, Ghost anomaly in ^{8}Be studied with ^{9}Be(p,d) at E_p=14.3 and 26.2 MeV, Physical Review C, 24, 2401

Bency John, Tokimoto, Y., Lui, Y.-W., et al. 2003, Isoscalar electric multipole strength in ^{12}C, Physical Review C, 68, 014305

Bergmann, U. C., Borge, M. J. G., Cederkäll, J., et al. 2003a, Study of the β-decay of ^{12}N and ^{12}B at IGISOL, proposal to the JYFL PAC

Bergmann, U. C., Fynbo, H. O. U., & Tengblad, O. 2003b, Use of Si strip detectors for low-energy particles in compact geometry, Nuclear Instruments and Methods A, 515, 657

Berntsen, J., Espelid, T. O., & Genz, A. 1991a, An adaptive algorithm for the approximate calculation of multiple integrals, ACM Transactions on Mathematical Software, 17, 437

Berntsen, J., Espelid, T. O., & Genz, A. 1991b, Algorithm 698 DCUHRE: an adaptive multidimensional integration routine for a vector of integrals, ACM Transactions on Mathematical Software, 17, 452

Blank, B., Giovinazzo, J., & Pfützner, M. 2003, First observation of two-proton radioactivity from an atomic nucleus, Comptes Rendus Physique, 4, 521

Brun, R. & Rademakers, F. 1997, ROOT—An object oriented data analysis framework, Nuclear Instruments and Methods A, 389, 81

Brune, C. R. 2002, Alternative parametrization of R-matrix theory, Physical Review C, 66, 044611

Buchmann, L., Gete, E., Chow, J. C., King, J. D., & Measday, D. F. 2001, β-delayed particle decay of ^{9}C and the $A = 9$, $T = 1/2$ nuclear system: R-Matrix fits, the $A = 9$ nuclear system, and the stellar reaction rate of $^{4}\mathrm{He}(\alpha n, \gamma)^{9}\mathrm{Be}$, Physical Review C, 63, 034303

Caughlan, G. & Fowler, W. 1988, Thermonuclear reaction rates, Atomic Data and Nuclear Data Tables, 40, 283

Caughlan, G. R., Fowler, W. A., Harris, M. J., & Zimmerman, B. A. 1985, Tables of thermonuclear reaction rates for low-mass nuclei ($1 \leq \mathrm{Z} \leq 14$), Atomic Data and Nuclear Data Tables, 32, 197

Clifford, E. T. H., Hagberg, E., Hardy, J. C., et al. 1989, The decay of ^{20}Na, Nuclear Physics A, 493, 293

Cook, C. W., Fowler, W. A., Lauritsen, C. C., & Lauritsen, T. 1957, B^{12}, C^{12}, and the red giants, Physical Review, 107, 508

Cook, C. W., Fowler, W. A., Lauritsen, C. C., & Lauritsen, T. 1958, High energy alpha particles from B^{12}, Physical Review, 111, 567

Cox, J. P. & Giuli, R. T. 1968, Principles of stellar structure, Vol. 1 (Gordon and Breach, Science Publishers)

Crannell, H., Jiang, X., O'Brien, J. T., Sober, D. I., & Offermann, E. 2005, Measurement of the pair transition width for the decay of the 7.654 MeV, 0^{+} state in ^{12}C, Nuclear Physics A, 758, 399

Dalitz, R. 1953, On the analysis of τ-meson data and the nature of the τ-meson, The Philosophical Magazine, 44, 1068

Descouvemont, P. & Baye, D. 1987, Microscopic theory of the $^{8}\mathrm{Be}(\alpha, \gamma)^{12}\mathrm{C}$ reaction in a three-cluster model, Physical Review C, 36, 54

Diget, C. A. 2004, A corner-stone of life—states in the triple alpha continuum, unpublished progress report, available at http://whome.phys.au.dk/~diget/

Diget, C. A., Barker, F. C., Borge, M. J. G., et al. 2005, Properties of the ^{12}C 10 MeV state determined through β-decay, Nuclear Physics A, 760, 3

Dunbar, D. N. F., Pixley, R. E., Wenzel, W. A., & Whaling, W. 1953, The 7.68-MeV state in C^{12}, Physical Review, 92, 649

Eadie, W. T., Drijard, D., James, F. E., Roos, M., & Sadoulet, B. 1971, Statistical methods in experimental physics (North-Holland Publishing Company)

Eidelman, S., Hayes, K. G., Olive, K. A., et al. 2004, Review of particle physics, Physics Letters B, 592, 1

Einstein, A. 1905, Ist die Trägheit eines Körpers von seinem Energieinhalt abhängig?, Annalen der Physik, 18, 639

Feshbach, H. & Kerman, A. K. 1967, Nuclear forces I, Comments on Nuclear and Particle Physics, 1, 132

Firestone, R. B. & Shirley, V. S. 1996, Table of isotopes, 8th edn. (John Wiley & Sons)

Fowler, W. A. 1993, Experimental and theoretical nuclear astrophysics; the quest for the origin of the elements, in Nobel Lectures, Physics 1981–1990, ed. G. Ekspång (World Scientific Publishing Co.), 172–229

Fynbo, H. O. U., Borge, M. J. G., Axelsson, L., et al. 2000, The β2p decay mechanism of ^{31}Ar, Nuclear Physics A, 677, 38

Fynbo, H. O. U., Diget, C. A., Bergmann, U. C., et al. 2005, Revised rates for the stellar triple-alpha process from measurement of ^{12}C nuclear resonances, Nature, 433, 136

Fynbo, H. O. U., Prezado, Y., Bergmann, U. C., et al. 2003, Clarification of the three-body decay of ^{12}C(12.71 MeV), Physical Review Letters, 91, 082502

Gaarde, C., Larsen, J. S., Harakeh, M. N., et al. 1980, The ^{48}Ca(^{3}He,t)^{48}Sc reaction at 66 and 70 MeV. Reaction mechanism and Gamow-Teller strength, Nuclear Physics A, 334, 248

Gamow, G. 1928, Zur quantentheorie des atomkernes, Zeitschrift für Physik, 51, 204

Goodman, C. D. 1990, Comment on testing the Gamow-Teller sum rule, Physical Review C, 42, 1150

Hamilton, D. R. 1947, Electron-neutrino angular correlation in beta-decay, Physical Review, 71, 456

Herrmann, G. 1988, From Srafap to Sisak—rapid chemical separation in nuclear research, award Address, American Chemical Society, Nuclear Chemistry Award (GSI-Report: GSI-88-22)

Herwig, F., Austin, S. M., & Lattanzio, J. C. 2006, Nuclear reaction rate uncertainties and astrophysical modeling: Carbon yields from low-mass giants, Physical Review C, 73, 025802

Hoyle, F. 1954, On nuclear reactions occuring in very hot stars I. The synthesis of elements from carbon to nickel, Astrophysical Journal Supplement Series, 1, 121

Hoyle, F., Dunbar, D. N. F., Wenzel, W. A., & Whaling, W. 1953, A state in C^{12} predicted from astrophysical evidence, in Minutes of the New Mexico Meeting Held at Alberquerque, September 2, 3, 4 and 5, Physical Review, Vol. 92, 1095c

Itoh, M., Akimune, H., Fujiwara, M., et al. 2004, Study of the cluster state at E_x=10.3 MeV in ^{12}C, Nuclear Physics A, 738, 268

James, F. 1994, MINUIT, function minimization and error analysis, CERN Program Library Long Writeup D506

Kankainen, A., Eronen, T., Fox, S. P., et al. 2006, Excited states in ^{31}S studied via beta decay of ^{31}Cl, The European Physical Journal A, 27, 67

Kippenhahn, R. & Weigert, A. 1990, Stellar structure and evolution, 1st edn. (Springer-Verlag)

Koch, J., Kofoed-Hansen, O., Kristensen, P., & Drost-Hansen, W. 1949, Measurements on radioactive krypton isotopes from fission after mass-spectrographic separation, Physical Review, 76, 279

Kofoed-Hansen, O. & Nielsen, K. 1951, Measurements on shortlived radioactive krypton isotopes from fission after isotopic separation, Matematisk-Fysiske Meddelelser, 26, 1

Korsheninnikov, A. A. 1990, Analysis of the properties of three-particle decays of nuclei with A=12 and 16 in the K-harmonics method, Soviet Journal of Nuclear Physics, 52, 827

Krane, K. S. 1988, Introductory nuclear physics (John Wiley & Sons)

Kronenberg, A. 2001, Entwicklung einer online-Chromatographie für Element 106 (Seaborgium), PhD thesis, Johannes Gutenberg-Universität Mainz

Lane, A. M. & Thomas, R. G. 1958, R-Matrix theory of nuclear reactions, Reviews of Modern Physics, 30, 257

Langanke, K., Wiescher, M., & Thielemann, F.-K. 1986, The triple alpha reaction at low temperatures, Zeitschrift für Physik A, 324, 147

Lunney, D. 2006, Mass measurements of exotic nuclei and their role in stellar nucleosynthesis, in Proceedings of the International Symposium on Nuclear Astrophysics—Nuclei in the Cosmos—IX, Proceedings of Science, PoS(NIC–IX)

Markham, R. G., Austin, S. M., & Shahabuddin, A. M. 1976, A Measurement of $\Gamma_{\rm rad}/\Gamma$ for the 7.654 MeV state of ^{12}C and the rate of the stellar 3α reaction, Nuclear Physics A, 270, 489

Morinaga, H. 1956, Interpretation of some of the excited states of 4n self-conjugate nuclei, Physical Review, 101, 254

Morinaga, H. 1966, On the spin of a broad state around 10 MeV in ^{12}C, Physics Letters, 21, 78

Nolen, J. A. & Austin, S. M. 1976, Measurement of the excitation energy of the 7.654 MeV state of ^{12}C and the rate of the 3α reaction, Physical Review C, 13, 1773

Nomoto, K., Thielemann, F.-K., & Miyaji, S. 1985, The triple alpha reaction rate at low temperatures in accreting white dwarfs and neutron stars, Astronomy and Astrophysics, 149, 239

Ohlsen, G. G. 1965, Kinematic relations in reactions of the form $A + B \rightarrow C + D + E$, Nuclear Instruments and Methods, 37, 240

Öpik, E. J. 1951, Stellar models with variable composition II. Sequences of models with energy generation proportional to the fifteenth power of temperature, Proceedings of the Royal Irish Academy A, 54, 49

Pauli, W. 1964, Exclusion principle and quantum mechanics, in Nobel Lectures, Physics 1942-1962 (Elsevier Publishing Company), 27–43

Pedersen, S. G., Diget, C. A., Fynbo, H. O. U., et al. 2006, β-decay studies of states in ^{12}C, in Proceedings of the International Symposium on Nuclear Astrophysics—Nuclei in the Cosmos—IX, Proceedings of Science, PoS(NIC–IX)244

Penttilä, H. 1998, Layout of the IGISOL facility, available at: http://www.phys.jyu.fi/

Pfennig, G., Klewe-Nebenius, H., & Seelmann-Eggebert, W. 1998, Karlsruher Nuklidkarte (Forschungszentrum Karlsruhe, Teknik und Umwelt)

Pieper, S. C. 2002, Quantum monte carlo calculations of light nuclei, The European Physical Journal A, 13, 75

Saha, M. N. 1920, Ionization in the solar chromosphere, Philosophical Magazine, 40, 472

Salpeter, E. E. 1952, Nuclear reactions in stars without hydrogen, The Astrophysical Journal, 115, 326

Schreckenbach, K., Liaud, P., Kossakowski, R., et al. 1995, A new measurement of the beta emission asymmetry in the free decay of polarized neutrons, Physics Letters B, 349, 427

Schwalm, D. & Povh, B. 1966, Alpha particles following the β-decay of ^{12}B and ^{12}N, Nuclear Physics, 89, 401

Shiers, J. 1996, CERN program library short writeups, available at http://cern.ch/cernlib

Smirnova, N. A. & Volpe, C. 2003, On the asymmetry of Gamow-Teller β-decay rates in mirror nuclei in relation with second-class currents, Nuclear Physics A, 714, 441

Strehl, P. 1970, Untersuchung von 0^+–0^+-Übergängen in ^{12}C, ^{24}Mg, ^{28}Si, ^{32}S und ^{40}Ca durch unelastische Elektronenstreuung, Zeitschrift für Physik A, 234, 416

Szczurek, A., Bodek, K., Jarczyk, L., et al. 1991, Ghost anomaly and first excited state of ^{8}Be in the ^{9}Be(d,tα)^{4}He reaction at 7 MeV, Nuclear Physics A, 531, 77

Tengblad, O., Bergmann, U. C., Fraile, L. M., Fynbo, H. O. U., & Walsh, S. 2004, Novel thin window design for a large-area silicon strip detector, Nuclear Instruments and Methods A, 525, 458

Thaysen, J. 1999, β-delayed proton emission from ^{31}Ar, Master's thesis, Department of Physics and Astronomy, University of Aarhus, Denmark

Tilley, D., Kelley, J., Godwin, J., et al. 2004, Energy levels of light nuclei A = 8, TUNL evaluation available at http://www.tunl.duke.edu/nucldata/

Towner, I. S., Hagberg, E., Hardy, J. C., & Koslowsky, V. T. 1995, Superallowed Fermi beta decay—a status report, in Proceedings of the International Conference on Exotic Nuclei and Atomic Masses (ENAM 95), Arles, France, 1995, ed. M. D. S. Simon & O. Sorlin (World Scientific Publishing Co.), 711

Tur, C. & Austin, S. M. 2006, Improving the rate of the triple-alpha process, in Proceedings of the International Symposium on Nuclear Astrophysics—Nuclei in the Cosmos—IX, Proceedings of Science, PoS(NIC–IX)

Weaver, R. F. 2002, Molecular biology, 2nd edn. (McGraw-Hill Higher Education)

Weiss, A., Serenelli, A., Kitsikis, A., Schlattl, H., & Christensen-Dalsgaard, J. 2005, Influence of two updated nuclear reaction rates on the evolution of low and intermediate mass stars, Astronomy and Astrophysics, 441, 1129

Wilkinson, D. H., Alburger, D. E., & Gallmann, A. 1963, Alpha-particle emission in the decays of B^{12} and N^{12}, Physical Review, 130, 1953

Wilkinson, D. H. & Macefield, B. E. F. 1974, A parametrization of the phase space factor for allowed β-decay, Nuclear Physics A, 232, 58

Young, T. 1804, The Bakerian Lecture. Experiments and calculations relative to physical optics, Philosophical Transactions of the Royal Society of London, 94, 1

Ziegler, J. F., Biersack, J. P., & Littmark, U. 2003, The stopping and range of ions in solids (Pergamon Press), program package available at: http://www.srim.org/